

# THz pulse compression

Dissertation  
zur Erlangung des Doktorgrades  
an der Fakultät für Mathematik, Informatik und Naturwissenschaften  
Fachbereich Physik  
der Universität Hamburg

vorgelegt von  
**Javier Nicolás Gutiérrez González**

Hamburg  
2021

Gutachter der Dissertation	Prof. Dr. Franz X. Kärtner Dr. Nicholas H. Matlis
Zusammensetzung der Prüfungskommission:	Prof. Dr. Franz X. Kärtner Dr. Nicholas H. Matlis Prof. Dr. Daniela Pfannkuche Prof. Dr. Markus Drescher Dr. Mark J. Prandolini
Vorsitzender der Prüfungskommission:	Prof. Dr. Daniela Pfannkuche
Datum der Disputation:	19. Januar 2022
Vorsitzender Fach-Promotionsausschusses PHYSIK:	Prof. Dr. Wolfgang Hansen
Leiter des Fachbereichs Physik:	Prof. Dr. Günter H. W. Sigl
Dekan der Fakultät MIN:	Prof. Dr. Heinrich Graener

## **Eidesstattliche Versicherung / Declaration on oath**

Hiermit versichere ich an Eides statt, die vorliegende Dissertationsschrift selbst verfasst und keine anderen als die angegebenen Hilfsmittel und Quellen benutzt zu haben.

Hamburg, den 22.10.2021

---

Unterschrift des Doktoranden



---

# Abstract

Compact THz-based particle accelerators require Terahertz (THz) pulses of tens of mJ of energy to achieve high acceleration fields of hundreds of MV/m. Despite the promising prospects of scaling THz generation to these energy ranges by non-linear optical processes, their conversion efficiency for high-energy (HE) THz applications is currently too low.

Aiming to provide a new way of producing HE THz pulses, this thesis presents the development of a THz pulse compression system by which the signal emitted by a continuous-wave (CW) THz source is enhanced in intensity and compressed in duration into short pulses. For this purpose, a 900 mm long bow-tie enhancement cavity resonant with the Gaussian mode of a 100 GHz frequency CW incident electro-magnetic wave was implemented in a quasi-optical way. Inside the cavity, the intensity of the incident 100 GHz radiation was enhanced a certain number of times expressed through the parameter  $\mathcal{E}$ . Subsequently, the cavity circulating THz radiation was extracted out in the form of a short pulse by using a laser-driven semiconductor switch. In particular, for a 145- $\mu\text{W}$  cavity input light and a 532-nm, 7-ns, 50-mJ excitation laser pulse, the compression system was performed under two specific scenarios. First, for a  $\mathcal{E} \approx 17.5$  and by using an intrinsic silicon wafer, a maximum power of 940  $\mu\text{W}$  was extracted, corresponding to  $\sim 38\%$  of the cavity circulating power. Second, for a  $\mathcal{E} \approx 6.5$  and by utilizing an intrinsic gallium arsenide wafer, a maximum power of 635  $\mu\text{W}$  was extracted, corresponding to  $\sim 67\%$  of the cavity circulating power. In both cases, the duration of the extracted pulse was about  $\sim 28$  ns, distributed in four main oscillations, each of them with a period of around  $6 \sim 7$  ns and different amplitude. These results proved that the magnitude, shape and duration of the extracted pulse were dependent on four factors: the cavity length, the parameter  $\mathcal{E}$ , the energy of the excitation laser pulse and the switching dynamics of the semiconductor wafer.

Based on observations made from the current compression system, two conclusions

can be drawn:

- (i) The length of the resonator needs to be matched to the semiconductor response and the laser driver pulse length used.
- (ii) The cavity and semiconductor switch size as well as laser energy needed needs to be scaled to a high power THz source such as gyrotrons. Such gyrotron sources have been developed to the multi-MW scale for electron-cyclotron resonance heating of fusion plasmas.

---

# Zusammenfassung

Kompakte THz-basierte Teilchenbeschleuniger benötigen Terahertz (THz) Pulse mit einer Energie von mehreren zehn mJ, um hohe Beschleunigungsfelder von Hunderten von MV/m zu erreichen. Trotz der vielversprechenden Aussichten, die THz-Erzeugung durch nichtlineare optische Prozesse in diese Energiebereiche hoch zu skalieren, ist deren Umwandlungseffizienz für hochenergetischen (HE) THz-Anwendungen derzeit noch zu gering.

Mit dem Ziel, einen neuen Weg zur Erzeugung von HE-THz-Pulsen zu finden, wird in dieser Arbeit die Entwicklung eines THz-Pulskompressionssystems vorgestellt, mit dem das von einer Dauerstrich-THz-Quelle emittierte Signal in seiner Intensität verstärkt und in seiner Dauer zu kurzen Pulsen komprimiert wird. Zu diesem Zweck wurde ein 900 mm langer Bow-Tie-Resonator aufgebaut, dessen Resonanzfrequenz auf das Einkoppeln der Gauß-Mode des 100 GHz Dauerstrich-THz-Strahlung abgestimmt ist. Im Inneren des Resonators wurde die Intensität der einfallenden 100 GHz-Strahlung um ein bestimmtes Vielfaches, ausgedrückt durch den Überhöhungsfaktor  $\mathcal{E}$ , erhöht. Anschließend wurde die im Resonator zirkulierende Strahlung in Form eines kurzen Pulses mit Hilfe eines lasergesteuerten Halbleiter-Schalters ausgekoppelt. Insbesondere wurde das Kompressionssystem für ein 145- $\mu$ W-Resonator-Eingangsstrahl und einen 532-nm, 7-ns, 50-mJ-Anregungslaserpuls unter zwei spezifischen Szenarien getestet. Zuerst wurde bei einem Überhöhungsfaktor  $\mathcal{E} \approx 17.5$  und unter Verwendung eines intrinsischen Silizium-Wafers eine maximale Leistung von 940  $\mu$ W extrahiert, was  $\sim 38\%$  der umlaufenden Leistung des Resonators entspricht. Als nächstes wurde bei einem Überhöhungsfaktor  $\mathcal{E} \approx 6.5$  und unter Verwendung eines intrinsischen Galliumarsenid-Wafers eine maximale Leistung von 635  $\mu$ W extrahiert, was  $\sim 67\%$  der Umlaufleistung des Resonators entspricht. In beiden Fällen betrug die Dauer des extrahierten Pulses etwa  $\sim 28$  ns, verteilt auf vier Hauptschwingungen, jede mit einer Periode von etwa  $6 \sim 7$  ns und unterschiedlicher Amplitude. Diese Ergebnisse zeigen, dass die Größe,

Form und Dauer des extrahierten Pulses von vier Faktoren abhängt: der Resonatorlänge, dem Überhöhungsfaktor  $\mathcal{E}$ , der Energie des Anregungslaserpulses und der Schaltdynamik des Halbleiter-Wafers.

Zweierlei Schlussfolgerungen lassen sich aus den Beobachtungen der Funktionsweise des Kompressionssystems ziehen:

- (i) Die Resonatorlänge muss zur Dynamik des Halbleiterschalters und der Länge des Laserpulses angepasst sein.
- (ii) Die Größe des Resonators sowie Halbleiterschalters sowie Laserpulseenergie muss auf die Leistung der THz-Quelle angepasst werden, um die gewünschten HE-THz-Pulse im multi-MW-Bereich erzeugen zu können. Solche THz-Quellen sind Gyrotrons mit multi-MW-Ausgangsleistung, welche zum Zweck der resonanten Elektron-Zyklotron-Heizung von Fusionsplasmen entwickelt wurden.



---

# Acknowledgments

I would like to greatly thank my supervisor Prof. Franz Kärtner for giving me the invaluable opportunity to do my PhD in his research group, in addition to the support, help and knowledge given throughout these years. Thank you very much to Dr. Nicholas Matlis for his knowledge, constant help and great motivation, fundamental for the realization of my project. Many thanks to Dr. Arya Fallahi for his support and knowledge given in the first part of my doctorate, essential to introduce me to this new challenge. I cordially thank Prof. Daniela Pfannkuche, Prof. Markus Drescher, and Dr. Mark Prandolini for having kindly agreed to be part of the Doctoral committee.

Huge thanks to Uta and Christine!. Without you, my stay in this beautiful city would definitely not have been possible. Total thanks to my office friends Tobi, Miguel and Fabian for the good moments and their always willingness to help me. Of course, big thanks to my friend Halil (pegasus!) for all the support and the memorable moments lived!. To my colleagues Thomas, Andrej, Timm, Simon, Wenlong, Giovanni, Felix, Dongfang, Mikhail, Mohamed, Elias, Erwin and the whole group in general, thanks a lot for everything!.

I am very grateful to the National Research and Development Agency ANID for granting me the PhD scholarship abroad, Becas Chile, during the period 2017 – 2020, crucial for the completion of my studies.

I want to infinitely thank my friends José and Sebastián for their friendship, joy, support and company during all these years, you are the best!. Thank you very much to Steffi!, always cordial and ready to help me from my first second in Hamburg!.

Mi familia ha sido el soporte fundamental a través de toda mi vida. Siempre seré un agradecido de la vida por darme la oportunidad de crecer, compartir y amar junto a ellos. Obviamente no puedo dejar pasar la oportunidad de nuevamente agradecerles por todo. ¡Gracias infinitas queridos padres y hermanos!. Y como diría mi querido papá: “De alguna manera me las arreglé, en este aún viaje, como el de tantos”...



---

# Contents

<b>Abstract</b>	<b>5</b>
<b>Zusammenfassung</b>	<b>7</b>
<b>Acknowledgments</b>	<b>9</b>
<b>1 Introduction</b>	<b>15</b>
<b>2 Preliminary concepts</b>	<b>21</b>
2.1 Introduction . . . . .	21
2.2 The fundamental Gaussian beam mode . . . . .	22
2.3 Higher-order modes . . . . .	27
2.4 The ABCD matrix . . . . .	28
2.5 The two-mirror enhancement cavity . . . . .	31
2.5.1 Field distribution condition . . . . .	32
2.5.2 Phase condition: Resonance frequencies . . . . .	35
2.5.3 Intensity relations . . . . .	36
2.5.4 Impedance matching and enhancement factor ( $\mathcal{E}$ ) . . . . .	38
<b>3 The bow-tie enhancement cavity</b>	<b>41</b>
3.1 Introduction . . . . .	41
3.2 Definition and design . . . . .	42
3.3 Design of the input coupler mirror (ICM) . . . . .	47
3.3.1 Simulated response of the ICM . . . . .	51
3.4 Experimental results . . . . .	52
3.4.1 Mode matching . . . . .	53
3.4.2 Bow-tie enhancement cavity setup . . . . .	55

---

3.4.3	Impedance matching and enhancement factor . . . . .	58
<b>4</b>	<b>Semiconductor as an optical switch</b>	<b>65</b>
4.1	Introduction . . . . .	65
4.2	Energy bands in semiconductors . . . . .	66
4.3	Carrier current . . . . .	68
4.3.1	Drift current . . . . .	68
4.3.2	Diffusion current . . . . .	69
4.4	Carrier photogeneration and recombination . . . . .	70
4.4.1	Direct band gap semiconductors . . . . .	71
4.4.2	Indirect band gap semiconductors . . . . .	72
4.4.3	The recombination time . . . . .	74
4.5	Continuity equation . . . . .	74
4.5.1	Photon absorption and excess of carriers . . . . .	75
4.6	Optical switch principle . . . . .	76
4.6.1	The Drude-Lorentz model . . . . .	78
4.6.2	Complex refractive index . . . . .	81
4.6.3	Reflectance at the photoconductive state . . . . .	82
4.7	Simulated response of semiconductors . . . . .	84
4.7.1	Power requirements of the excitation laser . . . . .	87
4.8	Experimental results . . . . .	89
4.8.1	Results for intrinsic silicon semiconductor wafer . . . . .	89
4.8.2	Results for intrinsic GaAs semiconductor wafer . . . . .	92
4.8.3	Comments on the experimental results . . . . .	94
<b>5</b>	<b>100 GHz radiation compression</b>	<b>97</b>
5.1	Introduction . . . . .	97
5.2	Experimental setup . . . . .	97
5.3	Pulse compression by using Si SW . . . . .	98
5.3.1	Discussion of the extracted pulse . . . . .	100
5.3.2	Efficiency of the compression process . . . . .	103
5.4	Pulse compression by using GaAs SW . . . . .	104
5.4.1	Efficiency of the extracted pulse . . . . .	106
5.5	Final remarks . . . . .	108
<b>6</b>	<b>Conclusions and Outlook</b>	<b>109</b>

<b>A 100 GHz IMPATT diode source</b>	<b>113</b>
<b>Bibliography</b>	<b>117</b>



---

# Chapter 1

## Introduction

Originally, particle accelerations were invented and designed to study the elementary components of matter. However, over the years their use has expanded to a wide range of applications, ranging from medicine and industry to the generation of high brilliance X-rays. As a result, currently, there are more than 30,000 accelerators around the world [WH20]. Some of them involve large facilities and production costs, which has recently prompted efforts to reduce their size based on new technologies. In particular, milestones in electron acceleration by terahertz (THz) radiation [NHH<sup>+</sup>15, LJ16] have demonstrated the viability of developing THz-based accelerators. For instance, the AXSIS project – Frontiers in Attosecond X-ray Science: Imaging and Spectroscopy – focuses on developing a new electron accelerator and radiation technology, which aims to build a compact source of attosecond X-ray pulses to study the dynamics of biological processes [KAC<sup>+</sup>16]. The source is planned to be driven entirely by laser systems which have the potential to make the device’s infrastructure more compact and less costly. The pivotal idea is to use radiation centered at THz frequencies (in the range 0.1 – 1 THz) for particle acceleration. This corresponds to a 200 times shorter wavelength compared with conventional radio-frequency (RF) driven accelerators composed of metallic RF structures usually operating at about 1 ~ 3 GHz. This leads to excitation with shorter pulse durations, which increases the threshold of the field emission with an expected peak field in the range of 1 GV/m and reduces the pulsed heating damage, being the latter one that limits electron acceleration fields in linear accelerators (LINAC). Specifically, the AXSIS machine seeks to accelerate the electron beam in two steps. First, by a THz-Gun powered by single-cycle (SC) THz radiation, in which the electrons are accelerated from rest to ~ 1 MeV. Second, by a THz-LINAC powered by

multi-cycle (MC) THz radiation centered at  $\sim 0.3$  THz with pulse energies of  $\sim 20$  mJ and hundreds of picosecond pulse duration, in which the electrons are accelerated from  $\sim 1$  MeV to the final energy of  $\sim 20$  MeV.

In parallel, to avoid and minimize damages by RF breakdown [PS14], different experimental tests and studies have been carried out to upgrade the working frequency of some LINACs from the standard 1 – 12 GHz operation to the millimeter-wave range (30 – 300 GHz). For example, at the Facility for Advanced Accelerator Experimental Tests (FACET) in the SLAC National Accelerator Laboratory, different customized metallic copper and stainless steel traveling wave acceleration structures were excited, using FACET electron beams, at THz frequencies, from 115 GHz to 140 GHz, achieving a maximum accelerating gradient of 0.3 GV/m with a peak surface electric field of 1.5 GV/m and a pulse duration of around 2.4 ns. Under these conditions, the structures did not experience damage by RF breakdown [DFDB<sup>+</sup>16b]. Furthermore, RF breakdown rates in 200 GHz copper and copper-silver metallic accelerating structures have been characterized by using peak electric fields in the range of 350 – 500 MV/m with a pulse length of about 0.3 – 0.5 ns [DFDB<sup>+</sup>16a].

The particle's acceleration structures mentioned so far involve high-energy (HE) THz pulses and consequently high peak accelerating fields in the MV/m range, even GV/m for the AXISIS case. These quantities can be generated by electron beams as drivers of linear accelerator-based THz sources [CBB<sup>+</sup>13, CCF<sup>+</sup>20], which require again large installations. Nevertheless, there are many conventional methods for generating THz pulses [HF11]. Most of them employ table-top techniques in nonlinear optics, in which the energy of high-power (HP) optical lasers interacts with nonlinear materials to convert the energy into THz radiation. Among them, the maximum conversion efficiencies (CE) in SC THz generation have been accomplished by employing the optical rectification (OR) method, especially through the tilted-pulse-front (TPF) technique [HAKK02, WTHK20] in cryogenically cooled lithium niobate (LiNbO<sub>3</sub>) crystals. Specifically, in [FOL<sup>+</sup>14] they achieved the highest CE so far of 0.77 %, with THz pulses energy over 0.4 mJ and for frequencies below 1 THz by using a 60-mJ, 1030-nm, 785-fs laser. Similarly, in [Kä20] they reported the generation of SC THz pulses with an energy of 0.2 mJ, at a center frequency of 0.28 THz and a CE of 0.5 % by using a 40-mJ, 1020-nm, 1-ps laser. In the case of MC THz generation, the highest CE has been obtained via difference frequency generation (DFG) by employing a tunable two narrow-spectral lines separation, 15-mJ, 10-Hz, 250-ps multi-line laser source into a Mg-doped periodically poled lithium niobate (MgO:PPLN) crystal achieving a CE



of 0.49 % at 0.29 THz and 0.89 % at 0.53 THz, respectively [Olg21]. Previously, also through the DFG method, using the chirp and delay (CD) technique [WHFA94] in a PPLN crystal, a maximum CE of 0.24 % with pulse energies of 0.6 mJ at 0.361 THz was reached by using a 1.2-J, 800-nm, 5-Hz, 260-ps laser [JMA<sup>+</sup>19].

However, despite the promising prospects of scaling THz generation to the millijoule regime in both SC and MC by optical laser-driven THz sources, the conversion efficiency of these methods is still low for HE terahertz applications. This has led to the search for new alternatives of obtaining short HE THz pulses. Under such a scenario, the laser-driven semiconductor switch (LDSS) technique has been widely used allowing the production of short pulses with frequencies from the microwaves (3 – 30 GHz) to the far infrared (FIR, 3 – 100 THz) range. This technique involves a laser pulse exciting the surface of a semiconductor causing an increment of its carrier concentration. As a consequence, the plasma frequency ( $\omega_p$ ) associated with the semiconductor also increases which makes the material to become momentarily reflective for all incident frequencies below  $\omega_p$ . Here, the temporal reflectivity depends on the duration of the laser pulse and the characteristics of the semiconductor (see section 4.6). Lately, to obtain THz pulses at a megawatt (MW) level, the LDSS method has been used to shorten the radiation emitted by stable, efficient, HP sources, such as gyrotron-based sources [SKS12], which can deliver MW of  $\mu$ s pulsed or continuous-wave (CW) THz radiation power with efficiencies as high as 60 % [JAA<sup>+</sup>17, HBG<sup>+</sup>02, SKT<sup>+</sup>07]. For instance, in [KJS<sup>+</sup>19] from a 1.5-MW, 3- $\mu$ s pulse, 110-GHz gyrotron source, they produced 9-ns, 110-GHz pulses by exciting a 387  $\mu$ m thick silicon (Si) wafer by a 230-mJ, 532-nm, 6-ns laser achieving more than 70 % reflectance for a gyrotron incident power limit of 600 kW. In the same way, in [OPS<sup>+</sup>20] and after their previously mentioned tests in [DFDB<sup>+</sup>16b] and [DFDB<sup>+</sup>16a], from a 1.25-MW, 3- $\mu$ s pulse, 110-GHz gyrotron source, they generated 10-ns, 110-GHz pulses by exciting a 387- $\mu$ m thick Si wafer by a 230-mJ, 523-nm, 6-ns laser achieving more than 75 % reflectance for a gyrotron incident power limit of 600 kW. Eventually, these pulses were used to successfully power a millimeter-wave electron accelerating structure accomplishing a gradient up to 230 MV/m corresponding to a peak surface electric field > 520 MV/m.

Based on the relevance of generating high-energy pulses in the THz regime for future THz-based LINACs and in order to provide a new way of producing such HE THz pulses, this thesis presents the development of a THz pulse compression system by which the signal emitted by a CW THz source is enhanced in intensity and compressed in duration into short pulses. Specifically, the system is composed of a quasi-optical bow-

tie enhancement cavity with an intracavity semiconductor wafer (SW) operating under the LDSS method. Firstly, an input 100 GHz Gaussian beam is resonantly accumulated inside the cavity a certain number of times. Secondly, the SW placed between the cavity mirrors is optically excited by a 7-ns, 532-nm laser pulse. This excitation induces a momentary reflectance in the SW for THz frequencies. As a result, a compressed 100 GHz radiation (short pulse) is extracted out from the cavity.

## Thesis outline

The THz pulse compression system contemplates the resonant coupling between the fundamental Gaussian mode of the 100 GHz input radiation and the lowest transverse mode of the bow-tie cavity. Thereby, chapter 2 describes some fundamental concepts about it, such as the mathematical expression of the Gaussian beam (section 2.2) together with a brief description of the high-order Hermite-Gaussian modes (section 2.3). Moreover, section 2.4 presents the q-transformation rule through the ABCD matrix as a method to know the behavior of the radiation throughout the optical components of the cavity. Finally, section 2.5 shows a general description of the two-mirror optical cavity as a prelude to understand the bow-tie cavity principle.

Chapter 3 explains the most important properties and the design process of the bow-tie enhancement cavity configuration (section 3.2) by following a similar analysis of the two-mirror resonator of chapter 2. Furthermore, sections 3.3 and 3.4 shows the different components involved in the configuration as well all the mounting processes with the corresponding experimental results.

Chapter 4 describes the principle of the LDSS technique, which is the other main subject of this thesis. Firstly, section 4.2 gives a general overview of semiconductors. Next, sections 4.3, 4.4 and 4.5 analyze a quasi-classical theoretical background of semiconductors under non-equilibrium conditions. After that, section 4.6 presents the optical switch principle with simulations on Si and GaAs semiconductors (section 4.7). Finally, section 4.8 shows the experimental results of a Si and GasAs wafer working as an optical switch.

Chapter 5 describes the implementation of the THz pulse compression system, which means, the bow-tie optical cavity and the LDSS method. In this way, sections 5.3 and 5.4 present the experimental results of the system by using Si and GaAs wafers, respectively.

Finally, chapter 6 summarizes the results obtained throughout the thesis and of-

fers an outlook of the current and future design of the system on high-power THz applications by using gyrotron sources.



---

# Chapter 2

## Preliminary concepts

### 2.1 Introduction

Generally, in the interaction processes between light and optical cavities it is desirable to study the behavior of the lowest transverse mode of the radiation field. This mode is associated with a certain type of light beam called Gaussian beam, named after the fact that its intensity distribution, transverse to the propagation axis, undergoes precisely a Gaussian beam profile.

On the other hand, an optical cavity is an arrangement of a certain number of mirrors designed to store and confine different light beam modes. It is a fundamental part of laser devices and is widely utilized as a frequency oscillator in dedicated optical applications such as regenerative amplifiers and optical parametric oscillators, among others.

This section describes a number of fundamental concepts necessary as a prelude to the research work developed in this thesis. In particular, a global analysis under rectangular coordinates of the formal mathematical expression of the Gaussian beam, as well as a brief description of the high-order Hermite-Gaussian beam modes, is presented. In addition, the q-transformation rule through the ABCD matrix and a general description of the two-mirror optical cavity are shown. A more detailed and in-depth study can be found in the referenced literature.

## 2.2 The fundamental Gaussian beam mode

THz pulse compression system presented in this thesis contemplates the resonant coupling between the fundamental Gaussian mode of the 100 GHz input radiation and the lowest transverse mode (Gaussian mode) of the bow-tie cavity. Thereby, it is fundamental to understand the nature involved in Gaussian beams.

A laser system is the best application example in which light is generated with a Gaussian beam profile. Due to the natural divergence of propagation, the wavefront associated with the emitted light experiences different patterns. This starts as a plane wave just at the laser output and then changes slowly towards a spherical wave form as the light spreads away from the source. In this scenario, as the first step in order to obtain the mathematical expression of the Gaussian beam, the electric and magnetic field components of an electromagnetic wave are described by a wave function of position and time  $U(\mathbf{r}, t) = U(x, y, z, t)$  which satisfies the three-dimensional wave equation given by:

$$\nabla^2 U - \frac{1}{c^2} \frac{\partial^2 U}{\partial t^2} = 0, \quad (2.2.1)$$

where  $\nabla^2 = \partial/\partial x^2 + \partial/\partial y^2 + \partial/\partial z^2$  is the Laplacian operator and  $c$  the speed of light.

The simplest representation of a wave function is the monochromatic wave defined as:

$$U(\mathbf{r}, t) = U(\mathbf{r})e^{-i\omega t}, \quad (2.2.2)$$

wherein the complex amplitude  $U(\mathbf{r}) = U(x, y, z)$  depends on the spatial coordinates and  $e^{-i\omega t}$  is the time dependence of the wave. Thus, the substitution of Eq. (2.2.2) into Eq. (2.2.1) leads to the Helmholtz equation described as:

$$\nabla^2 U + k^2 U = 0, \quad (2.2.3)$$

with  $k$  defined as the wavenumber. Assuming that the wave is propagating in a homogeneous and isotropic medium with refractive index  $n$ , then  $k = 2\pi\nu n/c = \omega n/c = 2\pi n/\lambda$  where  $\nu$  is the wave frequency,  $\omega = 2\pi\nu$  is the angular wave frequency and  $\lambda$  is the wavelength of the wave. From now on, the light propagation is assumed throughout

free space. Therefore  $n \approx 1$ .

Considering a propagation in the  $z$  axis, an Ansatz solution of the Helmholtz equation is the plane wave given by:

$$U(\mathbf{r}) = A(\mathbf{r})e^{-ikz}. \quad (2.2.4)$$

Thus, by replacing Eq. (2.2.4) into Eq. (2.2.3) it follows that:

$$\frac{\partial^2 A}{\partial x^2} + \frac{\partial^2 A}{\partial y^2} + \frac{\partial^2 A}{\partial z^2} - 2ik \frac{\partial A}{\partial z} = 0. \quad (2.2.5)$$

The term  $e^{-ikz}$  in Eq. (2.2.4) implies that the wave oscillates through the propagation direction. Meanwhile, the complex envelope  $A(\mathbf{r})$  connects the minimum and maximum of the oscillation and decreases slowly with respect to  $z$  within a distance  $\Delta z = \lambda$ . Thereby, the change  $\Delta A$  is much smaller than  $A$ , i.e.,  $\Delta A \ll A$ , which means  $A$  varies slowly with  $z$  [ST07]. For this reason, by neglecting the term  $\partial^2 A / \partial z^2$  compared with the other second order derivatives, Eq. (2.2.5) becomes:

$$\begin{aligned} \frac{\partial^2 A}{\partial x^2} + \frac{\partial^2 A}{\partial y^2} - 2ik \frac{\partial A}{\partial z} &= 0 \\ \nabla_T^2 A - 2ik \frac{\partial A}{\partial z} &= 0, \end{aligned} \quad (2.2.6)$$

which is called the *paraxial wave equation*.

The waves that are solutions of Eq. (2.2.6) are called *modes of propagation* and keep their principle shape. The simplest one is the fundamental mode solution which corresponds to the Gaussian beam. Its expression has the form [KL66]:

$$A(\mathbf{r}) = E_0 e^{-i \frac{k\rho}{2q(z)}} e^{-iP(z)}, \quad (2.2.7)$$

wherein  $\rho = x^2 + y^2$  is the radial direction,  $E_0$  is the amplitude constant,  $P(z)$  is the complex phase shift and  $q(z)$  is the q-parameter.

### The q-parameter

$q(z)$  is an essential complex parameter from which crucial features of the beam can be calculated. It is defined as:

$$\frac{1}{q(z)} = \frac{1}{R(z)} - \frac{\lambda}{\pi w(z)^2} i. \quad (2.2.8)$$

In Eq. (2.2.8),  $R(z)$  corresponds to the radius of curvature of the wavefront that intersects the axis at position  $z$ . On the other hand, the term  $w(z)$ , known as the *beam radius*, is the distance at which the beam intensity  $I$  is  $1/e^2$  times its maximum value  $I_0$  [KL66]. Both are defined by Eqs. (2.2.9) and (2.2.10), respectively. It should be pointed out that  $I$  decreases in a Gaussian way with the distance from the  $z$  axis.

$$R(z) = z \left[ 1 + \left( \frac{\pi w_0^2}{\lambda z} \right)^2 \right]. \quad (2.2.9)$$

$$w(z) = w_0 \sqrt{1 + \left( \frac{\lambda z}{\pi w_0^2} \right)^2}. \quad (2.2.10)$$

In the above equations, the constant  $w_0$  is called *beam waist* and corresponds to the minimum radius of the beam (which occurs at  $z = 0$  in Eq. (2.2.10)). At position  $z = 0$ , the wavefront of the beam is planar in nature, whereas at points far away it experiences a spherical behavior. The way how the wavefront spreads along  $z$  obeys the divergence angle  $\theta$  given by:

$$\theta = \frac{\lambda}{\pi w_0}. \quad (2.2.11)$$

Then, the limit where the plane wavefront turns into spherical wavefront is called *Rayleigh length*, denoted as  $z_R$  and defined as:

$$z_R = -\frac{\text{Im} \left\{ \frac{1}{q} \right\}}{\left| \frac{1}{q} \right|^2}, \quad (2.2.12)$$

where  $2z_R$  is the confocal parameter. In addition, the beam waist is related to  $z_R$  by:



$$w_0 = \sqrt{\frac{\lambda z_R}{\pi}}. \quad (2.2.13)$$

Eventually, the distance from a position  $z$  of the beam to the beam waist  $w_0$  is mathematically expressed in terms of the  $q$ -parameter in the form:

$$z = -\frac{\operatorname{Re}\left\{\frac{1}{q}\right\}}{\left|\frac{1}{q}\right|^2}. \quad (2.2.14)$$

The Gaussian beam parameters seen so far describe how the beam amplitude spreads with respect to the propagation axis  $z$  and to the radial direction  $\rho$ . A graphical representation of them is depicted in Fig. 2.1.

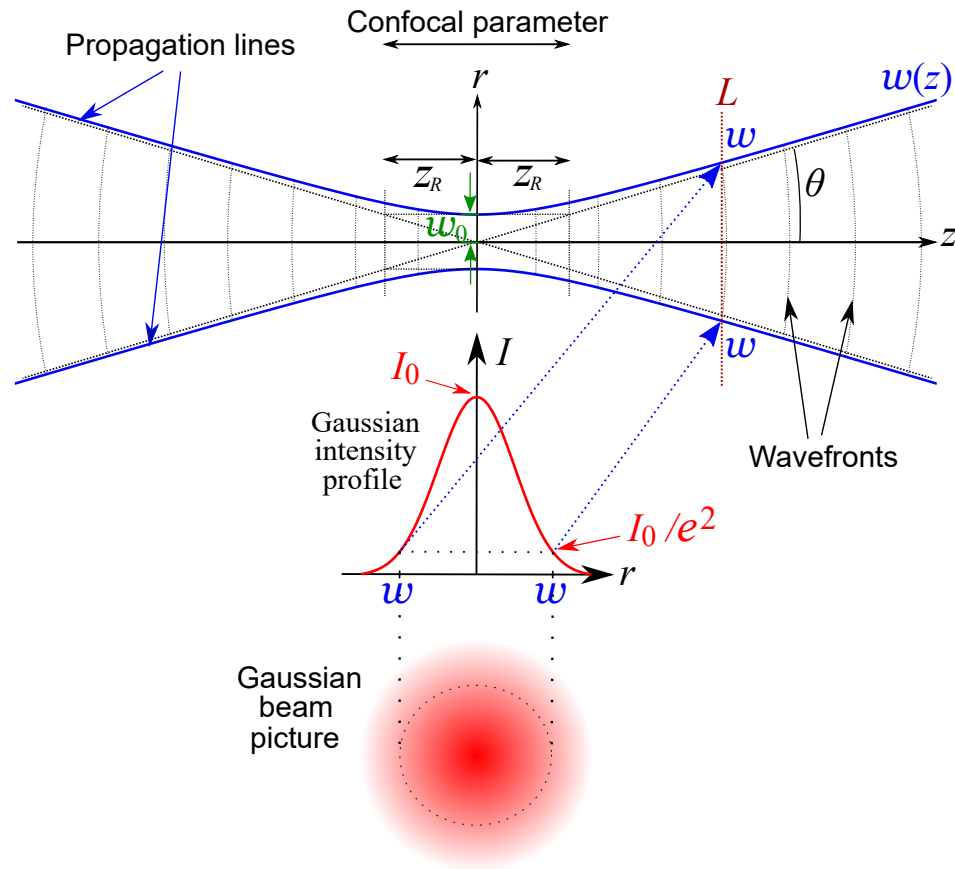


**Figure 2.1:** Fundamental propagation mode equivalent to a Gaussian beam showing some of its relevant parameters and the intensity profile with a beam picture at the transverse plane  $L$ .

### The complex phase shift

$P(z)$  provides the phase factors present in the Gaussian beam. The substitution of Eq. (2.2.7) into Eq. (2.2.6) produces the following relation:

$$\frac{dP(z)}{dz} = \frac{-i}{q(z)} = -\frac{i}{z + i(\pi w_0^2/\lambda)}. \quad (2.2.15)$$

Then, by using the previous definitions of  $q(z)$ ,  $R(z)$  and  $w(z)$  into Eq. (2.2.15), the solution of the integral  $\int_0^z \frac{dP(z)}{dz}$  leads to the following expression for  $P(z)$  [KL66][Nag10]:

$$iP(z) = \ln \left[ 1 - i \left( \frac{\lambda z}{\pi w_0^2} \right) \right] = \ln \sqrt{1 + \left( \frac{\lambda z}{\pi w_0^2} \right)^2} - i\Phi. \quad (2.2.16)$$

Looking at the right-hand side of Eq. (2.2.16), the logarithmic term reduces the beam intensity, whereas the term  $\Phi$ , known as the *Gouy phase*, basically gives an additional phase shift to the wavefront at position  $z$  with respect to a plane wave [KL66][ST07]. It is defined by:

$$\Phi = \tan^{-1} \left( \frac{z}{z_R} \right) = \tan^{-1} \left( \frac{\lambda z}{\pi w_0^2} \right), \quad (2.2.17)$$

with  $\Phi \in [-\pi, \pi]$ . This parameter plays an important role in defining the resonance frequencies of optical cavities, as will be discussed later.

### Mathematical expression of the Gaussian beam

Finally, by putting the parameters defined so far into Eq. (2.2.7), a formal expression for the complex envelope  $A(\mathbf{r})$  is obtained. Consecutively, by replacing it into Eq. (2.2.4), a complete mathematical representation for the field distribution  $U(\mathbf{r})$  of a Gaussian beam is established as follows [KL66][Nag10]:

$$U(x, y, z) = E_0 \frac{w_0}{w(z)} \cdot \overbrace{e^{-\left(\frac{\rho}{w(z)}\right)^2}}^{\text{Amplitude factor}} \cdot \underbrace{e^{-i\left(kz - \Phi + \frac{k\rho^2}{2R(z)}\right)}}_{\text{Phase factor}}. \quad (2.2.18)$$

In the last equation, the amplitude factor accounts for the Gaussian distribution of the beam radial (transverse) to the propagation axis. On the other hand, in the

phase factor term:  $kz$  defines the phase shift of a plane wave which together with the Gouy phase  $\Phi$  determine the general longitudinal phase shift of the beam, and  $\frac{k\rho^2}{2R(z)}$  describes the transverse phase shift of the beam with regard to a plane perpendicular to the propagation axis.

## 2.3 Higher-order modes

As mentioned earlier, each solution of Eq. (2.2.6) is a propagation mode of a monochromatic wave. In the previous section, the fundamental mode solution was analyzed, which corresponds to the Gaussian beam.

High order solutions in Cartesian coordinates are called *Hermite-Gaussian modes*. These modes do not have a transverse Gaussian intensity distribution. The complex envelope associated with them is given by [KL66][PLL<sup>+</sup>19]:

$$A(\mathbf{r}) = g(x, z)h(y, z)e^{-i\frac{k}{2q(z)}(x^2+y^2)}e^{-iP(z)}. \quad (2.3.1)$$

Because  $g$  is a function of  $x$  and  $z$ , and  $h$  of  $y$  and  $z$ , these solutions allow now differences in the  $x$  and  $y$  axis which lead to the non-Gaussian beam shape. After introducing Eq. (2.3.1) into Eq. (2.2.6),  $g$  and  $h$  are related to each other by [ST07]:

$$g \cdot h = H_m \left( \frac{\sqrt{2}x}{w(z)} \right) \cdot H_n \left( \frac{\sqrt{2}y}{w(z)} \right), \quad (2.3.2)$$

where  $m$  and  $n$  are the transverse mode numbers, with  $H_m$  and  $H_n$  known as the Hermite polynomial of order  $m$  and  $n$ , respectively. Examples of some low-order polynomials are:

$$H_0(v) = 1. \quad (2.3.3)$$

$$H_1(v) = 2v. \quad (2.3.4)$$

$$H_2(v) = 4v^2 - 2. \quad (2.3.5)$$

$$H_3(v) = 8v^3 - 12v. \quad (2.3.6)$$

Finally, all the functions that satisfy the paraxial wave equation (2.2.6) (this means, contemplating the Gaussian beam mode and the Hermite-Gaussian modes), are grouped in the following general expression [KL66][ST07]:

$$U(x, y, z)_{mn} = \frac{w_0}{w(z)} \cdot H_m \left( \frac{\sqrt{2}x}{w(z)} \right) \cdot H_n \left( \frac{\sqrt{2}y}{w(z)} \right) \cdot e^{-\left(\frac{\rho}{w(z)}\right)^2} \cdot e^{-i \left( kz - (1+m+n)\Phi + \frac{k\rho^2}{2R(z)} \right)}. \quad (2.3.7)$$

Overall, because of the transverse dependence of the modes, the fundamental Gaussian mode is normally denoted as the  $TEM_{00}$  mode and the high-order modes as the  $TEM_{mn}$  modes, where  $TEM$  stands for transverse electromagnetic. Fig. 2.2 shows the intensity profile distribution of some high-order modes.

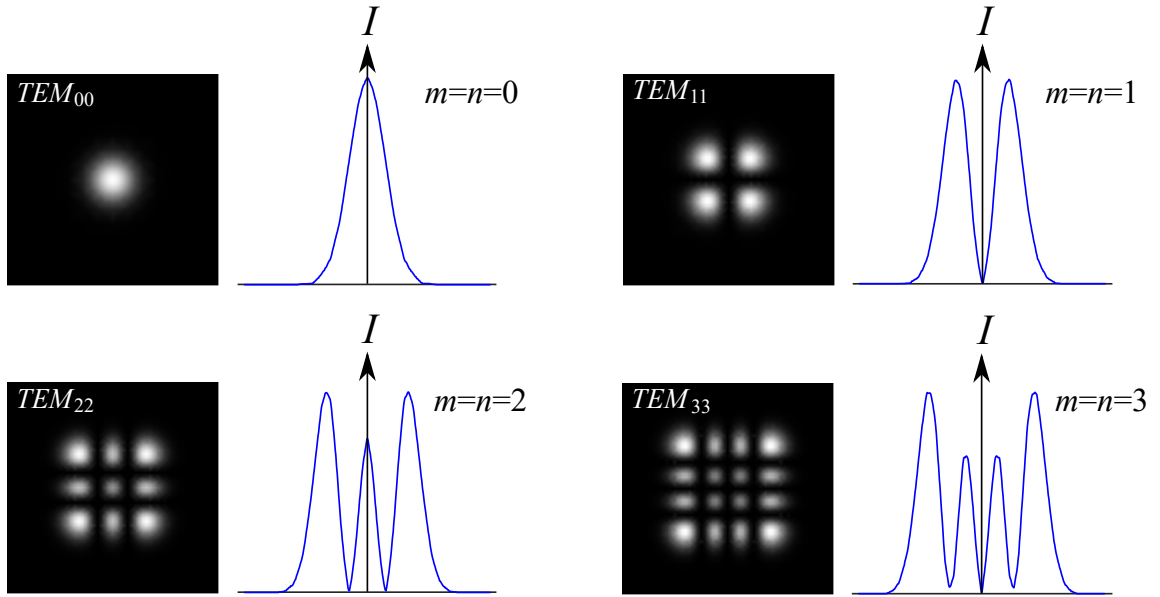


**Figure 2.2:** A few Hermite-Gaussian beams with their corresponding intensity distribution for each plane.  $TEM_{00}$  mode corresponds to the fundamental Gaussian beam.

## 2.4 The ABCD matrix

In the postulates of ray optics, the light travels in form of rays. Under the paraxial approximation, a ray makes a small angle  $\beta \approx \sin(\beta)$  with respect to the optical axis.

This paraxial ray can be described by a  $2 \times 1$  column vector containing its height  $h$  and angle  $\beta$  as depicted in Fig. 2.3 [ST07].

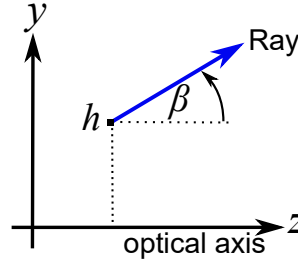


**Figure 2.3:** Paraxial ray defined by its height  $h$  and angle  $\beta$  with respect to the optical axis  $z$ .

When a ray defined by  $(h_1, \beta_1)$  travels along an optical system, it undergoes a linear transformation represented by a ray-transfer matrix called *ABCD matrix*. Thus, after the optical system, the ray is characterized by a new position and angle  $(h_2, \beta_2)$  which can be written in the form:

$$\begin{pmatrix} h_2 \\ \beta_2 \end{pmatrix} = \begin{pmatrix} A & B \\ C & D \end{pmatrix} \begin{pmatrix} h_1 \\ \beta_1 \end{pmatrix}, \quad (2.4.1)$$

where the real numbers  $A$ ,  $B$ ,  $C$  and  $D$  depend on the characteristics of the optical system. Besides, considering identical refractive indices before and after the optical system, the determinant of the ABCD matrix is unity [KL66]:

$$\det \begin{pmatrix} A & B \\ C & D \end{pmatrix} = AD - BC = 1. \quad (2.4.2)$$

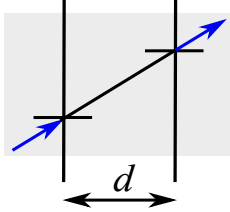
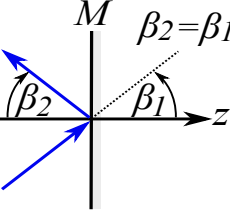
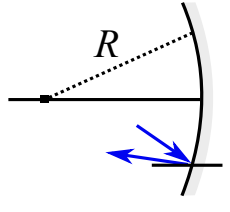
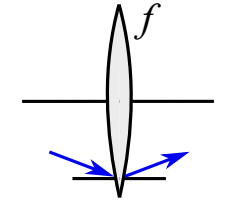
An optical system can be composed of an arrangement of different optical components where each one has its own ABCD matrix. Table 2.1 illustrates some optical components with their respective ray matrices.

The knowledge of the ray-transfer matrix is useful in order to understand the behavior of the Gaussian beam after the optical system associated with such a matrix. Specifically, defining  $1/q_0$  and  $1/q_1$  as the beam q-parameters (see Eq. (2.2.8)) before and after the optical system, respectively, the following q-transformation rule is fulfilled [KL66]:

$$\frac{1}{q_1} = \frac{C + D \left(\frac{1}{q_0}\right)}{A + B \left(\frac{1}{q_0}\right)}. \quad (2.4.3)$$

The last equation implies that the spot size of the beam and the radius of curvature of the wavefront can be calculated immediately after the optical system and, from there, at all points throughout the path of the beam.

**Table 2.1:** Optical components and their associated ABCD matrices

Case	Scheme	ABCD matrix
Free-space propagation of length $d$		$\begin{pmatrix} 1 & d \\ 0 & 1 \end{pmatrix}$
Reflection from a flat mirror $M$		$\begin{pmatrix} 1 & 0 \\ 0 & 1 \end{pmatrix}$
Reflection from a spherical mirror with radii of curvature $R$ and center to the left		$\begin{pmatrix} 1 & 0 \\ -\frac{2}{R} & 1 \end{pmatrix}$
Transmission through a thin lens of focal length $f$		$\begin{pmatrix} 1 & 0 \\ -\frac{1}{f} & 1 \end{pmatrix}$

## 2.5 The two-mirror enhancement cavity

An optical cavity, also called optical resonator, is a set of two or more mirrors arranged in such a way that causes an incident light, weakly transmitted through one of the mirrors, to circulate in a closed path reflected within the mirrors, coupling and being coherently stored at a certain resonant frequency. The enhancement is a factor that reflects the ability of the cavity to build up or enhance passively the input light certain number of times whose value will depend on the cavity features.

The two-mirror cavity is the simplest optical cavity and it is basically a Fabry-Perot interferometer [ST07][YY07] with two facing highly-reflective curved mirrors with radii of curvature  $R_1$  and  $R_2$  separated by a distance  $d$ . Distinct types of two-mirror cavities exist that differ from each other in the value of the radius of curvature and in the separation between the mirrors. Fig. 2.4 depicts a symmetric configuration of a two-concave-mirror resonator which will be used as a model in the analysis of this section.

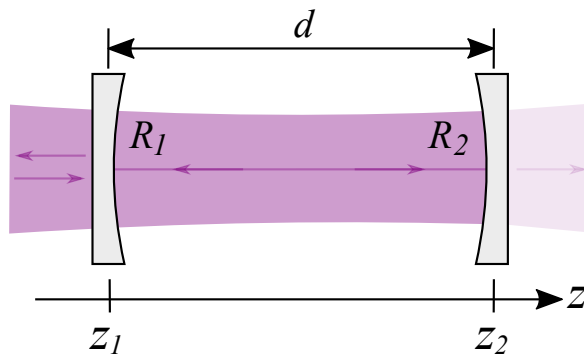


**Figure 2.4:** A symmetric two-concave-mirror resonator. Because the mirrors are not perfectly reflective, there is a small light leakage along them.

The light circulates in sequences inside the resonator of Fig. 2.4. First, the beam enters through the input coupler mirror  $R_1$ . Next, it travels forward along  $d$ . Then, it is reflected on the mirror  $R_2$ . After that, it travels the path  $d$  backwards. And finally, it is reflected by  $R_1$  repeating the whole sequence over and over. The right-traveling wave and the left-traveling wave in the resonator generate an interference pattern, which is why this cavity is also called *the two-mirror standing wave resonator*.

Similar to the light beam modes, a cavity also has uncountable possible modes. In order for a cavity mode to happen, it requires, as condition, that after one round-trip the field distribution of the light and its phase replicate themselves inside the resonator. This brings about the interference pattern. Thus, when both are fulfilled, the mode associated with the input light beam is a mode of the cavity, in other words, there is a successful mode matching between the input beam mode and a specific cavity mode.

### 2.5.1 Field distribution condition

Inside the cavity, the wavefronts normal to the propagation axis will reflect back onto themselves, always retracing the same path as long as the mirror surfaces coincide with the wavefronts. In order to find out the light field distribution in the resonator, a simple analysis can be performed using the ABCD q-transformation rule described in the foregoing section [KL66]. Specifically, taking just to the right of  $R_1$  as the reference plane, if  $1/q_p$  is the complex beam parameter at this plane, then after one round-trip the condition has to comply with the following:

$$\frac{1}{q_p} = \frac{C + D \left( \frac{1}{q_p} \right)}{A + B \left( \frac{1}{q_p} \right)}, \quad (2.5.1)$$

whose solution leads to:

$$\frac{1}{q_p} = \frac{D - A}{2B} \pm \frac{1}{2B} \sqrt{(A - D)^2 + 4BC}. \quad (2.5.2)$$

Analogously to Eq. (2.2.8), the first term of Eq. (2.5.2) is related to  $1/R$  – where  $R$  is the radius of curvature of the wavefront at the reference plane – and the second one to  $i\lambda/\pi w^2$  as follows:

$$\begin{aligned} \frac{1}{R} &= \frac{D - A}{2B} \\ R &= \frac{2B}{D - A}. \end{aligned} \quad (2.5.3)$$

$$\begin{aligned} w^2 &= \frac{2|B|\lambda i}{\pi \sqrt{(A - D)^2 + 4BC}} \\ w^2 &= \frac{2|B|\lambda i}{\pi \sqrt{A^2 + 2AD + D^2 - 4AD + 4BC}} \\ w^2 &= \frac{2|B|\lambda}{\pi \sqrt{4 - (A + D)^2}}. \end{aligned} \quad (2.5.4)$$

The beam radius  $w$  is a real number. Therefore, the term under the square root in



Eq. (2.5.4) must be positive. In other words, to have a physically valid value of  $w$  it is necessary to fulfill the following inequality:

$$-2 < (A + D) < 2. \quad (2.5.5)$$

This inequality is called the *stability criterion*. If it is fulfilled, the cavity is stable, meaning that the field successfully replicates itself after one round-trip [Nag10].

As mentioned before, the light in the cavity travels back and forth between the mirrors experiencing a repetitive sequence. Keeping the reference plane, in Fig. 2.4 one round-trip sequence is composed of four elements: the free-space propagation of distance  $d$ , the reflection by mirror  $R_2$ , the second free-space propagation of distance  $d$ , and the reflection by mirror  $R_1$ . Therefore, by following Table 2.1 and writing the matrices of each optical component in reverse order [Nag10], the ABCD matrix of a one round-trip sequence is equal to:

$$\begin{pmatrix} A & B \\ C & D \end{pmatrix} = \begin{pmatrix} 1 & 0 \\ -\frac{2}{R_1} & 1 \end{pmatrix} \begin{pmatrix} 1 & d \\ 0 & 1 \end{pmatrix} \begin{pmatrix} 1 & 0 \\ -\frac{2}{R_2} & 1 \end{pmatrix} \begin{pmatrix} 1 & d \\ 0 & 1 \end{pmatrix}. \quad (2.5.6)$$

The preceding expression produces the following matrix elements:

$$A = 2 \left( 1 - \frac{d}{R_2} \right) - 1, \quad (2.5.7)$$

$$B = 2 \left( 1 - \frac{d}{R_2} \right) d, \quad (2.5.8)$$

$$C = \frac{2}{d} \left[ 2 \left( 1 - \frac{d}{R_1} \right) \left( 1 - \frac{d}{R_2} \right) - \left( 1 - \frac{d}{R_1} \right) - \left( 1 - \frac{d}{R_2} \right) \right], \quad (2.5.9)$$

$$D = 4 \left( 1 - \frac{d}{R_1} \right) \left( 1 - \frac{d}{R_2} \right) - 2 \left( 1 - \frac{d}{R_2} \right) - 1. \quad (2.5.10)$$

Consequently, by replacing Eqs. (2.5.7) and (2.5.10) into Eq. (2.5.5), the stability criterion turns into:

$$0 < \left( 1 - \frac{d}{R_1} \right) \left( 1 - \frac{d}{R_2} \right) < 1. \quad (2.5.11)$$

In the literature [KL66][Nag10][ST07], for a simpler analysis, the criterion is written in terms of the quantities  $g_1 = (1 - d/R_1)$  and  $g_2 = (1 - d/R_2)$  known as *g parameters*. Hence, Eq. (2.5.11) becomes:

$$0 < g_1 g_2 < 1. \quad (2.5.12)$$

Fig. 2.5 illustrates a 2-D plot of the criterion (2.5.12) in terms of  $g_1$  and  $g_2$ . Basically, this diagram indicates the regions of stability. On the one hand, to fulfill the inequality on the left ( $0 < g_1 g_2$ ), all the stable points must be in the first or third quadrants. On the other hand, to accomplish the inequality on the right ( $g_1 g_2 < 1$ ), the stable points must be in a region bounded by the hyperbola  $g_1 g_2 = 1$  [Nag10][ST07]. In summary, resonators located in the shaded area are stable. Otherwise, they are unstable. Furthermore, the configuration of some common stable resonators is depicted in the diagram.

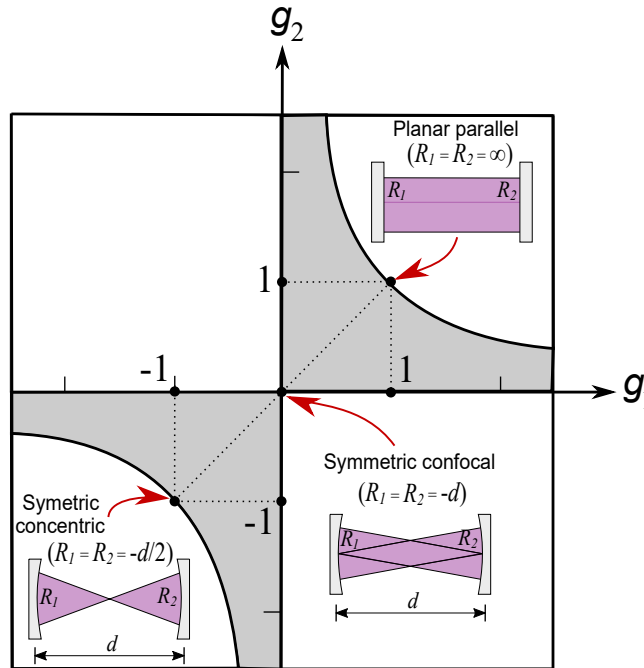


**Figure 2.5:** Stability diagram in a two-mirror cavity with examples of some common stable symmetric resonators.

In the design process of a two-mirror resonator with specific characteristics (type and size of mirrors, cavity length, etc...), the parameters of the fundamental (Gaussian) beam mode inside the resonator can be calculated by substituting the values of the *ABCD* elements into the different equations seen so far. In particular, Eq. (2.5.4)

provides the result of the spot size  $w$  at the position just at the right of mirror  $R_1$ . Consecutively, by replacing  $w$  into Eq. (2.2.10), expressions for the waist size  $w_0$  and the Rayleigh length  $z_R$  can be directly obtained. Afterward, matching the input beam field mode and the cavity resonant beam mode guarantees a coupling of the incident light into the resonator, provided that the phase condition is also satisfied.

## 2.5.2 Phase condition: Resonance frequencies

As mentioned earlier, the phase of the Gaussian mode also has to reproduce itself in the resonator after one round-trip. If this happens, the beam frequency is at resonance with the cavity mode. In such a circumstance, after each round-trip, the beam phase shift  $\delta$  is an integral multiple of  $2\pi\Upsilon$ , with  $\Upsilon = 1, 2, 3, \dots$

For the fundamental mode, looking at Eq. (2.2.18) and following Fig. 2.4, at points on the optical axis ( $\rho = 0$ ) the beam phase is  $\delta = kz - \Phi$ . Therefore, by accomplishing the resonance condition after the beam propagates back and forth between  $z_1$  at mirror  $R_1$  and  $z_2$  at mirror  $R_2$  (the total displacement is 2 times the cavity length), the beam phase change is equal to  $\Delta\delta = 2dk - 2\Delta\Phi = 2\pi\Upsilon$ , where  $\Delta\Phi = \Phi(z_2/z_R) - \Phi(z_1/z_R)$ , with  $\Phi$  defined by Eq. (2.2.17). This leads to a formal expression of the resonance frequencies as follows [Nag10][ST07]:

$$\nu_\Upsilon = \left( \Upsilon + \frac{\Delta\Phi}{\pi} \right) \frac{c}{2d}. \quad (2.5.13)$$

In the case of higher-order modes (see section 2.3), at points on the optical axis the phase  $\delta$  depends on the indexes  $m$  and  $n$  like this:  $\delta = kz - (1 + m + n)\Phi$ . Thereby, following a similar procedure, a global expression of the resonance frequencies in a two-mirror optical cavity is finally given by [Nag10][ST07]:

$$\nu_{\Upsilon,m,n} = \left[ \Upsilon + (1 + m + n) \frac{\Delta\Phi}{\pi} \right] \frac{c}{2d}. \quad (2.5.14)$$

In the last two equations, the term  $c/2d$  is the distance between neighboring frequency modes and is known as *free spectral range* (FSR). In terms of  $\delta$ ,  $\text{FSR} = 2\pi$ .

### 2.5.3 Intensity relations

Losses in a resonator are attributable to the mirrors and the medium between them. In the case studied here, the cavity is immersed in a passive loss-less medium (free-space). Each mirror is described by its amplitude reflection and transmission coefficients  $r$  and  $t$ , as well as its intensity reflectance  $R = |r|^2$  and transmittance  $T = |t|^2$ , respectively. A real mirror satisfies  $R + T + M_L = 1$ , where  $M_L$  is the mirror losses due to mainly absorption, scattering, and diffraction phenomena [YY07].

In order to understand more clearly the amount of light inside, reflected and transmitted by the optical cavity, the two-flat-mirror resonator shown in Fig. 2.6 is considered. In this scheme are assumed a normal incident plane wave with complex amplitude  $E_0$ , and loss-less mirrors ( $M_L = 0$ ) with reflection coefficients  $r_1$  and  $r_2$  and transmission coefficients  $t_1$  and  $t_2$ , respectively. Thus, it follows that: the total amplitude of the reflected light is  $E_r = A_1 + A_2 + A_3 + \dots + A_n$ , the total amplitude of the right-going circulating light is  $E_c = C_1 + C_2 + C_3 + \dots + C_n$ , and the total amplitude of the transmitted light is  $E_t = B_1 + B_2 + B_3 + \dots + B_n$ .

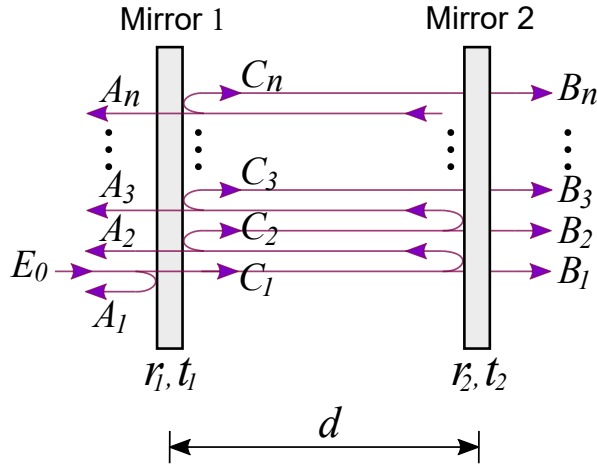


**Figure 2.6:** Two-flat-mirror resonator with the reflected, circulating and transmitted amplitude field from the first to the  $n$  round-trip.

Considering the first three round-trip passes of the light inside the cavity with the respective round-trip phase shift  $\delta = 2kd$  for a plane wave, and knowing that the intensity is related to the amplitude field by  $I = |E|^2$ , then the intensity of the total reflected light  $I_r$ , the total right-going circulating intracavity light  $I_c$  and the total transmitted light  $I_t$  can be approximated as follows [Nag10][ST07][YY07]:

$$I_r = |E_r|^2 = I_0 \frac{(r_1 - r_2)^2 + 4r_1r_2 \sin^2 \delta/2}{(1 - r_1r_2)^2 + 4r_1r_2 \sin^2 \delta/2} \quad (2.5.15)$$

$$I_c = |E_c|^2 = I_0 \frac{t_1^2}{(1 - r_1 r_2)^2 + 4r_1 r_2 \sin^2 \delta/2} \quad (2.5.16)$$

$$I_t = |E_t|^2 = I_0 \frac{(1 - r_1 r_2)^2}{(1 - r_1 r_2)^2 + 4r_1 r_2 \sin^2 \delta/2}. \quad (2.5.17)$$

By using the previous definitions, the following important properties are defined.

### Finesse ( $\mathcal{F}$ )

The finesse  $\mathcal{F}$  is a parameter that measures the quality of the cavity at resonance ( $\delta=0$  or multiple of  $2\pi$ ) which is directly connected with the enhancement factor. It corresponds to the number of bounces that the beam makes before being absorbed or leaked [You14]. It is denoted by:

$$\mathcal{F} = \frac{\pi\sqrt{r_1 r_2}}{1 - r_1 r_2} = \frac{FSR}{FWHM}, \quad (2.5.18)$$

where  $FSR=c/2d$  is the free spectral range previously defined in section 2.5.2, and  $FWHM$  is the full width at half maximum of the circulating light at resonance (cavity linewidth) defined as:

$$FWHM = \frac{2(1 - r_1 r_2)}{\sqrt{r_1 r_2}}. \quad (2.5.19)$$

### The decay time ( $t_c$ )

At resonance, the energy stored  $\xi$  in the cavity decays with time through the decay time  $t_c$  [Nag10, YY07, IMK<sup>+</sup>13] which is defined as the average time that the beam lives in the cavity before being dissipated due to cavity losses. Their relation is stated by the energy loss rate  $d\xi/dt$ :

$$\frac{d\xi}{dt} = -\frac{\xi}{t_c}. \quad (2.5.20)$$

In passive resonators, the fractional intensity loss per round-trip  $L_T$  (attributable to the transmittance of the mirrors) can be specified by the field reflection coefficients of the mirrors as  $L_T = 1 - r_1^2 r_2^2$ . Therefore, the energy loss per round-trip would be

$L_T\xi$ . Moreover, considering the round-trip distance  $2d$  and the light velocity  $c$ , the loss per unit length corresponds to  $(1/2d)L_T\xi$  while  $(c/2d)L_T\xi$  would represent the loss per unit time. Consequently, Eq. (2.5.20) can be also written as:

$$\frac{d\xi}{dt} = - \left( \frac{c}{2d} \right) L_T\xi. \quad (2.5.21)$$

Finally, by matching Eqs. (2.5.20) and (2.5.21), the expression for  $t_c$  becomes:

$$t_c = \frac{2d}{cL_T} = \frac{\mathcal{F}}{\pi \cdot FSR}. \quad (2.5.22)$$

### The $Q$ factor

Another important cavity property is the  $Q$  factor or quality factor. Basically, it is a quantity that measures the effectiveness of the cavity to store energy. It is proportional to the stored energy inside the cavity and the energy decay per unit time (loss rate) as follows [Nag10][ST07][YY07]:

$$Q = -\frac{\omega \times \xi}{d\xi/dt}, \quad (2.5.23)$$

where  $\omega = 2\pi\nu$  with  $\nu$  being the resonance frequency. By replacing Eqs. (2.5.20) and (2.5.22) into Eq. (2.5.23),  $Q$  is defined as:

$$Q = 2\pi\nu t_c = \frac{2d\mathcal{F}}{\lambda}. \quad (2.5.24)$$

A high  $\mathcal{F}$  implies a high  $Q$  which means the light is stored and built up appropriately, staying longer inside the cavity.

### 2.5.4 Impedance matching and enhancement factor ( $\mathcal{E}$ )

In the design of an enhancement cavity, a maximum circulating power inside the resonator (highest possible  $\mathcal{F}$ ) is desirable. Such a state is reached when, at resonance, most of the input light is coupled into the cavity with a minimum amount (ideally zero) reflected by the input coupling mirror. Under such a scenario, the resonator is said to be impedance matched. In terms of the cavity parameters, the impedance matching

case happens when the intensity transmission coefficient  $T_1 = t_1^2$  of the input coupling mirror is equal to the sum of all the other round-trip losses  $L$  in the resonator excluding the input coupler, i.e.,  $L$  includes the transmission coefficient  $T_2 = t_2^2$  of the second cavity mirror as well as the total possible absorption and scattering losses  $O_L$  [Nag10][Car16]. Then, the cavity can be categorized in terms of impedance coupling conditions as follows [Bre18][RCGM10]:

$$T_1 = L \text{ (or } R_1 = R_2) \quad \text{Impedance matched} \quad (2.5.25)$$

$$T_1 < L \quad \text{Under coupled} \quad (2.5.26)$$

$$T_1 > L \quad \text{Over coupled} \quad (2.5.27)$$

where  $L = 1 - R_1 = T_2 + O_L$ .

As mentioned before, the number of times that the intensity of the cavity input light increases inside the cavity at resonance is known as *enhancement factor*  $\mathcal{E}$ . It is given by the ratio between the intensity  $I_c$  of the cavity circulating light and the intensity  $I_0$  of the cavity input light. Applying the resonance condition  $\delta = 0$  over Eqs. (2.5.15) and (2.5.16),  $I_r$  and  $I_c$  become:

$$I_r = \frac{I_0(r_1 - r_2)^2}{(1 - r_1 r_2)^2}. \quad (2.5.28)$$

$$I_c = \frac{I_0 t_1^2}{(1 - r_1 r_2)^2}. \quad (2.5.29)$$

Thus,  $\mathcal{E}$  is given by:

$$\mathcal{E} = \frac{I_c}{I_0} = \frac{t_1^2}{(1 - r_1 r_2)^2}. \quad (2.5.30)$$

At the impedance matching instance,  $\mathcal{E}$  is directly bound to the finesse as described in Eq. (2.5.31) [Nag10][Bre18][Ham07]. In this equation, since the equality  $T_1 = L$  is satisfied, it can be intuitively seen that for a higher  $\mathcal{E}$  it is essential to reduce the cavity losses as much as possible.

$$\mathcal{E} = \frac{I_c}{I_0} = \frac{1}{T_1} = \frac{\mathcal{F}}{\pi}. \quad (2.5.31)$$

As a final comment, the decision to study the two-mirror optical cavity was made because it provides a good theoretical framework to understand the four-mirror bow-tie cavity behavior. Basically, both resonators share the same type of definitions, therefore the analysis of the bow-tie configuration can be performed through a similar procedure to the one developed throughout this section, as will be shown in the next chapter.



---

# Chapter 3

## The bow-tie enhancement cavity

### 3.1 Introduction

Chapter 2 provided general concepts about the two-mirror optical cavity. The most distinctive aspect of such a resonator was the generation of a standing-wave pattern of the resonant light between its mirrors. However, by incrementing the number of mirrors, it is possible to build another type of optical cavity in which the beam inside does not move back and forth anymore, but it only experiences a unique direction, as in a circulating loop behavior. This kind of resonator is called *traveling wave cavity* or *ring cavity*.

There are different ways to set up a traveling-wave enhancement cavity, depending on the number of mirrors. In particular, this thesis implements a symmetrical bow-tie configuration, which consists of two flat mirrors and two concave mirrors. As in the two-mirror cavity, this configuration also has the goal of coupling and storing light at a certain resonance frequency by always fulfilling the field and phase conditions. In addition, it is used, e.g., in many laser-based systems as a cavity with an intracavity nonlinear crystal in frequency generation and discrimination processes [MCH96][SM90][YIO<sup>+</sup>96] and in regenerative amplifiers for the amplification of ultrashort pulses [DCH<sup>+</sup>20], among others.

This chapter presents, following a similar method as the two-mirror resonator, the most important properties of the bow-tie configuration, as well as its design and mounting process with the corresponding experimental results.

### 3.2 Definition and design

Fig. 3.1 illustrates a model of the bow-tie cavity configuration. This consists of two similar concave mirrors CM1 and CM2 with the same radius of curvature  $R_{CM}$ , and two flat mirrors FM and ICM, where the latter acts as an input light coupler mirror. All of them are aligned in such a way that when an incident beam enters through the ICM, the light follows the curl formed by paths  $d_1$ ,  $d_2$ ,  $d_3$  and  $d_4$ , creating two waists with different sizes: a bigger one within the flat mirrors and a smaller one between the spherical mirrors. According to the design developed in this thesis, in the following picture  $d_1 = d_3$  and  $d_2 = d_4$  but depending on the specific application they may have different lengths.

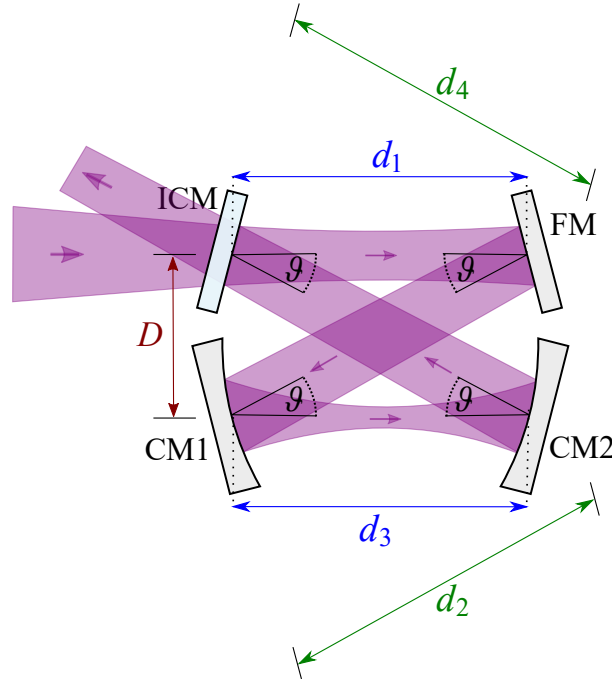


**Figure 3.1:** Bow-tie resonator model.

The bow-tie configuration was chosen for three main reasons. Firstly, because it enables the variation and control of the size of both beam waists for a specific input light frequency by adjusting the length of the paths and the mirrors angle. Secondly, because it has the advantage that the light between the mirrors travels in a single direction. This is crucial at the moment of extracting the circulating accumulated field. And finally, because the input light is reflected from the ICM at a non-normal angle, which prevents unwanted multiple reflections that distort the beam and avoids damages

in the light source due to non-desirable re-entering light.

The main disadvantage is the presence of *astigmatism* which is another important peculiarity of ring resonators. It occurs due to off-axis reflection from the curved mirrors, causing differences between the focus positions of the sagittal and tangential planes [Nag10].

The designed cavity is made for an incident fundamental Gaussian beam of  $\lambda = 3$  mm of wavelength, which corresponds to  $\nu = 100$  GHz in the frequency domain. Due to this frequency range, it is valid to say that the resonator presented here is a quasi-optical cavity that follows the principles of optical cavities. Its dimensions and some parameters are shown in Table 3.1 (see [RUS<sup>+</sup>12] and [PSTS17] for design procedures). The bow-tie geometry used in this thesis satisfies the need to have enough space between the concave mirrors with the smallest beam waist and the minimum level of astigmatism possible halfway among these mirrors.

**Table 3.1:** Dimensions and some parameters of the designed ring resonator

Parameter	Value
$d_1 = d_3$	210 mm
$d_2 = d_4$	240 mm
Total cavity length $d = 2(d_1 + d_2)$	900 mm
Cavity width ( $D$ )	120 mm
$\vartheta$	$30^\circ$
Radius of curvature ( $R_{CM}$ ) of CM1 and CM2	186 mm
Round-trip time (traveling time)	3 ns

There are alternative methods to design ring resonators that are widespread to cavities with a higher number of mirrors [QXZ<sup>+</sup>14][AS04]. However, a general analysis can be performed by following a strategy that is similar to the two-mirror case.

A special interest lies in knowing the size of the two beam waists present in the configuration. In order to calculate them, first it is necessary to determine the round-trip ABDC matrix. Looking at Fig. 3.1, by choosing as reference plane the location just at the right of the concave mirror CM1, the matrix is formed by: the free space propagation  $d_3$ , the reflection by mirror CM2, the free propagation  $d_4$ , the reflection by mirror

ICM, the free propagation  $d_1$ , the reflection by mirror FM, the free propagation  $d_2$ , and the reflection by mirror CM1. Then, by following Table 2.1 with the values of Table 3.1, the round-trip ray transfer matrix of the designed cavity is given by:

$$\begin{aligned} \begin{pmatrix} A_0 & B_0 \\ C_0 & D_0 \end{pmatrix} &= \begin{pmatrix} 1 & 0 \\ -2/R_{CM} & 1 \end{pmatrix} \begin{pmatrix} 1 & d_1 + 2d_2 \\ 0 & 1 \end{pmatrix} \begin{pmatrix} 1 & 0 \\ -2/R_{CM} & 1 \end{pmatrix} \begin{pmatrix} 1 & d_1 \\ 0 & 1 \end{pmatrix} \\ \begin{pmatrix} A_0 & B_0 \\ C_0 & D_0 \end{pmatrix} &= \begin{pmatrix} -6.419 & -658.064 \\ 0.0582 & 5.817 \end{pmatrix}. \end{aligned} \quad (3.2.1)$$

Next, the replacement of the previous matrix elements into Eq. (2.5.2) leads to the following q-parameter:

$$\frac{1}{q_{p0}} = -0.0093 - 0.0014i. \quad (3.2.2)$$

Afterward, by replacing Eq. (3.2.2) into Eq. (2.2.12) and consecutively into Eq. (2.2.13), the Rayleigh length  $z_{R0}$  and the beam waist  $w_0$  among the concave mirrors are equal to:

$$z_{R0} = -\frac{\text{Im} \left\{ \frac{1}{q_{p0}} \right\}}{\left| \frac{1}{q_{p0}} \right|^2} = 16.3663 \text{ mm}. \quad (3.2.3)$$

$$w_0 = \sqrt{\frac{\lambda z_{R0}}{\pi}} = 3.9533 \text{ mm}. \quad (3.2.4)$$

The second beam waist between ICM and FM can be calculated by using the q-transformation rule. Traveling in reverse from the reference plane to the location just to the left of mirror CM1,  $1/q_{pM}$  is determined from  $1/q_{p0}$  through Eq. (2.5.1) in the following way:

$$\frac{1}{q_{pM}} = \frac{C_M + D_M \left( \frac{1}{q_{p0}} \right)}{A_M + B_M \left( \frac{1}{q_{p0}} \right)} = 0.0015 - 0.0014i. \quad (3.2.5)$$

where  $\begin{pmatrix} A_M & B_M \\ C_M & D_M \end{pmatrix} = \begin{pmatrix} 1 & 0 \\ 2/R_{CM} & 1 \end{pmatrix} = \begin{pmatrix} 1 & 0 \\ 0.0108 & 1 \end{pmatrix}$ . Here the term  $2/R_{CM}$  is positive because the beam moves in a reverse direction.

Then, by substituting Eq. (3.2.5) into Eqs. (2.2.12) and (2.2.13), the Rayleigh length  $z_{RM}$  and the beam waist  $w_{0M}$  between ICM and FM result in:

$$z_{RM} = -\frac{Im\left\{\frac{1}{q_{pM}}\right\}}{\left|\frac{1}{q_{pM}}\right|^2} = 343.6932 \text{ mm}. \quad (3.2.6)$$

$$w_{0M} = \sqrt{\frac{\lambda z_{RM}}{\pi}} = 18.1164 \text{ mm}. \quad (3.2.7)$$

Finally, by replacing  $A_0 = -6.4194$  and  $D_0 = 5.8179$  into the already known criterion (2.5.5), the designed cavity fulfills the stability condition, as proven in Eq. (3.2.8).

$$\begin{aligned} -2 &< (A + D) < 2 \\ -2 &< -0.6015 < 2. \end{aligned} \quad (3.2.8)$$

Overall, with a fixed reference plane, the beam features can be computed in different positions by choosing a specific location of interest and following a procedure similar to the one shown above. Nevertheless, independently of the position under study, the beam waist presents variations among its sagittal and tangential plane due to the astigmatism aberration [RUS<sup>+</sup>12], which was not considered in the last calculations. Therefore,  $w_0$  in Eq. (3.2.4) is the average value between the sagittal and tangential beam waist among the concave mirrors, and  $w_{0M}$  in Eq. (3.2.7) is the average value between the sagittal and tangential beam waist among ICM and FM.

If the astigmatism is now incorporated in the analysis, the following simulated graphs show, with detail, the Gaussian beam propagation throughout the entire bow-tie resonator with the respective beam profiles at certain points. According to Fig. 3.3, thanks to the appropriate choice of the small folding angle  $\vartheta/2 = 15^\circ$  of the mirrors and to the suitable length of the biggest path  $d1$  and the width  $D$  compared with the total cavity length  $d$  [CHK<sup>+</sup>13], the effect of the astigmatism at waist  $w_0$  is considerably reduced, resulting in an almost circular shape beam in that position.

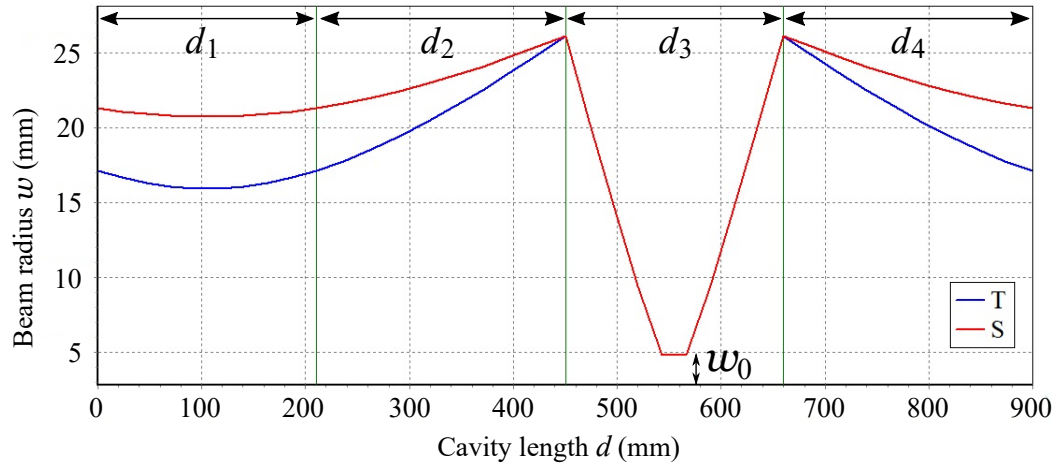


**Figure 3.2:** Simulated beam propagation along the bow-tie cavity.

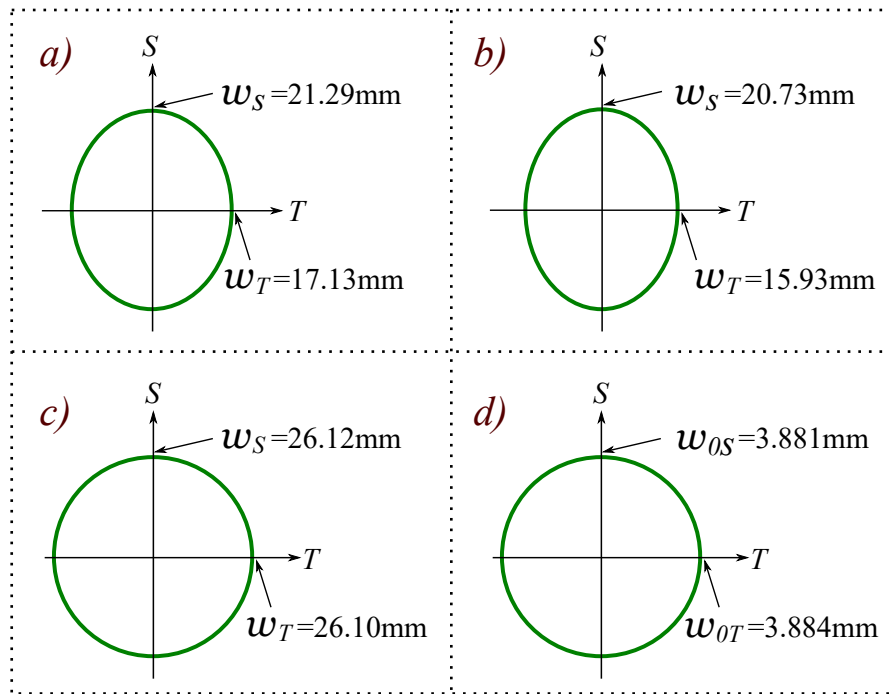


**Figure 3.3:** Simulated beam profiles at certain cavity planes: a) at ICM; b) at  $d_1/2$ ; c) at any of concave mirrors; d) at the center between CM1 and CM2. The calculated  $w_0$  in Eq. (3.2.4) is similar to the simulated beam waist in figure d).

Furthermore, Eq. (3.2.9) is the mathematical expression for the resonance frequencies in ring resonators [Nag10][RUS<sup>+</sup>12][CCM<sup>+</sup>19]. It shares a similar expression to Eq. (2.5.14) and was obtained after fulfilling the same round trip phase shift condition of  $\delta = 2\pi\Upsilon$ , with  $\Upsilon = 1, 2, 3, \dots$ , except that now the total cavity round trip length is

$d = d_1 + d_2 + d_3 + d_4 = 2(d_1 + d_2)$ , which leads to a free spectral range of  $\text{FSR} = c/d$  (or  $2\pi$  in terms of  $\delta$ ).

$$\nu_{\Upsilon} = \left[ \Upsilon + (1 + m + n) \frac{\Delta\Phi}{\pi} \right] \frac{c}{d}. \quad (3.2.9)$$

In the case of the designed cavity, the term  $\Delta\Phi$  is the Gouy phase difference given by  $\Delta\Phi = \Phi(z_2/z_{RM}) - \Phi(z_1/z_{R0})$ , where  $z_2$  is the distance from the reference plane to the waist  $w_{0M}$  and  $z_1$  is the distance from the reference plane to the waist  $w_0$ . Therefore, it is deduced that:

$$\begin{aligned} \frac{\Delta\Phi}{\pi} &= \left[ \tan^{-1} \left( \frac{z_2}{z_{RM}} \right) - \tan^{-1} \left( \frac{z_1}{z_{R0}} \right) \right] \frac{1}{\pi}, \\ \frac{\Delta\Phi}{\pi} &= \left[ \tan^{-1} \left( \frac{345}{343.6932} \right) - \tan^{-1} \left( \frac{105}{16.3663} \right) \right] \frac{1}{\pi} = -0.2. \end{aligned} \quad (3.2.10)$$

Finally, considering that the frequency of the fundamental Gaussian mode  $TEM_{00}$  ( $m=n=0$ ) of the cavity input radiation is  $\nu=100$  GHz and that the free spectral range is  $\text{FSR}=333,330$  MHz, therefore, by approximating  $\Delta\Phi/\pi \approx 0$ , the associated mode number  $\Upsilon$  in Eq. (3.2.9) is 300. The remaining parameters and properties of the bow-tie cavity will be analyzed in parallel with their equivalent experimental results.

### 3.3 Design of the input coupler mirror (ICM)

The input coupler mirror plays a fundamental role in the cavity operation. Specifically, choosing a suitable ICM, whose reflectance  $R_I$  and transmittance  $T_I$  at 100 GHz are appropriate for the characteristics of the cavity, allows an efficient light coupling with a high cavity enhancement factor.

In order to control  $R_I$  and  $T_I$ , the proposed design [AB77, YY07, YS05] of the ICM involves a Bragg reflector [IPI<sup>+</sup>17] composed of a multilayer structure of  $N$  layers built of wafers made of some material suitable for THz frequencies and separated from each other by an air gap of thickness  $l$ . Every wafer has the same thickness  $l$  and diameter  $\varnothing$  and all of them are considered transparent, therefore the Fresnel coefficients [BW03] and the phase change in each spread are real numbers (real refractive index). To be

more consistent with the analysis, the air gap will be also called and treated as a layer. The general scheme of the structure is shown in Fig. 3.4.

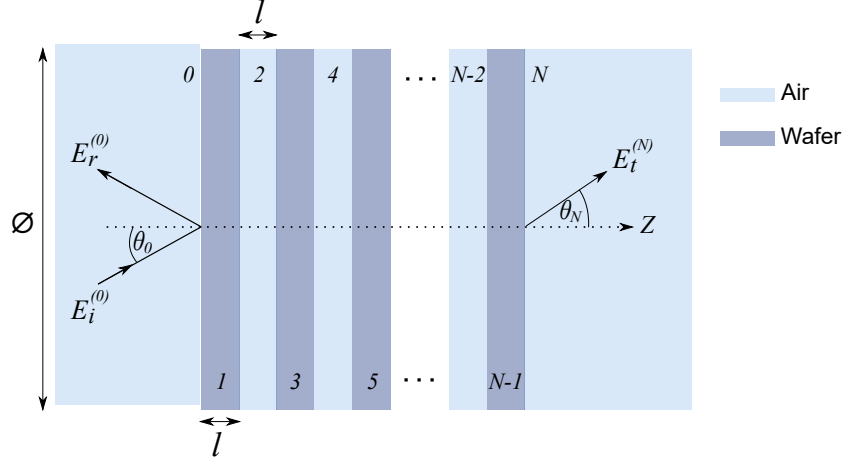


**Figure 3.4:** Scheme of a multilayer structure of  $N$  layers made by wafers and air gaps.

Calculating the total reflectance and transmittance of the whole structure of Fig. 3.4 is a challenging task because of the uncountable multiple reflections between the layers. However, by using the theory of the matrix transfer method the difficulty is considerably reduced, solving the problem in a more practical way. To this end, by assuming an incident plane wave onto the structure,  $E_i^{(0)}$  corresponds to the electric field amplitude of the input wave, whereas  $E_r^{(0)}$  and  $E_t^{(N)}$  correspond to the electric field amplitudes of the total reflected and transmitted output waves due to the multiple reflections. The light enters through the interface 0 (air) with an incidence angle  $\theta_0$  then spreads throughout the structure.  $\theta_N$  is the refractive angle throughout the interface  $N$  (air) which satisfies Snell's law [YF09] applied over all the previous interfaces respectively. Thus, the amplitudes of the fields on each side of the multilayer structure are related to each other by a  $2 \times 2$  complex transfer matrix  $M$ . The mathematical expression of this relation is given by:

$$\begin{aligned} \begin{pmatrix} E_i^{(0)} \\ E_r^{(0)} \end{pmatrix} &= M \begin{pmatrix} E_t^{(N)} \\ 0 \end{pmatrix} \\ \begin{pmatrix} E_i^{(0)} \\ E_r^{(0)} \end{pmatrix} &= \begin{pmatrix} M_{11} & M_{12} \\ M_{21} & M_{22} \end{pmatrix} \begin{pmatrix} E_t^{(N)} \\ 0 \end{pmatrix}, \end{aligned} \quad (3.3.1)$$



wherein  $M_{11}$ ,  $M_{12}$ ,  $M_{21}$  and  $M_{22}$  are the transfer matrix coefficients.

$M$  is formed by the multiplication of multiple matrices: the transmission matrix  $S$  between a border of two layers and the propagation matrix  $P$  throughout an interface. To simplify the analysis, Fig. 3.5 shows a scheme including just the first three layers of the structure of Fig. 3.4. This means that layer  $0$  = air, layer  $1$  = wafer and layer  $2$  = air.

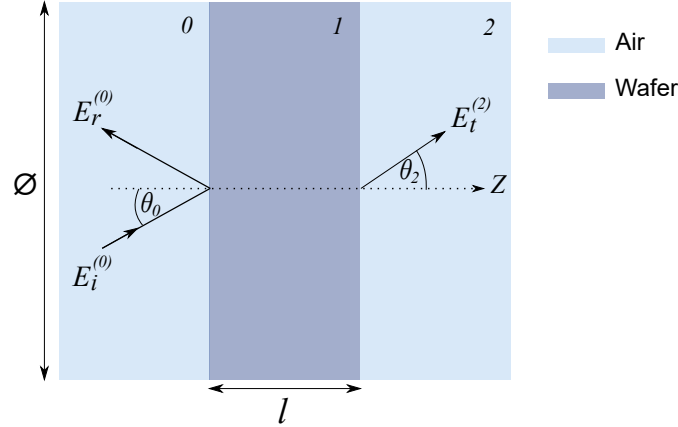


**Figure 3.5:** Scheme of the structure formed by layer  $0$  (air), layer  $1$  (wafer) and layer  $2$  (air).

Therefore, the transfer matrix  $M_{0,2}$  for the system air-wafer-air of Fig. 3.5 would be:

$$M_{0,2} = S_{01} \cdot P_1 \cdot S_{12}, \quad (3.3.2)$$

where  $S_{01}$  is the transmission matrix of the border between layers  $0$  and  $1$ ,  $P_1$  is the propagation matrix throughout layer  $1$ , and  $S_{12}$  is the transmission matrix of the border between the layers  $1$  and  $2$ .

In particular,  $S_{01}$  is given by:

$$S_{01} = \frac{1}{t_{01}} \begin{pmatrix} 1 & r_{01} \\ r_{01} & 1 \end{pmatrix}, \quad (3.3.3)$$

wherein  $r_{01}$  and  $t_{01}$  are the reflection and transmission Fresnel coefficients [BW03] in the border between layers  $0$  and  $1$ , respectively. For  $p$  and  $s$  polarizations,  $r_{01}$  and  $t_{01}$  are determined by:

$$r_{01}(p) = \frac{n_1 \cos \theta_0 - n_0 \cos \theta_1}{n_1 \cos \theta_0 + n_0 \cos \theta_1}, \quad (3.3.4)$$

$$t_{01}(p) = \frac{2n_0 \cos \theta_0}{n_1 \cos \theta_0 + n_0 \cos \theta_1}, \quad (3.3.5)$$

$$r_{01}(s) = \frac{n_0 \cos \theta_0 - n_1 \cos \theta_1}{n_0 \cos \theta_0 + n_1 \cos \theta_1}, \quad (3.3.6)$$

$$t_{01}(s) = \frac{2n_0 \cos \theta_0}{n_0 \cos \theta_0 + n_1 \cos \theta_1}, \quad (3.3.7)$$

where  $n_0$  and  $n_1$  are the refractive indexes of the layer  $0$  and  $1$  and  $\theta_0$  and  $\theta_1$  are the angles of incidence and refraction, respectively.

Similarly, considering layers  $1$  and  $2$ ,  $S_{12}$  is defined as:

$$S_{12} = \frac{1}{t_{12}} \begin{pmatrix} 1 & r_{12} \\ r_{12} & 1 \end{pmatrix}. \quad (3.3.8)$$

On the other hand,  $P_1$  is given by:

$$P_1 = \begin{pmatrix} e^{i\beta_1} & 0 \\ 0 & e^{-i\beta_1} \end{pmatrix}. \quad (3.3.9)$$

$\beta_1$  represents the phase change of the plane wave along the interface  $1$  described by  $\beta_1 = kl \cos \theta_1 = \frac{2\pi}{\lambda} n_1 l \cos \theta_1$ , where  $\lambda$  is the light wavelength,  $l$  is the layer thickness,  $\theta_1$  is the propagation angle of the wave inside the layer, and  $n_1$  is the refractive index of the layer which, as mentioned before, is assumed to be real (no imaginary part  $\implies$  no absorption). Thereby,  $\beta_1$  is real and  $|e^{i\beta_1}| = 1$ .

In the end, once  $S_{01}$ ,  $P_1$  and  $S_{12}$  are known, by replacing Eqs. (3.3.3), (3.3.8) and (3.3.9) into (3.3.2),  $M_{0,2}$  becomes:

$$M_{0,2} = S_{01} \cdot P_1 \cdot S_{12} = \frac{1}{t_{01}t_{12}} \begin{pmatrix} e^{i\beta_1} + r_{01}r_{12}e^{-i\beta_1} & r_{01}e^{-i\beta_1} + r_{12}e^{i\beta_1} \\ r_{01}e^{i\beta_1} + r_{12}e^{-i\beta_1} & e^{-i\beta_1} + r_{01}r_{12}e^{i\beta_1} \end{pmatrix}. \quad (3.3.10)$$

By extending the previous analysis of the three-layer system to the entire scheme of Fig. 3.4, the transfer matrix  $M$  of the whole multilayer structure is given by:

$$M = S_{01} \cdot P_1 \cdot S_{12} \cdot P_2 \cdot S_{23} \cdot P_3 \cdot S_{34} \cdot P_4 \cdot S_{45} \cdot P_5 \cdots S_{(N-2)(N-1)} \cdot P_{N-1} \cdot S_{(N-1)(N)}. \quad (3.3.11)$$

Eventually, after knowing  $M$ , by solving  $E_i^{(0)}$  and  $E_r^{(0)}$  in terms of  $E_t^{(N)}$  in Eq. (3.3.1), the calculation of the amplitude reflection coefficient  $r_I$  and the amplitude transmission coefficient  $t_I$  leads to the final expressions of the reflectance intensity  $R_I$  and transmittance intensity  $T_I$  of the multilayer structure of  $N$  layers as follows:

$$\begin{aligned} \frac{E_r^{(0)}}{E_i^{(0)}} &= \frac{M_{21}}{M_{11}} = r_I \\ \implies R_I &= |r_I|^2. \end{aligned} \quad (3.3.12)$$

$$\begin{aligned} \frac{E_t^{(N)}}{E_i^{(0)}} &= \frac{1}{M_{11}} = t_I \\ \implies T_I &= |t_I|^2. \end{aligned} \quad (3.3.13)$$

### 3.3.1 Simulated response of the ICM

High transparency and low absorption at 100 GHz are key parameters of the input coupler mirror wafers for a good cavity performance. In this context, some solid materials like semiconductors, polymers and dielectrics provide high transmittance and transparency in the THz regime (0.1 – 3 THz). Within the first two families, high-resistivity crystalline silicon (Si) is the most transparent and least dispersive medium thanks to its practically constant refractive index  $n$  along the THz range ( $3.4174 < n < 3.4176$ ) and very low absorption coefficient  $\alpha$  in the first part of the THz spectrum ( $\alpha < 0.005 \text{ cm}^{-1}$  for  $\nu < 500$  GHz). In the case of dielectric materials, fused silica ( $\text{SiO}_2$ ) provides the lowest refractive index below 250 GHz ( $n \approx 1.950$ ) and a very low absorption coefficient ( $\alpha < 0.05 \text{ cm}^{-1}$ ) [Lee09, NM05, NM07]. This dielectric also offers the advantage of being transparent in the visible wavelength range which will be very useful for the alignment procedure of the cavity.

Considering  $l = 1 \text{ mm}$ ,  $\lambda = 3 \text{ mm}$  and  $\theta_0 = 15^\circ$  (whose value corresponds to the folding angle of the mirrors in the designed cavity), Fig. 3.6 illustrates the simulated

response of the ICM under a different number of layers with wafers made of Si and SiO<sub>2</sub>, respectively, by employing the previously presented multilayer structure. According to the graphs, the dependence of  $T_I$  and  $R_I$  on the number of wafers is clear, i.e, the greater the number of wafers in the ICM, the lower the transmittance and the higher the reflectance, either for a  $p$  or  $s$ -polarized incident light.

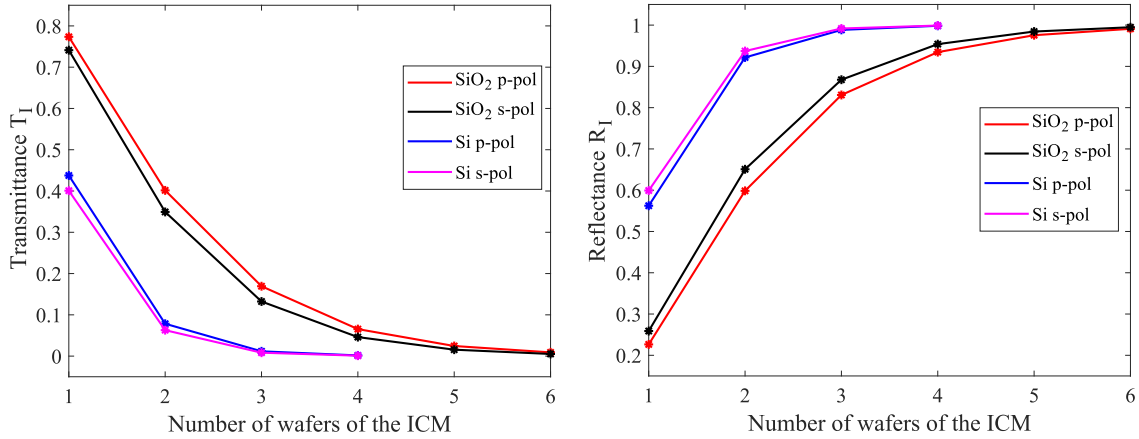


**Figure 3.6:** Simulated response of the ICM with a different number of wafers made of Si and SiO<sub>2</sub>, respectively.

It should be pointed out that the typical Bragg reflector considers a quarter wavelength for the layer thickness. However, under this consideration, for Si is about 200  $\mu\text{m}$  and for SiO<sub>2</sub> is about 400  $\mu\text{m}$  which are difficult to deal with considering that in the experiment the wafers are 101.6 mm in diameter. This is the reason why 1 mm in the wafer and air gap thickness was chosen.

### 3.4 Experimental results

Before presenting the experimental results about the bow-tie enhancement cavity, the equipment and devices used for this purpose and the rest of the experimental parts throughout the thesis are mentioned below:

- IMPATT-100-H/F diode source. Frequency emission: 100 GHz (CW). Beam emission: Gaussian distribution (for a characterization of the Gaussian emission and general features of the source see A).
- THz camera model Tera-1024. Frequency range detection: 40 GHz 0,7 THZ.

- Zero-Bias detector model WR10ZBD-F06. Frequency range detection: 75 – 110 GHz. Maximum response:  $\sim 15$  GHz.
- Oscilloscope LeCroy model 640Zi. Bandwidth: 4 GHz. Acquisition: 40 Gs/s.

### 3.4.1 Mode matching

Fig. 3.2 shows the beam propagation of the desired fundamental Gaussian mode of the bow-tie cavity. To replicate this propagation pattern, the q-parameter of the input Gaussian beam emitted by the 100 GHz source must match the characteristics of the q-parameter of the Gaussian beam inside the cavity. This guarantees that after one round trip the light field reproduces itself in the resonator.

As a mode matching strategy, it will generate an input beam whose waist has the same value and position as the beam waist  $w_{0M}$  between the ICM and FM, already computed in Eq. (3.2.7). It is important to mention that  $w_{0M}$  does not consider the astigmatism issue and its value is roughly the average between the sagittal and tangential beam waist of Fig. 3.3b).

The desired position and value of  $w_{0M}$  can be achieved by a single-lens system [WJ19][FLE71] whose scheme is shown in Fig. 3.7.

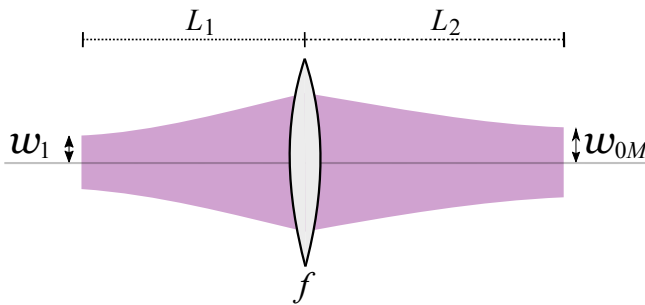


**Figure 3.7:** Single-lens system approach. A Gaussian beam with waist  $w_1 = 10.2$  mm propagates a distance  $L_1$  towards a lens with focal length  $f$  to then propagate along an additional distance  $L_2$  forming a new beam waist  $w_{0M} = 18.12$  mm.

Knowing that  $w_1 = 10.2$  mm, the confocal parameter before and after the lens is  $z_{R1} = 2\pi w_1^2/\lambda = 217.90$  mm and  $z_{R2} = 2\pi w_{0M}^2/\lambda = 674.07$  mm, respectively. Furthermore,  $L_1$  and  $L_2$  have a consistent value only if  $f \geq \sqrt{z_{R1} \cdot z_{R2}/4} = 191.62$  mm. After applying the ABCD matrix principle on the system and considering  $f = 200$  mm, the distance from the waist  $w_1$  to the lens and the distance from the lens to the second waist  $w_{0M}$  are given by:

$$L_1 = f + \frac{w_1}{w_{0M}} \sqrt{f^2 - \frac{z_{R1} \cdot z_{R2}}{4}} = 232.6 \text{ mm.} \quad (3.4.1)$$

$$L_2 = f + \frac{w_{0M}}{w_1} \sqrt{f^2 - \frac{z_{R1} \cdot z_{R2}}{4}} = 300.7 \text{ mm.} \quad (3.4.2)$$

With the previous calculations, the mode matching setup is shown in Fig. 3.8. The waist  $w_1 = 10.2 \text{ mm}$  is obtained by using a lens with focal length  $f_1 = 63 \text{ mm}$  situated at  $80 \text{ mm}$  from the source. The steering metal mirror  $M_1$  together with the lens  $f$  are used for aligning the beam towards the cavity.

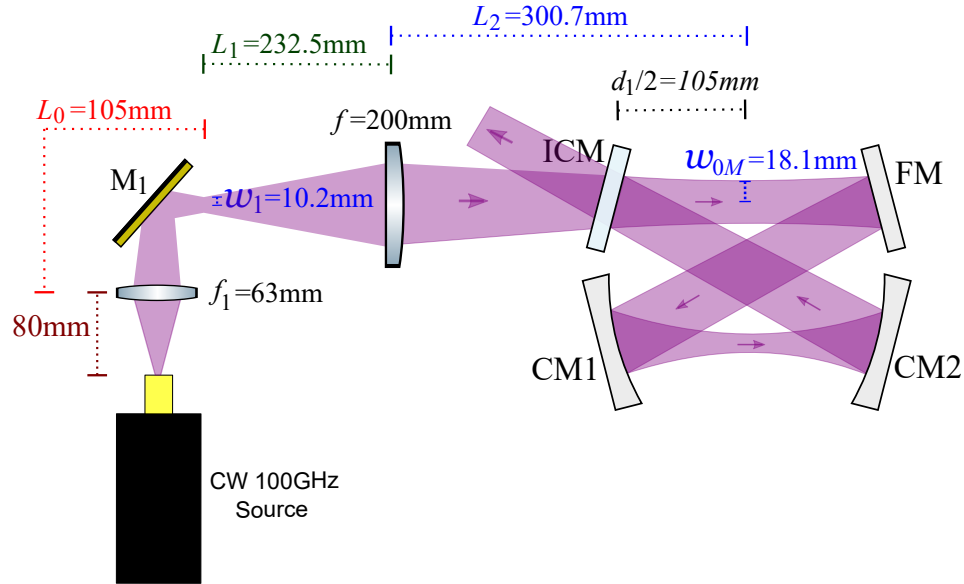


**Figure 3.8:** Mode matching setup.

Eventually, Fig. 3.9 illustrates the beam profile measured at  $w_1$  and  $w_{0M}$ , respectively. The similarity between the calculated  $w_{0M}$  of Fig. 3.8 and the measured  $w_{0M}$  of Fig. 3.9 demonstrates the effectiveness of the mode matching strategy employed. It is important to mention that the beam profiles were measured by using a scanning procedure similar to that described in appendix A.

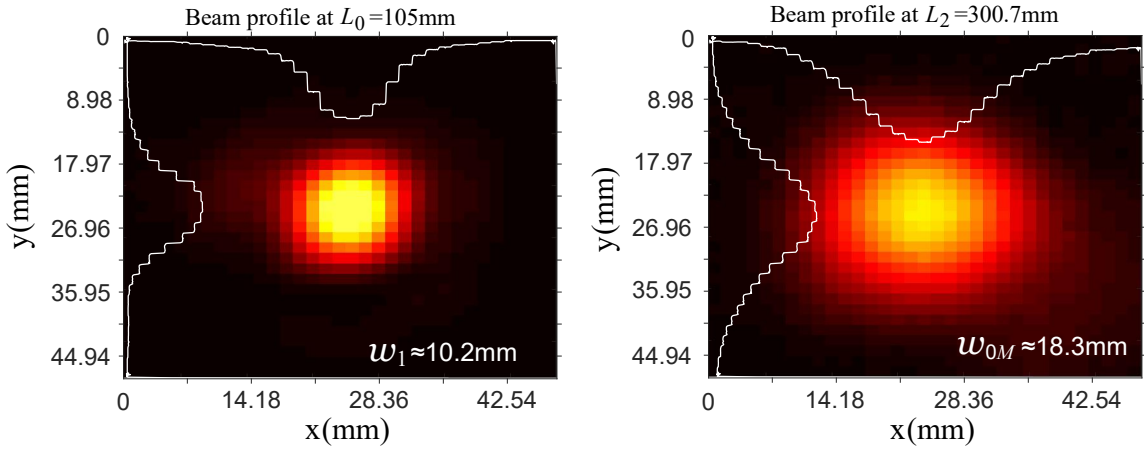


**Figure 3.9:** Beam profile measured at  $L_0 = 105$  mm at waist  $w_1$ , and at  $L_2 = 300.7$  mm at waist  $w_{0M}$  of Fig. 3.8. The calculated  $w_{0M}$  is similar to the measured one.

### 3.4.2 Bow-tie enhancement cavity setup

As presented in the previous subsection, the mode matching setup, by itself, is enough to have the cavity approximately at resonance with the input radiation. However, the cavity mounting and alignment process can be quite difficult using only the 100 GHz radiation.

To minimize this hardship, a complementary optical system by implementing a HeNe alignment laser ( $\lambda = 633$  nm) is added to the scheme. The complete Bow-tie enhancement cavity setup is shown in Fig. 3.10. On the one hand, the semiconductor wafer  $SW_1$ , which is highly transparent for 100 GHz and reflective for 633 nm of wavelength, reflects the alignment beam towards the cavity. Therefore, the alignment beam propagates superposed and collinearly with the THz signal. Furthermore, the alignment laser is also sent perpendicular to the input beam onto the center of every cavity mirror to achieve the cavity dimensions more accurately. On the other hand, the flat mirror FM is mounted on a motorized stage MS. This mounting enables to obtain the circulating spectrum pattern by scanning the cavity length throughout the different resonant frequencies. Finally, the semiconductor wafer SW between the cavity concave mirrors reflects a small percentage of the incident beam which is used for identifying and monitoring the circulating light inside the resonator.

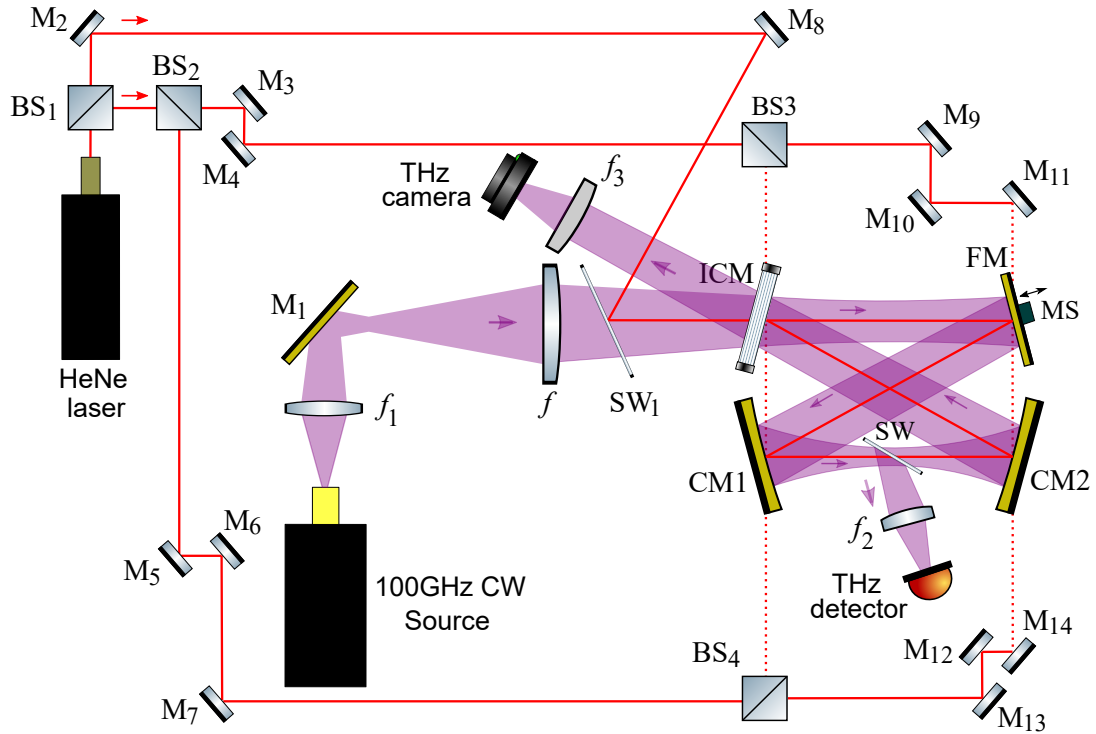


**Figure 3.10:** Bow-tie enhancement cavity setup. A Gaussian beam generated by a 100 GHz CW source is adapted through a mirror and lens system to match the lowest mode of the cavity. The HeNe laser is used as a guide to align the THz beam into the cavity.

The ability of the cavity to accumulate energy is directly related to its losses. For this purpose, metal-coated mirrors offer a high reflectance in practically the entire THz range [ND11] with low losses. For the case of the designed cavity, FM, CM1 and CM2 are metal mirrors with similar characteristics manufactured by the company Tydex. They are made of BK7 material with a gold coating which allows them to achieve a reflectance of  $R_C = 0.99 \pm 0.003$  at 100 GHz. Each of these mirrors is 101.6 mm in diameter and, particularly for CM1 and CM2, their radius of curvature is  $R_{CM} = 186$  mm.

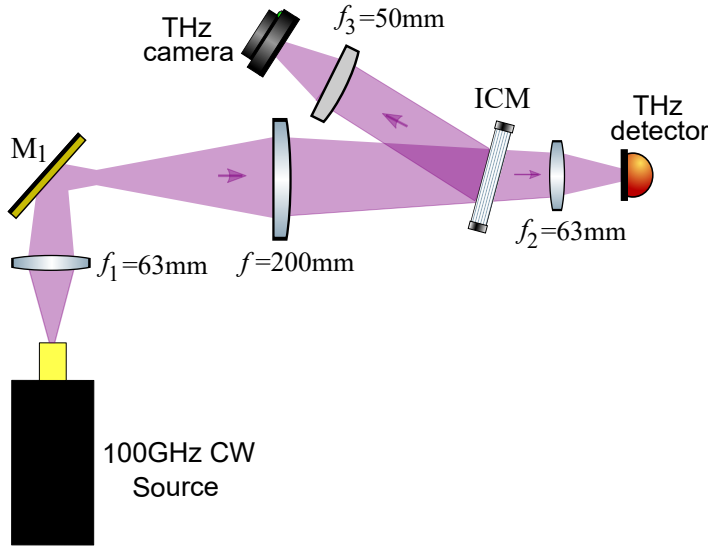
The properties of the ICM and the SW may vary depending on the way they are implemented in the application, therefore both are described separately in more detail. All the wafers used in this work were manufactured by Siegert Wafer GmbH and their dimensions are 101.6 mm in diameter, 1 mm in thickness.

### ICM transmittance

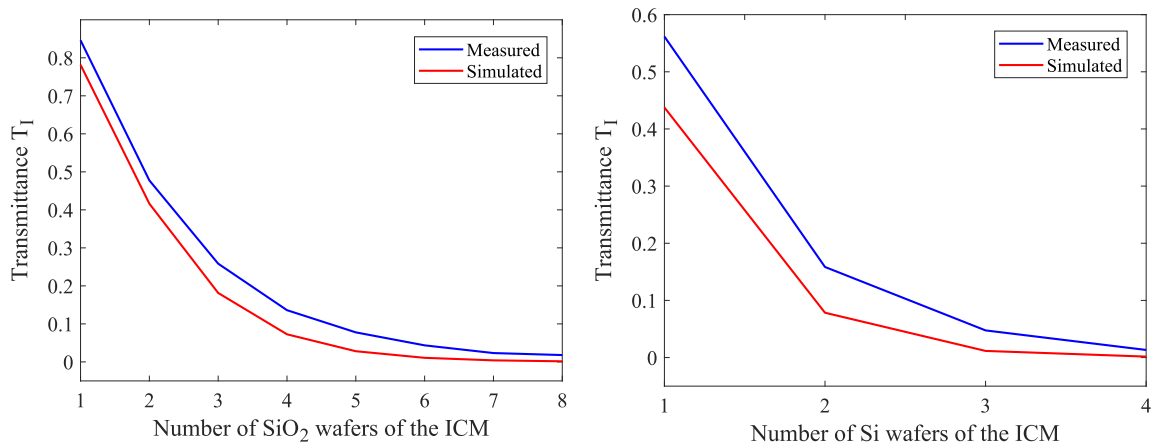
In the design of the ICM proposed in section 3.3, the angle  $\theta_0$  of the incidence wave as well as the number and types of wafers are preponderant in its performance. Thus,



by developing the experimental setup of Fig. 3.11, Fig. 3.12 shows the measured transmittance  $T_I$  of the ICM using two types of wafer materials: UV-grade  $\text{SiO}_2$  and intrinsic high resistivity Si. The data was taken with the ICM placed at around  $\theta_0 = 15^\circ$  and for a p-polarized incident light of 3 mm wavelength. To contrast, the simulated values of Fig. 3.6 were also incorporated in the figure.



**Figure 3.11:** Setup to measure the ICM transmittance.  $T_I$  is the ratio between the measured power with and without the ICM.



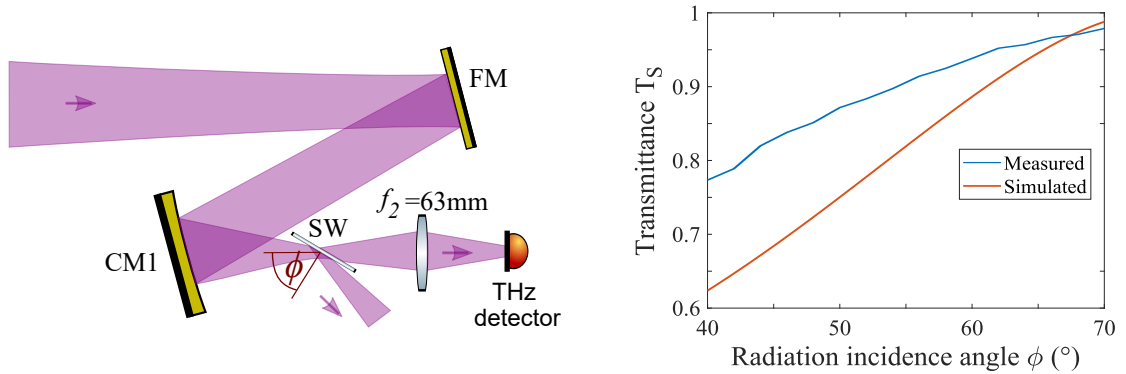
**Figure 3.12:** Simulated and measured  $T_I$ . ICM formed by  $\text{SiO}_2$  wafers (left). ICM formed by Si wafers (right).

Fig. 3.12 depicts that the experimental curves are larger in magnitude than their theoretical counterparts, however both decay in a similar way regardless of the type of wafer used. It is concluded that the presented design of the ICM enables the control of the intensity of the light entering the cavity by managing the number of wafers in the ICM.

### SW transmittance

Without considering the ICM, ideally, to monitor the circulating light in a bow-tie cavity, the weak signal transmitted by one of the mirrors is used (usually called *output coupler mirror*). In the case of the resonator designed in this thesis, it is not possible to obtain any measurable signal transmitted by any the mirrors due to their metal-coated nature. Nevertheless, positioning the SW at a certain angle between the concave mirrors enables the measurement of a faint reflected light which is enough to comply with the monitoring role.

The SW used is made of high-resistivity intrinsic silicon. Its characterization was performed by following the experimental setup depicted on the left of Fig. 3.13. Here, its transmittance  $T_S$  was measured under different angles  $\phi$  regarding the incident 100 GHz radiation. The simulated and experimental results of  $T_S$  are shown on the right of Fig. 3.13. It can be observed that, as expected,  $T_S$  increases as  $\phi$  grows. Theoretically,  $T_S = 1$  when  $\phi = 73.7^\circ$  which corresponds to Brewster's angle [BW03, YF09]. However, experimentally, the maximum angle achieved without distorting the beam – and consequently the measurement – with the border of the SW was  $\phi = 70^\circ$ .



**Figure 3.13:** Transmittance of the SW for an incident 100 GHz radiation. On the left, the experimental setup.  $T_S$  is the ratio between the measured power with and without the SW. On the right,  $T_S$  regarding the angle  $\phi$ .

### 3.4.3 Impedance matching and enhancement factor

The impedance coupling conditions given in Eqs. (2.5.25), (2.5.26) and (2.5.27) are also valid for the ring resonator. However, due to the increase in the number of mirrors (which implies more losses) and the fact that the light circulates in only one direction, some of the remaining cavity equations experience changes [Nag10] compared to the

two-mirror case. Excluding the ICM again, the sum of all the other round-trip cavity losses ( $L$ ) is determined by the reflectance of FM, CM1 and CM2 and the transmittance of SW as follows:  $L = 1 - R_C^3 T_S$ , wherein any losses due to dispersion or absorption are also contemplated. Therefore, at resonance, the reflected and circulating light intensity become now:

$$I_r = \frac{I_0(r_I - r_C^3 t_S)^2}{(1 - r_I r_C^3 t_S)^2}. \quad (3.4.3)$$

$$I_c = \frac{I_0 t_I^2}{(1 - r_I r_C^3 t_S)^2}. \quad (3.4.4)$$

Base Eq. (3.4.4), the enhancement factor for the ring cavity is given by:

$$\mathcal{E} = \frac{I_c}{I_0} = \frac{t_I^2}{(1 - r_I r_C^3 t_S)^2}. \quad (3.4.5)$$

Likewise, under the impedance matching case ( $T_I = L$ ) the enhancement factor is determined by (similar to Eq. (2.5.31)):

$$\mathcal{E} = \frac{I_c}{I_0} = \frac{1}{T_I} = \frac{\mathcal{F}}{\pi}, \quad (3.4.6)$$

wherein the finesse is now defined as:

$$\mathcal{F} = \frac{\pi \sqrt{r_I r_C^3 t_S}}{1 - r_I r_C^3 t_S} = \frac{FSR}{FWHM}, \quad (3.4.7)$$

and the cavity linewidth as:

$$FWHM = \frac{2(1 - r_I r_C^3 t_S)}{\sqrt{r_I r_C^3 t_S}}. \quad (3.4.8)$$

In the same way, the cavity decay time  $t_c$  and the  $Q$  factor are now calculated by Eqs. (3.4.9) and (3.4.10), respectively.

$$t_c = \frac{d}{cL_T} = \frac{d}{c(1 - r_I^2 r_C^6 t_S^2)} = \frac{\mathcal{F}}{\pi \cdot FSR}. \quad (3.4.9)$$

$$Q = \frac{d\mathcal{F}}{\lambda}. \quad (3.4.10)$$

where  $d = 2(d_1 + d_2)$  is the cavity length.

### Simulated enhancement factor

$R_C = 0.99 \pm 0.003$  is the reflectance of the metal mirrors and cannot be manipulated. Hence,  $\mathcal{E}$  in Eq. (3.4.5) varies according to the transmittance  $T_I$  and the reflectance  $R_I = 1 - T_I$  of the ICM as well as the transmittance  $T_S$  of the SW, which depends on the angle  $\phi$  (see Fig. 3.13). In particular, for  $\phi = 68^\circ$ , which is the biggest angle achievable with the cavity closed,  $T_S \approx 0.97$ . By using these values and considering a perfect mode matching and alignment, a simulation of the enhancement factor in terms of  $T_I$  can be seen in Fig. 3.14. As the curve indicates, a maximum of  $\mathcal{E} \approx 20$  can be obtained with the actual cavity parameters. This situation corresponds to the impedance matched case which occurs at  $T_I = L = 0.05$ . Thus, based on the conditions established by Eqs. (2.5.26) and (2.5.27), for  $T_I < 0.05$  the cavity is under coupled, and for  $T_I > 0.05$  is over coupled.

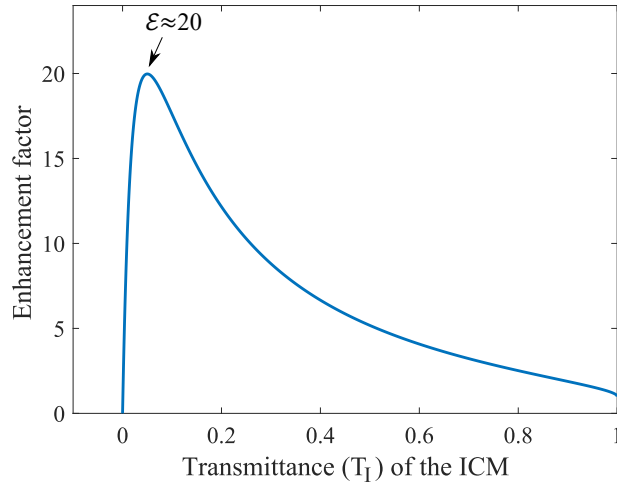


**Figure 3.14:** Simulated enhancement factor regarding  $T_I$  considering the actual cavity parameters.

From the experimental graphs of Fig. 3.12, the ICM formed by three Si wafers has a  $T_I = 0.0475$ . The transmittance of this ICM case is the nearest to  $L = 0.05$  (point of maximum  $\mathcal{E}$ ), so it will be considered in the following subsection.

### Circulating spectrum

After mounting the entire bow-tie enhancement cavity setup of Fig. 3.10, the process of scanning the resonator length by moving the FM reveals the spectrum of the circulating light inside the cavity, whose pattern is monitored by measuring the weak signal reflected by the SW. For the case of the ICM formed by three silicon wafers and with the SW placed at  $\phi = 68^\circ$ , the results of the scanning procedure are depicted in Fig. 3.15. Basically, in the graph, each of the three large resonance peaks corresponds to the fundamental Gaussian mode  $TEM_{00}$  of the cavity which occurs every  $2\pi$ , just when the cavity length has increased one light wavelength ( $\lambda=3\text{ mm}$ ). The small resonance peaks located next to the big ones are high-order transverse modes  $TEM_{mn}$  of the cavity which appear when the cavity input light also matches these modes and/or the cavity is slightly misaligned. Nevertheless, the sharpness of  $TEM_{00}$  and the low amplitude of  $TEM_{mn}$  demonstrate that at resonance most of the input light is coupled into the cavity matching the cavity fundamental mode.

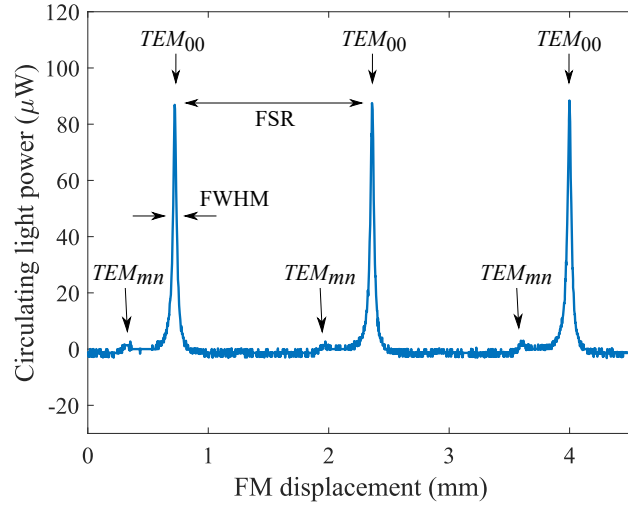


**Figure 3.15:** Experimental spectrum pattern of the cavity circulating light. Case of the ICM formed by three Si wafers and  $\phi = 68^\circ$ .

According to the spectrum in Fig. 3.15,  $\text{FWHM} \approx 0.0321\text{ mm}$  and  $\text{FSR} \approx 1.6398\text{ mm}$ , which in the frequency domain are equivalent to  $6.525\text{ MHz}$  and  $333.330\text{ MHz}$ . By using these values into Eqs. (3.4.7), (3.4.9) and (3.4.10) the rest of cavity parameters can be estimated. A summary of them is depicted in Table 3.2. Particularly, in the calculated value column the impedance matched condition was

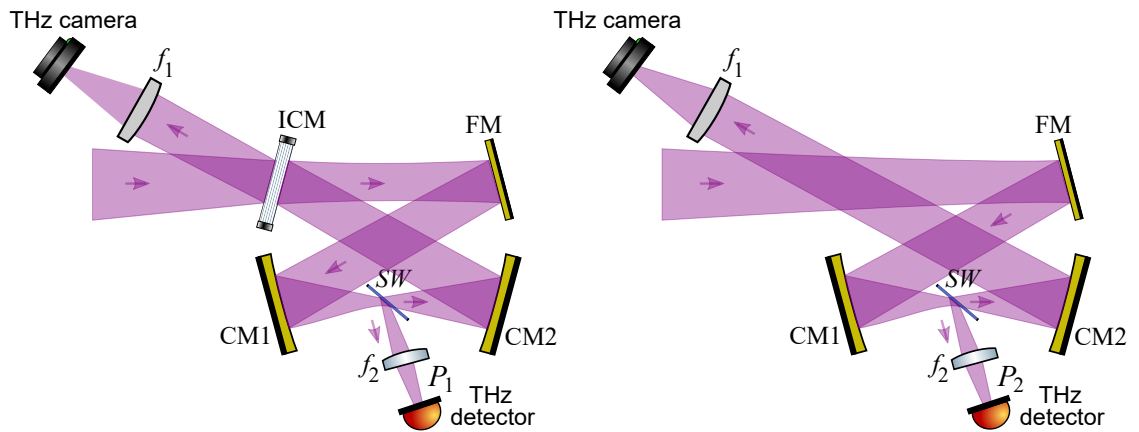
considered (Eq. (3.4.6)).

**Table 3.2:** Cavity parameters. Case of the ICM with three Si wafers.

Parameter	Experimental value	Calculated value
Finesse ( $\mathcal{F}$ )	51.085	62.675
Decay time ( $t_c$ )	48.783 ns	59.851 ns
Q factor	15,326	18,803

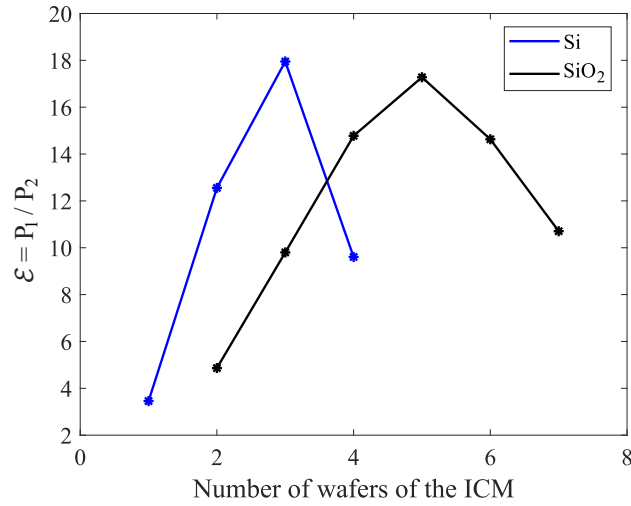
### Experimental enhancement factor

Fig. 3.16 shows an experimental way [Nag10] to measure  $\mathcal{E}$ , which consists of two different power measurements –  $P_1$  and  $P_2$  – obtained from the reflected light by the SW. Specifically,  $P_1$  is proportional to the cavity circulating light power, which is measured with the cavity aligned and tuned at resonance (Fig. 3.16 left), this means that the cavity is situated on any of the large peaks in Fig. 3.15. Following this, when the cavity is still tuned to the foregoing condition,  $P_2$  is proportional to the cavity input light power measured after removing the ICM (Fig. 3.16 right). Finally,  $\mathcal{E}$  is merely the ratio  $P_1/P_2$ .



**Figure 3.16:** Experimental setup for measuring the cavity enhancement factor. Cavity closed at resonance (left). Cavity opened with ICM removed (right). The enhancement factor is equal to  $\mathcal{E} = P_1/P_2$ .

Some results of the enhancement factor experiment can be seen in Fig. 3.17. The outcomes are for different numbers and kinds of wafers in the ICM. Analyzing both curves in terms of the impedance coupling conditions, the cavity is: under-coupled in the zone of the negative slope; over-coupled in the positive slope part; and impedance matched at around the peak value. For the SiO<sub>2</sub> case,  $\mathcal{E}$  increases until a bit over 17 by using five wafers. Instead, by employing three Si wafers, a maximum enhancement factor of  $\mathcal{E} \approx 18$  is achieved, corresponding to the best result regarding the ideal case of impedance matching of  $\mathcal{E} \approx 20$ . For this case, the cavity parameters were already described in Fig. 3.15 and Table 3.2 of the previous subsection. Furthermore, according to Fig. 3.12,  $T_I = 0.0475$  which is less than  $L = 0.05$ . Therefore, the cavity is a little under-coupled at the maximum case.



**Figure 3.17:** Experimental results of the enhancement factor in terms of the number and type of wafers in the ICM.

Eventually, Table 3.3 shows a summary including the enhancement factor obtained under the different scenarios. The columns with the measured  $\mathcal{E}$  correspond to the values of Fig. 3.17. On the other hand, assuming a perfect mode matching with no beam misalignment in the cavity and employing the measured  $T_I$  of the different ICMs of Fig. 3.12, the columns with the maximum  $\mathcal{E}$  were calculated using Eq. (3.4.5).

**Table 3.3:** Measured and maximum  $\mathcal{E}$  of the cavity under different ICMs

Number of wafers in the ICM	Measured $\mathcal{E}$ (with Si wafers)	Maximum $\mathcal{E}$ (with Si wafers)	Measured $\mathcal{E}$ (with SiO <sub>2</sub> wafers)	Maximum $\mathcal{E}$ (with SiO <sub>2</sub> wafers)
1	3.455	4.46	-	-
2	12.55	14.12	4.865	5.47
3	17.95	19.95	9.801	10.01
4	9.606	13.10	14.78	15.37
5	-	-	17.18	18.98
6	-	-	14.63	19.87
7	-	-	10.71	17.21

The difference between the measured  $\mathcal{E}$  and maximum  $\mathcal{E}$  in Table 3.3 is due to three factors: a non-perfect mode matching, misalignment of the beam inside the cavity, and a small percentage of absorption losses  $A_I$  present in the ICM. Strictly speaking about the last factor, the input coupler mirror satisfies the equality  $T_I + R_I + A_I = 1$ . In the maximum  $\mathcal{E}$  case,  $A_I = 0$ . On the contrary, for the measured  $\mathcal{E}$  case,  $A_I \neq 0$ . For instance, in the case of the ICM with three silicon wafers and assuming a perfect mode matching with no beam misalignment, the measured transmittance is  $T_I = 0.0475$  and the measured enhancement factor is  $\mathcal{E} = 17.95$ . By replacing these values into Eq. (3.4.5) and solving for  $r_I$ , it is found that  $R_I = r_I^2 = 0.9472$ . This implies an absorption loss in the ICM of  $A_I = 1 - (T_I + R_I) = 0.0053$ .



---

# Chapter 4

## Semiconductor as an optical switch

### 4.1 Introduction

A semiconductor is a solid-state material that can operate as an insulator or conductor of charged particles depending on the environmental conditions (perturbations) in which it is immersed, such as temperature, the presence of external electromagnetic fields, and possible light illuminating on it, among others. Silicon (Si) and germanium (Ge) are elemental semiconductors being Si the most important and widely used in the construction of integrated circuits (ICs) and electronic components. Moreover, more than twenty compound semiconductors can be found – such as gallium arsenide (GaAs) – and more than ten alloy semiconductors [Pie96].

When a laser light with sufficient photon energy illuminates the surface of a semiconductor, a photogeneration process occurs leading to a state of high carrier concentration in the material. As a result, a temporary reflectance (optical switch on) is induced in the semiconductor for THz frequencies. Otherwise, without the excitation laser, the semiconductor is transparent (optical switch off) to the THz radiation.

This chapter provides, firstly, a theoretical background of the general nature of semiconductors in equilibrium and non-equilibrium conditions. Secondly, it inspects some qualitative properties of the photogeneration and recombination phenomena. Thirdly, it presents a quasi-classical analysis of the optical switch principle along with some simulations, and finally, it shows experimental results of Si and GaAs wafers acting as an optical switch of an incident 100 GHz wave under a 532 nm excitation laser pulse.

## 4.2 Energy bands in semiconductors

Atoms within a crystalline semiconductor are ordered and organized spatially in a three-dimensional periodic arrangement or lattice. In principal semiconductors, each atom is bound to its closest four atoms through covalent bonds among their respective four outermost orbital energy level electrons called *valence electrons* [Pie96].

In most optical and electronics processes, the bound electrons in the lattice are located at specific energy states inside two well-defined energy bands: the *valence band* (lower energy states) and the *conduction band* (higher energy states). The energy distance between them is called *band gap* which is essentially the minimum energy required to move an electron between the two bands. At temperature  $T=0$  K and under equilibrium conditions – this means, in thermal equilibrium without the presence of external electromagnetic waves or other perturbations interacting with the semiconductor – the electron distribution is completely concentrated in the valence band, whereas the conduction band is totally empty [Pie96]. The general energy band diagram can be seen in Fig. 4.1.

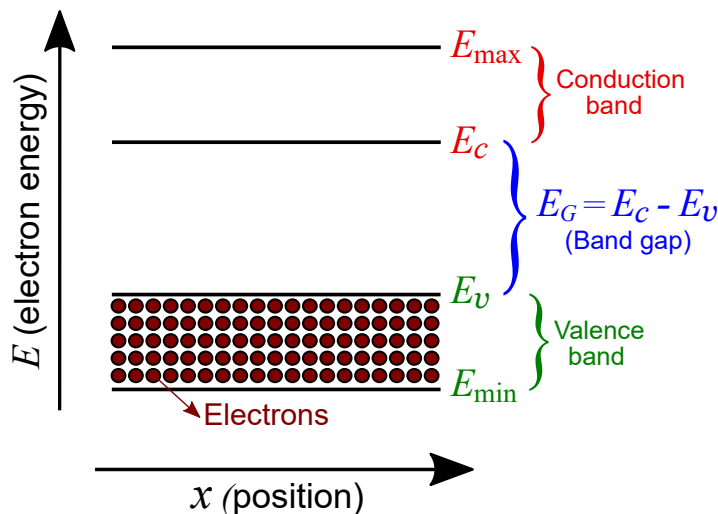


**Figure 4.1:** General model of the semiconductor energy band diagram at  $T=0$  K.  $E_v$  is the highest energy level of the valence band,  $E_c$  is the lowest energy level of the conduction band, and  $E_G = E_c - E_v$  is the band gap energy.

At temperature  $T>0$  K and under equilibrium conditions, a restricted number of electrons, in the valence band, gain enough thermal energy to break their covalent bonds, jump into the conduction band and then move freely along the lattice. The missing bond in the valence band left by each of these now “free” electrons is known as a *hole*. Electrons in the conduction band and holes in the valence band are called *carriers* and they have an associated electric charge of similar magnitude but different polarity (electrons are negatively charged and holes positively charged) [Pie96, Nea11].

This process of electron-hole pair generation by thermally breaking bonds is schematized in Fig. 4.2.

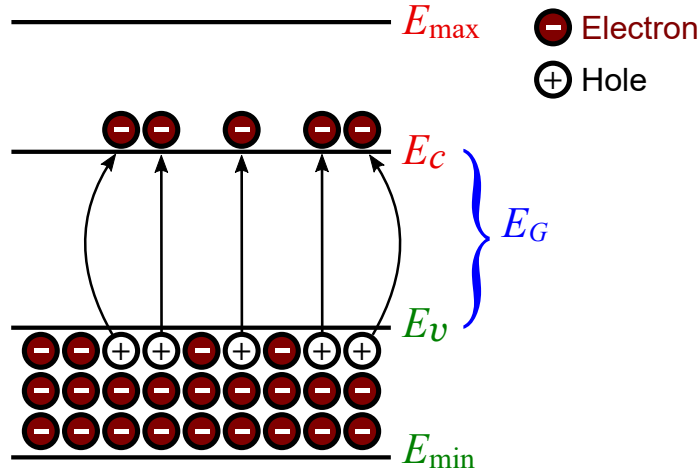


**Figure 4.2:** Semiconductor energy band diagram with the band-to-band thermal generation of electron-hole pairs at  $T > 0$  K.

The number of electrons in the conduction band and holes in the valence band per unit volume, denoted as  $n$  and  $p$  respectively, depends on the nature of the semiconductor. In an intrinsic semiconductor or also called undoped semiconductor (highly pure semiconductor with a negligible number of impurity atoms)  $n = p$ , hence they are simply denoted as  $n_i$ . On the contrary, in an extrinsic semiconductor or also called doped semiconductor (semiconductor with a controlled number of known impurity atoms)  $n \neq p$ . In this case, the difference between  $n$  and  $p$  is associated with the quantity and properties of the doping material. For example, in the doping process of silicon, dopants like phosphorus or arsenic donate an electron to the conduction band, thus increasing the total electron concentration ( $n > p \Rightarrow n$ -type semiconductor) and dopants like boron or indium accept an electron from the valence band, resulting instead in an increase of the total hole concentration ( $n < p \Rightarrow p$ -type semiconductor) [Nea11].

The motion of carriers in a semiconductor involves multiple internal forces and fields due to collisions with the atoms of the lattice. It is a complex process adequately described by quantum mechanics. However, a classical perspective of the semiconductor behavior can be performed under the approach of the effective carrier mass concept. Mainly, in this formalism, the mass of the carrier and the effects of the complicated internal forces are grouped into the effective mass term, denoted as  $m^*$ . This approach is widely used in the literature (see e.g. [Pie96, Nea11, Pie03]) to determine the different variables and properties of the semiconductor, such as the density of states in the energy bands, the Fermi levels, the carrier concentration in doped and intrinsic semiconductors and so on. Throughout the rest of the chapter, the following general

theoretical framework about the semiconductor state under non-equilibrium conditions is described by using the effective mass formalism.

## 4.3 Carrier current

In equilibrium conditions, the net current in a semiconductor is zero. Nevertheless, external perturbations and a carrier concentration gradient move the semiconductor out of the equilibrium state causing the motion of the carriers. In the end, both situations induce a current flow proportional to the magnitude of the perturbation and to the carrier concentration.

### 4.3.1 Drift current

When a constant electric field  $E$  is applied to the semiconductor, the carriers develop an accelerated motion that leads to the so-called *drift current* [Pie96, Nea11]. However, holes and electrons undergo a mobility loss through collisions with the thermal vibrations of the lattice atoms, a process known as *lattice scattering*. Then, the average drift velocity  $v_d$  experienced by carriers is defined as:

$$v_d = \mu_q E, \quad (4.3.1)$$

wherein  $\mu_q$  is a temperature and doping dependence term named *mobility factor* which basically interprets the grade of movement of the charge under the external electric field. Mathematically, it is given by:

$$\mu_q = \frac{e\tau_q}{m_q^*}, \quad (4.3.2)$$

where  $\tau_q$  is the average time of the charge between collisions,  $e$  is the magnitude of the charge, and  $m_q^*$  is the effective mass of the carrier. Therefore, for a given volume charge density  $\rho$ , the drift current density is determined by:

$$\begin{aligned} J_d &= \rho v_d \\ &= \rho \mu_q E. \end{aligned} \quad (4.3.3)$$

Electrons ( $n$ ) and holes ( $p$ ) have their own mobility factor:  $\mu_n$  and  $\mu_p$ , respectively. Furthermore, knowing that  $\rho$  is defined as the magnitude of the charge times the number of charges and that in intrinsic semiconductors  $n = p = n_i$ , then  $J_d$  can be expressed by:

$$\begin{aligned} J_d &= (en\mu_n + ep\mu_p)E \\ &= e(\mu_n + \mu_p)n_iE \\ &= \sigma E, \end{aligned} \tag{4.3.4}$$

where  $\sigma = e(\mu_n + \mu_p)n_i$  is the conductivity of the semiconductor. Eq. (4.3.4) intuitively concludes: the higher the  $n_i$ , the higher the  $\sigma$ ; and the proportionality between  $J_d$  and  $E$ . In parallel, a reduction in temperature implies a less thermal vibration of the lattice atoms which causes greater mobility of carriers due to a lower number of collisions. The latter also involves a larger conductivity which in the end results in a higher drift current density.

Moreover, the resistivity  $\rho$  of the semiconductor is defined as the inverse of  $\sigma$ :

$$\rho = \frac{1}{\sigma} = \frac{1}{e(\mu_n + \mu_p)n_i}, \tag{4.3.5}$$

wherein a high resistivity generates a greater resistance to current flow, leading to a lower  $J_d$ , as expected.

In the case of doped semiconductors, in addition to  $n \neq p$ , there is a second loss mechanism due to collisions between the carriers and the added impurity atoms called *ionized impurity scattering*. This process contributes to the value of the respective mobility carriers  $\mu_n$  and  $\mu_p$ , which affects  $\sigma$  and consequently  $J_d$ .

### 4.3.2 Diffusion current

In semiconductors, diffusion is the process by which carriers move from a high concentration zone to a lower concentration zone. The current flow generated by this motion is called *diffusion current* [Pie96, Nea11].

Analogous to the drift case, the diffusion current density is given by:

$$J_{diff} = J_{n-diff} + J_{p-diff}, \quad (4.3.6)$$

with  $J_{n-diff}$  as the diffusion current density due to electrons and  $J_{p-diff}$  as the diffusion current density due to holes. Both are defined by:

$$J_{n-diff} = eD_n \nabla n, \quad (4.3.7)$$

$$J_{p-diff} = -eD_p \nabla p, \quad (4.3.8)$$

where  $e$  is the magnitude of the charge,  $D_n$  is the electron diffusion coefficient,  $D_p$  is the hole diffusion coefficient,  $\nabla n$  is the three-dimensional density gradient of electrons and  $\nabla p$  is the three-dimensional density gradient of holes. According to Eqs. (4.3.7) and (4.3.8),  $J_{diff}$  is directly proportional to the carrier density gradient, this means, the larger the concentration gradient, the greater the diffusion current.

Eventually, by using Eqs. (4.3.4) and (4.3.6), the total current density in a semiconductor is given by:

$$\begin{aligned} J &= J_d + J_{diff} \\ &= en\mu_n E + ep\mu_p E + eD_n \nabla n - eD_p \nabla p. \end{aligned} \quad (4.3.9)$$

## 4.4 Carrier photogeneration and recombination

Fig. 4.2 indicates that thermal excitation is a way of electron-hole pair generation. Another mechanism of carrier generation can be accomplished by using light. If the surface of a semiconductor is illuminated by a monochromatic light with photon energy  $E_{ph} = \hbar\omega$ , larger than the band gap energy, the photon is absorbed causing an electron to transition from the valence band to the conduction band, thus generating an electron-hole pair. This process is called *photogeneration* [Pie96] and is directly related to the development of this thesis.

The carrier generation occurs all the time in the semiconductor at a certain rate  $G_g$  when it interacts with either of the two mechanisms. Once steady state is achieved,

the carrier concentration is stable and independent of time (constant generation rate). In order to maintain the concentration of carriers in such a state, through a parallel process, electrons in the conduction band must necessarily fall into the valence band at a rate  $R_r$  equal to  $G_g$ , releasing energy as a photon and/or heat during the process to then recombine with the empty states (holes). This process is called *recombination*. A representation of the generation and recombination processes is shown in Fig. 4.3. In both, the conservation laws of energy and momentum must be fulfilled [Nea11].

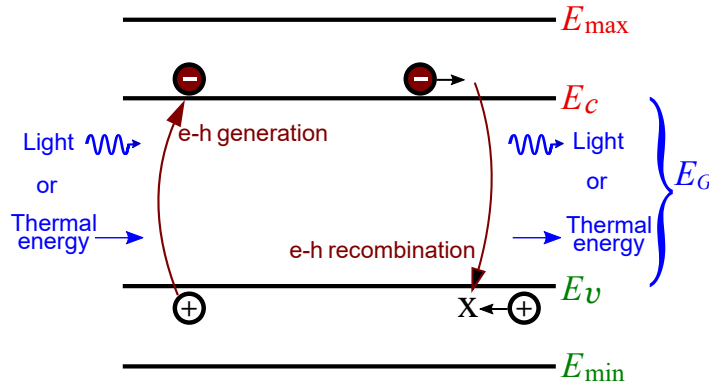


**Figure 4.3:** Representation of the electron-hole generation and recombination processes.

The way how an electron transitions between the two energy bands, either in the process of generation or in recombination, depends on the two band gap categories in which semiconductors are classified: direct band gap semiconductor or indirect band gap semiconductor. To explain their differences, according to quantum mechanics, the wave function defining an electron is assumed to have the form of a plane wave with wave vector  $k$ . Then, the allowed energy states of the electron are described in terms of  $k$  by the following parabolic equation [YC10, Ham17]:

$$E = \frac{\hbar^2 k^2}{2m_n^*} = \frac{p^2}{2m_n^*}, \quad (4.4.1)$$

where  $p = \hbar k$  is the momentum of the electron. By using Eq. (4.4.1), it is possible to create a different diagram of the energy bands of the electron in the semiconductor, this time  $E$  regarding the momentum through  $k$ , which is known as  $E - k$  diagram.

#### 4.4.1 Direct band gap semiconductors

On one hand, in the case of a direct band gap semiconductor [Gru16, Pie96, Nea11], the  $E - k$  diagram can be seen in Fig. 4.4. The picture illustrates that the energy minima

$E_c$  of the conduction band and the energy maxima  $E_v$  of the valence band are located at the same value of momentum  $k_0 = 0$ . In Fig. 4.4a), when the photogeneration takes place (also valid for thermal generation), the electron transitions directly from the valence band into the conduction band. The photon of energy  $\hbar\omega = E_G$  absorbed in the process fulfills the energy conservation ( $E_c = E_v + \hbar\omega$ ) as well as the momentum conservation ( $k_v = k_c = k_0$ ).

On the other hand, in the recombination process shown in Fig. 4.4b), the released photon of energy  $\hbar\omega = E_G$  is in the visible range and also satisfies the energy ( $E_v = E_c - \hbar\omega$ ) and momentum ( $k_c = k_v = k_0$ ) conservation. GaAs and indium phosphide (InP) are examples of direct band gap semiconductors.

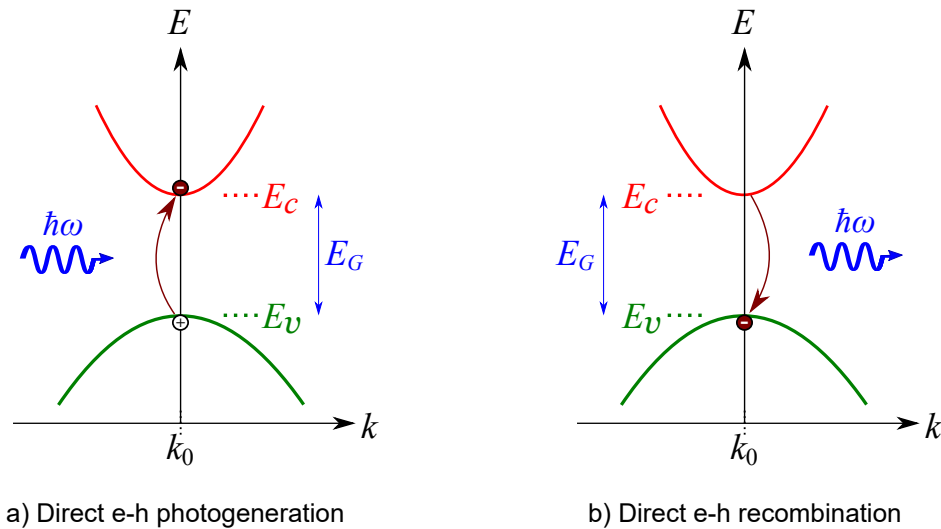


**Figure 4.4:** General representation of the E-k diagram for a direct band gap semiconductor. a) E-k diagram with the band-to-band photogeneration process. b) E-k diagram with the band-to-band recombination process.

#### 4.4.2 Indirect band gap semiconductors

The  $E - k$  diagram of an indirect band gap semiconductor [Gru16, Pie96, Nea11] is depicted in Fig. 4.5. In this case, the top of the valence band and the bottom of the conduction band have different momentum values ( $k_0 = 0$  and  $k_1 \neq 0$ , respectively). For this reason, two steps are required to accomplish the photogeneration process of Fig. 4.5a). In the step, labeled as  $a_0$ , the absorbed photon energy  $\hbar\omega = E_G$  only fulfills the energy conservation ( $E_c = E_v + \hbar\omega$ ). In the other step, labeled as  $b_0$ , the electron absorbs a phonon from the lattice which increases its momentum. This guarantees the



momentum conservation ( $k_1 = k_0 + \text{phonon}$ ).

Something similar happens in the recombination process of Fig. 4.5b). During step  $b_1$ , the electron loses some momentum by releasing a phonon, and through step  $a_1$ , the electron loses energy by releasing a photon of energy  $\hbar\omega = E_G$ . With both steps, momentum ( $k_0 = k_1 - \text{phonon}$ ) and energy ( $E_v = E_c - \hbar\omega$ ) conservation are satisfied. Si and Ge are examples of indirect band gap semiconductors.

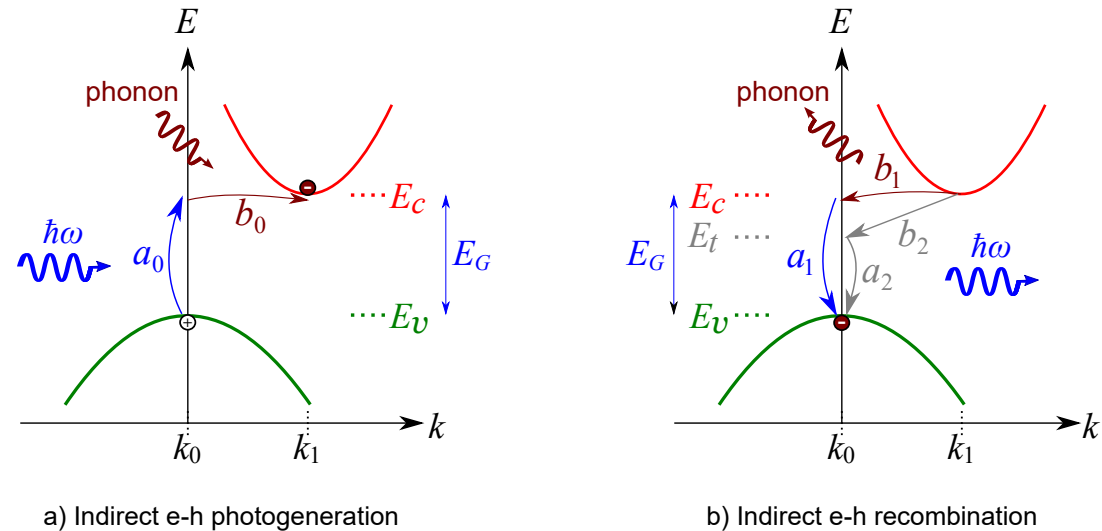


**Figure 4.5:** General representation of the E-k diagram for an indirect band gap semiconductor. a) E-k diagram with the band-to-band photogeneration process. b) E-k diagram with the band-to-band and R-G center recombination processes.

Nevertheless, the recombination process in indirect band gap semiconductors predominantly occurs in a different manner. Specifically, due to the presence of impurity atoms and defects in the lattice, some additional energy states within the band gap are created, as in the case of  $E_t$  in Fig. 4.5b). In the picture, during the two-step recombination process, first, through step  $b_2$ , the electron falls from  $E_c$  to  $E_t$  decreasing its momentum and losing energy at the same time. Then, through step  $a_2$ , the electron drops from  $E_t$  to  $E_v$  losing energy usually as heat. This recombination process is called *R-G center recombination* or *Recombination through traps*.

Additionally, strongly doped semiconductors experience a third principal recombination mechanism called *Auger recombination*. Here, basically, when an electron recombines with a hole, in parallel, a collision between the electron with another one occurs. On this occasion, the energy released in the process is transferred to one of the electrons which moves to a higher energy state in the conduction band, whereas the

other one decays to the valence band.

### 4.4.3 The recombination time

The time taken by an electron to transition from the conduction band to recombine with a hole in the valence band is called *recombination time* or *carrier lifetime*, denoted by  $\tau$  [HW83, KJS<sup>+</sup>19, DLI14]. This parameter is longer in indirect band gap semiconductors since, as shown in the foregoing subsection, the recombination process involves two general steps, unlike direct band gap semiconductors where only one step is necessary for the process. However, the parameter changes drastically depending on the quality (presence of impurities) of the semiconductor in the manufacturing process, as well as the density and type of doping. Consequently, encompassing all the recombination processes, the value of  $\tau$  can be estimated by:

$$\frac{1}{\tau} = \frac{1}{\tau_{B-B}} + \frac{1}{\tau_{R-G}} + \frac{1}{\tau_{Auger}}, \quad (4.4.2)$$

wherein  $\tau_{B-B}$  is the band-to-band recombination time,  $\tau_{R-G}$  is the R-G recombination time, and  $\tau_{auger}$  is the Auger recombination time, respectively.

## 4.5 Continuity equation

Considering all phenomena seen in sections 4.3 and 4.4, where the semiconductor was moved out of the equilibrium, the spatial and temporal distribution of the carrier concentration is described by the continuity equation [Pie96, LJ16, Nea11]. For an intrinsic semiconductor, the one-dimensional continuity equation is given by:

$$\frac{\partial \Delta n}{\partial t} = \frac{1}{e} \frac{\partial J}{\partial x} + G_g - \frac{\Delta n}{\tau}, \quad (4.5.1)$$

where  $\Delta n$  is the excess of carriers (for an intrinsic material it is the same for electrons and holes, denoted here as  $\Delta n$  for both),  $J$  is the total current density defined by Eq. (4.3.9),  $G_g$  is the carrier generation rate, and  $\frac{\Delta n}{\tau} = R_r$  is the carrier recombination rate. Assuming zero external electric fields (no presence of drift current), Eq. (4.5.1) becomes:

$$\frac{\partial \Delta n}{\partial t} = D \frac{\partial^2 \Delta n}{\partial x^2} + G_g - \frac{\Delta n}{\tau}, \quad (4.5.2)$$

wherein the carrier diffusion coefficient  $D$  can take the value of  $D_n$  or  $D_p$ .

### 4.5.1 Photon absorption and excess of carriers

In the photogeneration process it is assumed that every electron-hole pair is created by absorbing one photon, which implies a quantum efficiency  $\eta$  equal to 1 [RBBA17]. Therefore, the photon absorption rate is equal to the carrier generation rate [Nea11]. Assuming a uniform monochromatic light striking on the surface of an intrinsic semiconductor, the reduction of the light intensity going through the semiconductor obeys Lambert–Beer’s law [Bee52]:

$$I(z) = I_0 e^{-\alpha(\omega)x}, \quad (4.5.3)$$

where  $I_0$  is the optical power density of the light at the top of the surface,  $\alpha(\omega)$  is the frequency-dependent absorption coefficient of the material and  $x$  is the depth of penetration into the semiconductor. Most of the light is absorbed within a distance equal to the absorption length  $d_\alpha = 1/\alpha$ , so the thickness of the semiconductor must be greater than  $d_\alpha$  to absorb most of the light.

When the semiconductor with intrinsic carrier concentration  $n_i$  at thermal equilibrium is perturbed by the monochromatic excitation light, an excess of carriers  $\Delta n$  is produced. Thereby, once the system reaches its steady state ( $R_r = G_g$  which implicates no temporal dependence), the total carrier concentration  $N_n$  in the semiconductor is equal to  $N_n = n_i + \Delta n$ . Under such a non-time-dependent state and assuming a uniform photon absorption (no spatial dependence) and no saturation of the absorption over the volume  $V_l$  of the layer of thick  $d_\alpha$ , Eq. (4.5.2) leads to:

$$\begin{aligned} 0 &= 0 + G_g - \frac{\Delta n}{\tau} \\ \Delta n &= G_g \tau. \end{aligned} \quad (4.5.4)$$

In the foregoing equation, the carrier generation rate  $G_g$  is due to photogeneration, hence it depends on the characteristics of the light exciting the semiconductor. Therefore, by averaging the incident power density throughout  $V_l$  as  $I_{av} \approx 0.63I_0$ ,  $G_g$  is given by [KJS<sup>+</sup>19, RBBA17, MS08]:

$$G_g = \frac{I_{av}\eta\alpha}{E_{ph}}, \quad (4.5.5)$$

where  $E_{ph}$  is the photon energy of the excitation light. Then, by replacing (4.5.5) into (4.5.4), the excess of carriers is calculated as:

$$\Delta n = \frac{0.63I_0\eta\alpha}{E_{ph}}\tau. \quad (4.5.6)$$

Finally, when the excitation light is switched off ( $t = 0$ ),  $\Delta n$  often decays exponentially with time in the form [Nea11]:

$$\Delta n(t) = \Delta n(0)e^{-t/\tau}, \quad (4.5.7)$$

wherein  $\Delta n(0)$  is the initial excess carrier concentration calculated by Eq. (4.5.6).

## 4.6 Optical switch principle

At thermal equilibrium, a semiconductor in the intrinsic state in the absence of free carriers normally behaves transparently to incident waves within the microwave frequency range (1 GHz to 1000 GHz). As shown in the preceding sections, an increase in the carrier concentration tends to raise the electrical conductivity of the semiconductor. Then, when this increment is performed by a photogeneration process, the semiconductor is said to operate in a photoconductive state [KJS<sup>+</sup>19, Wei01]. In such a state, the semiconductor acts now as a reflector under the same incident GHz microwave radiation [HS96, DCKS04, KJS<sup>+</sup>19]. In general, as mentioned in section 1, controlling the on/off of the semiconductor's optical reflectivity through laser light is known as *Laser-driven semiconductor switch* (LDSS). Fig. 4.6 shows a schematic representation of the optical switch principle. Here, the reflection period  $t_p$  is determined by the duration  $t_n$  of the

excitation laser pulse (which is basically the time while the semiconductor is illuminated by the laser) and the carrier recombination time  $\tau$  of the semiconductor.

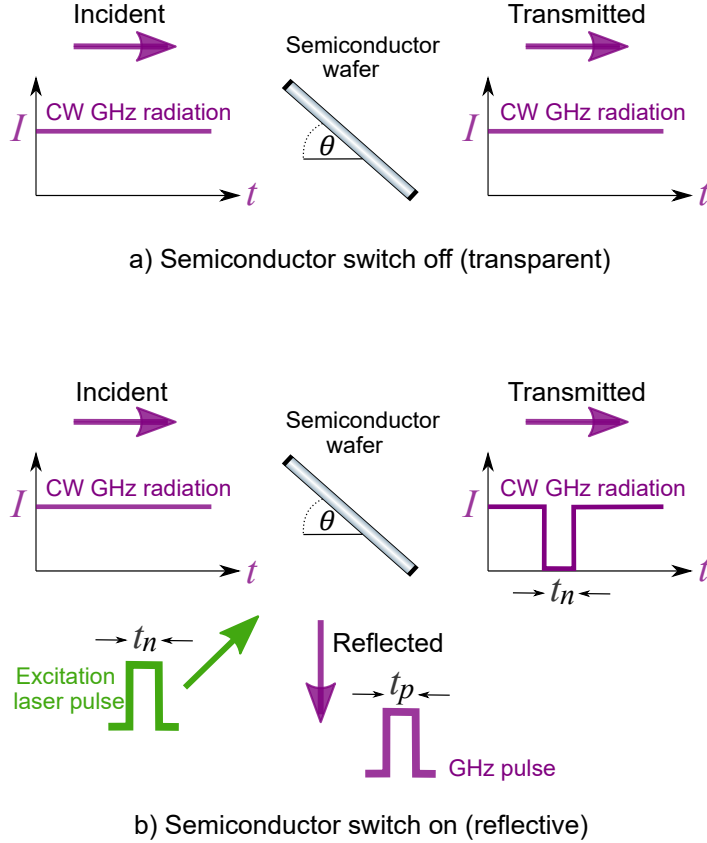


**Figure 4.6:**

Semiconductor wafer used as an optical switch. a) Switch off: the semiconductor is transparent to an incident microwave radiation. b) Switch on: under an excitation laser pulse, the semiconductor at the photoconductive state becomes reflective to the same incident microwave radiation.

### The plasma frequency ( $\omega_p$ )

Semiconductors have associated a frequency which is directly proportional to the carrier density called *plasma frequency* ( $\omega_p$ ). For incident frequencies below  $\omega_p$  the material becomes reflective and for frequencies above  $\omega_p$  the material acts transparently [KJS<sup>+</sup>19]. In other words,  $\omega_p$  can be roughly treated as the frequency point at which the semiconductor switch goes from on to off mode, and vice versa. Quantitatively,  $\omega_p$  is defined as [STvdL00, ZBC<sup>+</sup>01]:

$$\omega_p = \sqrt{\frac{N_n e^2}{\epsilon_0 m^*}}, \quad (4.6.1)$$

where  $N_n$  is the carrier concentration,  $e$  is the magnitude of the electron charge,  $\epsilon_0$  is the permittivity of free space and  $m^*$  is the effective mass of the charge.

### 4.6.1 The Drude-Lorentz model

The Drude-Lorentz model approach is a practical approximation widely used for analyzing, on a macroscopic scale, the dynamics involved in the optical switching behavior of an intrinsic semiconductor in the photoconductive state [KJS<sup>+</sup>19, PSR<sup>+</sup>19, BAF<sup>+</sup>18, MSB<sup>+</sup>14, VDH<sup>+</sup>92]. Eventually, this will enable the estimation of the degree of reflectance reached by the semiconductor to the incident microwave radiation.

#### The Lorentz model

The response of a dielectric material to a weak external electric field  $E$  of angular frequency  $\omega$  is manifested through the polarization process [KM18], in which the created dipoles per unit volume  $N$  oscillate at frequency  $\omega$ . Considering an isotropic dielectric medium and assuming the field in the form  $E(t) = E_0 e^{-i\omega t}$ , the equation of motion experienced by the electron in the dipole system is described by the general Lorentz oscillator model [ABB11, Woo72] for dielectrics in the form:

$$m_e \frac{\partial^2 x(t)}{\partial t^2} = \underbrace{eE(t)}_{\text{Electric force}} - \overbrace{m_e \Gamma \frac{\partial x(t)}{\partial t}}^{\text{Damping force}} - \underbrace{\omega_0^2 m_e x(t)}_{\text{Restoring force}}, \quad (4.6.2)$$

where  $x(t)$  is the electron position vector,  $m_e$  is the electron rest mass,  $\Gamma$  is the damping coefficient and  $\omega_0$  is the natural resonance frequency of the system. Three forces are involved in the total resulting force in the last equation: the electric force induced by  $E$ ; the damping force that accounts for the losses by frictions in the system; and the restoring force, which, similar to the classical harmonic oscillator, tends to bring back the system to its natural equilibrium position as when  $E$  was not present. In the end, the resulting force induces an average acceleration  $\frac{\partial^2 x(t)}{\partial t^2}$  on the electron in the dipole. Thus, after applying Fourier's transform, the solution of Eq. (4.6.2) in the frequency domain is given by:

$$\tilde{x}(\omega) = \frac{e}{m_e} \cdot \frac{\tilde{E}(\omega)}{\omega_0^2 - \omega^2 - i\omega\Gamma}. \quad (4.6.3)$$

The dipole moment of an electron is defined as  $p(\omega) = e\tilde{x}(\omega)$ . Then, the replacement of Eq. (4.6.3) into this definition produces:

$$p(\omega) = e\tilde{x}(\omega) = \frac{e^2}{m_e} \cdot \frac{\tilde{E}(\omega)}{\omega_0^2 - \omega^2 - i\omega\Gamma}. \quad (4.6.4)$$

Thereby, the average polarization  $P(\omega)$  of the system composed of all the dipoles is given by the number of dipoles per unit volume  $N$  multiplied by the dipole moment  $p(\omega)$  as follows:

$$P(\omega) = Np(\omega) = \frac{Ne^2}{m_e} \cdot \frac{\tilde{E}(\omega)}{\omega_0^2 - \omega^2 - i\omega\Gamma}. \quad (4.6.5)$$

Equivalently, the polarization is linearly related to the external electric field  $E$  through the scalar dielectric susceptibility  $\chi(\omega)$  in the form [KM18, Ham17]:

$$P(\omega) = \varepsilon_0\chi(\omega)\tilde{E}(\omega). \quad (4.6.6)$$

Therefore, by comparing Eq. (4.6.5) with Eq. (4.6.6), the mathematical expression of  $\chi(\omega)$  is given by:

$$\chi(\omega) = \frac{Ne^2}{\varepsilon_0 m_e} \cdot \frac{1}{\omega_0^2 - \omega^2 - i\omega\Gamma}. \quad (4.6.7)$$

As well as  $\chi(\omega)$ , the polarization capacity of a dielectric is usually quantified by the relative permittivity parameter  $\tilde{\varepsilon}_r$  whose expression as a function of frequency is defined as:

$$\tilde{\varepsilon}_r(\omega) = 1 + \chi(\omega) = 1 + \frac{Ne^2}{\varepsilon_0 m_e} \cdot \frac{1}{\omega_0^2 - \omega^2 - i\omega\Gamma}. \quad (4.6.8)$$

### The Drude model

The Drude model describes the response of a metal to an external electric field [Mai07, Woo72]. It is basically derived from the Lorentz dielectric model, but with the difference that the natural resonance frequency is now  $\omega_0 = 0$ . This happens because the electrons in the metal conduction band are not bound to the lattice so they move freely through it, without experiencing a restoring force. In other words,  $E$  tends to accelerate the electrons in the lattice. Thus, in this model, it is found that:

$$\tilde{\varepsilon}_r(\omega) = 1 - \frac{N_n e^2}{\varepsilon_0 m_n^*} \cdot \frac{1}{\omega^2 + i\omega\Gamma}, \quad (4.6.9)$$

where now  $N_n$  is interpreted as the free electron concentration and  $m_n^*$  as the electron effective mass.

### The generalized Drude-Lorentz model

Because of its metal like nature, a semiconductor in the photoconductive state can be compared and analyzed under the Drude model. However, actual semiconductors have many resonance frequencies. For this reason, a more suitable analysis can be done by the generalized Drude-Lorentz model [KJS<sup>+</sup>19, ECC14, Mai07] in which both models are somehow combined. Specifically, the model considers  $\omega_0 = 0$  and the contribution of high-order resonance frequencies to the relative permittivity, wherein the latter is carried out through an average DC offset value denoted as  $\varepsilon_\infty$ . Therefore, for a semiconductor at the photoconductive state,  $\tilde{\varepsilon}_r(\omega)$  is given by:

$$\tilde{\varepsilon}_r(\omega) = \varepsilon_\infty - \frac{N_n e^2}{\varepsilon_0 m_n^*} \cdot \frac{1}{\omega^2 + i\omega\Gamma}. \quad (4.6.10)$$

which extended in terms of electrons and holes results in:

$$\tilde{\varepsilon}_r(\omega) = \varepsilon_\infty - \frac{N_n e^2}{\varepsilon_0 m_n^*} \cdot \frac{1}{\omega^2 + i\omega\Gamma_n} - \frac{N_p e^2}{\varepsilon_0 m_p^*} \cdot \frac{1}{\omega^2 + i\omega\Gamma_p}. \quad (4.6.11)$$

where  $m_n^*$  and  $m_p^*$  are the electron and hole effective mass, and  $\Gamma_n$  and  $\Gamma_p$  are the electron and hole damping coefficient, respectively. Subsequently, by separating  $\tilde{\varepsilon}_r(\omega)$  into its real  $\varepsilon'_r(\omega)$  and imaginary part  $\varepsilon''_r(\omega)$ , Eq. (4.6.11) becomes:

$$\tilde{\varepsilon}_r(\omega) = \varepsilon'_r(\omega) + i\varepsilon''_r(\omega), \quad (4.6.12)$$

with:



$$\varepsilon'_r(\omega) = \varepsilon_\infty - \left[ \frac{\omega_{pn}^2}{\omega^2 + \Gamma_n^2} + \frac{\omega_{pp}^2}{\omega^2 + \Gamma_p^2} \right], \quad (4.6.13)$$

$$\varepsilon''_r(\omega) = \frac{\omega_{pn}^2 \Gamma_n}{\omega^3 + \omega \Gamma_n^2} + \frac{\omega_{pp}^2 \Gamma_p}{\omega^3 + \omega \Gamma_p^2}, \quad (4.6.14)$$

wherein  $\omega_{pn} = \sqrt{N_n e^2 / \varepsilon_0 m_n^*}$  and  $\omega_{pp} = \sqrt{N_p e^2 / \varepsilon_0 m_p^*}$  are the electron and hole plasma frequency (see Eq. (4.6.1)), respectively.

The damping coefficients  $\Gamma_n$  and  $\Gamma_p$  in the foregoing equations account for the loss of carrier mobility, mainly due to the lattice scattering process (see section 4.3.1). With the sub-index  $q$  taking the value of  $n$  or  $p$  (depending on the carrier case under analysis), a mean value of this parameter is determined by:

$$\Gamma_q = \frac{1}{\tau_q}, \quad (4.6.15)$$

where  $\tau_q$  is the average time of the carrier between collisions defined in terms of the carrier mobility factor  $\mu_q$  viewed in Eq. (4.3.2) as:

$$\tau_q = \frac{\mu_q m_q^*}{e}. \quad (4.6.16)$$

## 4.6.2 Complex refractive index

Throughout the medium, the propagation of the wave associated with  $\tilde{E}(\omega)$  is characterized by the complex refractive index  $\tilde{n}(\omega)$  described by:

$$\tilde{n}(\omega) = n_r(\omega) + i\kappa(\omega). \quad (4.6.17)$$

The real part  $n_r(\omega)$  is responsible for the phase velocity of the wave, whereas the imaginary part  $\kappa(\omega)$ , called *extinction coefficient*, is responsible for the losses by absorption experienced by the wave in the material [Dre01, ABB11]. For a non-magnetic medium (as the semiconductor case),  $\tilde{n}(\omega)$  and  $\tilde{\varepsilon}_r(\omega)$  are related to each other by:

$$\tilde{n}^2(\omega) = \tilde{\varepsilon}_r(\omega). \quad (4.6.18)$$

Eventually, the substitution of Eqs. (4.6.12) and (4.6.17) into Eq. (4.6.18) leads to establish  $n_r(\omega)$  and  $\kappa(\omega)$  in terms of  $\varepsilon_r'(\omega)$  and  $\varepsilon_r''(\omega)$  as follows:

$$n_r(\omega) = \sqrt{\frac{\sqrt{\varepsilon_r'^2(\omega) + \varepsilon_r''^2(\omega)} + \varepsilon_r'(\omega)}{2}}. \quad (4.6.19)$$

$$\kappa(\omega) = \sqrt{\frac{\sqrt{\varepsilon_r'^2(\omega) + \varepsilon_r''^2(\omega)} - \varepsilon_r'(\omega)}{2}}. \quad (4.6.20)$$

### 4.6.3 Reflectance at the photoconductive state

The equations obtained so far enable to determine a mathematical expression for the intensity reflectance  $R_p$  of the SW in the photoconductive state. To this end, a multilayer system is considered, similar to the one shown in Fig. 3.5. This means, the incident wave of angular frequency  $\omega$  travels through the structure formed by air (layer 0), the semiconductor wafer (layer 1), and air (layer 2). Thus, recalling from section 3.3, the  $2 \times 2$  transfer matrix  $M$  associated with the structure is given by:

$$M = \frac{1}{t_{01}t_{12}} \begin{pmatrix} e^{i\beta_1} + r_{01}r_{12}e^{-i\beta_1} & r_{01}e^{-i\beta_1} + r_{12}e^{i\beta_1} \\ r_{01}e^{i\beta_1} + r_{12}e^{-i\beta_1} & e^{-i\beta_1} + r_{01}r_{12}e^{i\beta_1} \end{pmatrix}, \quad (4.6.21)$$

where  $r_{01}$  and  $t_{01}$  are the reflection and transmission Fresnel coefficients [BW03] in border  $01$  between layers 0 and 1, and  $r_{12}$  and  $t_{12}$  are the reflection and transmission Fresnel coefficients in border  $12$  between layers 1 and 2, respectively. For  $p$  polarization, they are defined by:

$$r_{01}(p) = \frac{\tilde{n} \cos \theta_0 - n_0 \cos \theta_1}{\tilde{n} \cos \theta_0 + n_0 \cos \theta_1} = \frac{(n_r + i\kappa) \cos \theta_0 - \cos \theta_1}{(n_r + i\kappa) \cos \theta_0 + \cos \theta_1}, \quad (4.6.22)$$

$$t_{01}(p) = \frac{2n_0 \cos \theta_0}{\tilde{n} \cos \theta_0 + n_0 \cos \theta_1} = \frac{2 \cos \theta_0}{(n_r + i\kappa) \cos \theta_0 + \cos \theta_1}, \quad (4.6.23)$$

$$r_{12}(p) = \frac{n_2 \cos \theta_1 - \tilde{n} \cos \theta_2}{n_2 \cos \theta_1 + \tilde{n} \cos \theta_2} = \frac{\cos \theta_1 - (n_r + i\kappa) \cos \theta_2}{\cos \theta_1 + (n_r + i\kappa) \cos \theta_2}, \quad (4.6.24)$$

$$t_{12}(p) = \frac{2\tilde{n} \cos \theta_1}{n_2 \cos \theta_1 + \tilde{n} \cos \theta_2} = \frac{2(n_r + i\kappa) \cos \theta_1}{\cos \theta_1 + (n_r + i\kappa) \cos \theta_2}, \quad (4.6.25)$$

where  $n_r$  and  $\kappa$  are described by Eqs. (4.6.19) and (4.6.20), respectively, and  $\theta_0$ ,  $\theta_1$  and  $\theta_2$  are the angles of incidence and refraction throughout the structure which are related to each other by Snell's law [YF09].

In Eq. (4.6.21),  $\beta_1$  represents the phase change of the wave along the semiconductor (layer 1). It is described by  $\beta_1 = kl \cos \theta_1 = \frac{2\pi}{\lambda} \tilde{n} l \cos \theta_1$ , where  $\lambda$  is the wavelength of the incident wave,  $l$  is the semiconductor thickness,  $\theta_1$  is the propagation angle of the wave inside the semiconductor and  $\tilde{n}$  is the refractive index of the semiconductor given by Eq. (4.6.17).

All in all, after obtaining the matrix elements in Eq. (4.6.21),  $R_p$  is finally calculated by:

$$r_p = \frac{M_{21}}{M_{11}} \implies R_p(\omega, N_n) = |r_p|^2. \quad (4.6.26)$$

## 4.7 Simulated response of semiconductors

This section presents some simulations and calculations employing the equations derived in the previous ones. Table 4.1 shows the parameters taken from the literature of intrinsic Si and intrinsic GaAs semiconductors at room temperature that are considered for this purpose. The value of the thickness of the SW and the quantum efficiency is also added to the table.

**Table 4.1:** Intrinsic Si and GaAs parameters at room temperature (T=300 K)

Parameter	Symbol	Si	GaAs
Energy band gap	$E_G$	1.12 eV (or $1.792 \times 10^{-19}$ J)	1.42 eV (or $2.272 \times 10^{-19}$ J)
Carrier concentration	$n_i$	$1 \times 10^{10} \text{ cm}^{-3}$	$2 \times 10^6 \text{ cm}^{-3}$
Electron elemental charge	$e$	$1.6022 \times 10^{-19} \text{ C}$	$1.6022 \times 10^{-19} \text{ C}$
High-frequency permittivity constant	$\epsilon_\infty$	11.68	12.88
Electron rest mass	$m_e$	$9.11 \times 10^{-31} \text{ Kg}$	$9.11 \times 10^{-31} \text{ Kg}$
Electron effective mass	$m_n^*$	$\sim 0.26 \cdot m_e$	$\sim 0.063 \cdot m_e$
Hole effective mass	$m_p^*$	$\sim 0.37 \cdot m_e$	$\sim 0.51 \cdot m_e$
Electron mobility factor	$\mu_n$	$1350 \text{ cm}^2/\text{V-s}$	$8500 \text{ cm}^2/\text{V-s}$
Hole mobility factor	$\mu_p$	$480 \text{ cm}^2/\text{V-s}$	$400 \text{ cm}^2/\text{V-s}$
Electron average collision time	$\tau_n$	$\sim 0.2 \text{ ps}$	$\sim 0.3 \text{ ps}$
Hole average collision time	$\tau_p$	$\sim 0.1 \text{ ps}$	$\sim 0.1 \text{ ps}$
Recombination time	$\tau$	$\sim 1 \mu\text{s}$	$\sim 10 \text{ ns}$
Absorption coefficient at 3 mm	$\alpha_1$	$< 0.02 \text{ cm}^{-1}$	$\sim 0.4 \text{ cm}^{-1}$
THz absorption length at 3 mm for $\alpha_1$	$d_{\alpha_1} = 1/\alpha_1$	$> 50 \text{ cm}$	$\sim 2.5 \text{ cm}$
Absorption coefficient at 532 nm	$\alpha_2$	$\sim 7.6 \times 10^3 \text{ cm}^{-1}$	$\sim 7.9 \times 10^4 \text{ cm}^{-1}$
Optical absorption length at 532 nm for $\alpha_2$	$d_{\alpha_2} = 1/\alpha_2$	$\sim 1.3 \mu\text{m}$	$\sim 0.12 \mu\text{m}$
SW thickness	$l$	1 mm	1 mm
Quantum efficiency	$\eta$	1	1

Recalling from chapter 3, the SW between the cavity concave mirrors was positioned at an angle  $\theta_0 = \phi = 68^\circ$  with the cavity closed. Under this angle, Fig. 4.7 illustrates a simulation of the reflective response of the Si and GaAs wafer under different values of  $N_n$  and for a 100 GHz incident wave. According to the curve on the left for silicon, the reflectivity at the intrinsic concentration  $N_n = 10^{10} \text{ cm}^{-3}$  is about  $R_p = 0.026$ , around 0.004 less than the measured value. Such amount remains until  $N_n = 10^{16} \text{ cm}^{-3}$  from where  $R_p$  starts growing progressively with  $N_n$  achieving a reflectance over 0.75 for  $N_n \geq 10^{18} \text{ cm}^{-3}$ . The plot on the right corresponds to the GaAs case where at the intrinsic carrier concentration  $N_n = 10^6 \text{ cm}^{-3}$ , it is found that  $R_p \approx 0.072$ , which is about 0.01 less than the measured value. Furthermore, from  $N_n = 10^6 \text{ cm}^{-3}$  the reflectivity starts increasing continuously achieving a  $R_p > 0.85$  for  $N_n \geq 10^{18} \text{ cm}^{-3}$ . It can be concluded that GaAs reaches a reflectance greater than Si for the same carrier concentration.

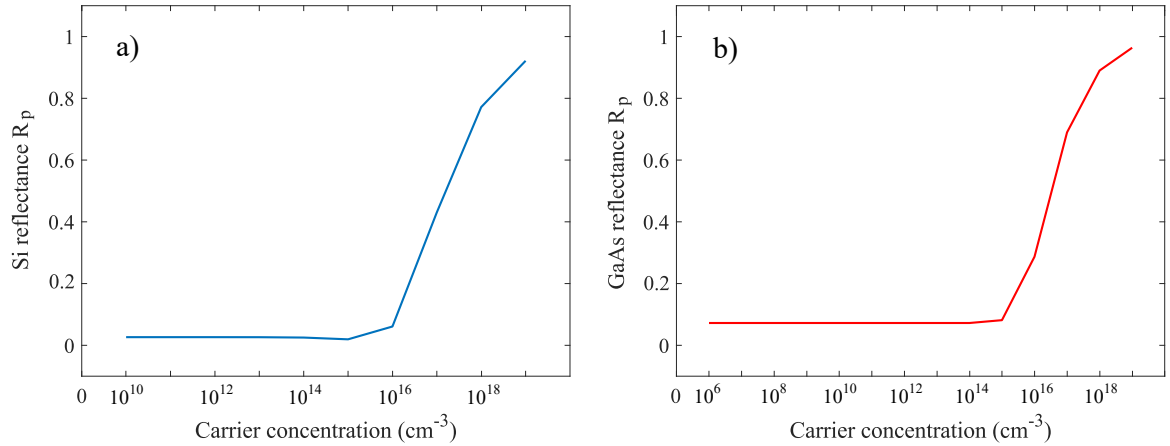


**Figure 4.7:** Simulated reflectance of semiconductor wafer positioned at  $\theta_0 = 68^\circ$  under different carrier concentrations for a 100 GHz incident wave. a) Si. b) GaAs.

By changing the angle  $\theta_0$ , the reflectance response of the semiconductor at different  $N_n$  varies for the Si case as shown in Fig. 4.8 and for the GaAs case as depicted in Fig. 4.9. The average plasma frequency  $\nu_p = \omega_p/2\pi$  associated with every  $N_n$  is also shown in the figures. Focusing first on Fig. 4.8, it can be observed that under Brewster's angle  $\theta_B = \theta_0 = 73.7^\circ$ , for  $10^{10} \leq N_n \leq 10^{15} \text{ cm}^{-3}$  the reflection is around zero. However, due to an increment in the real part of the refractive index, for  $N_n \geq 10^{16} \text{ cm}^{-3}$  there is no angle at which  $R_p$  is low. Furthermore, for concentrations over  $10^{18} \text{ cm}^{-3}$ , a  $R_p > 0.8$  can be achieved for  $\theta_0 < 60^\circ$ . Looking now at Fig. 4.9 for GaAs, at Brewster's angle  $\theta_B = \theta_0 = 74.4^\circ$ , a  $R_p \approx 0$  in the interval  $10^{10} \leq N_n \leq 10^{14} \text{ cm}^{-3}$  is found, but for

$N_n \geq 10^{15} \text{ cm}^{-3}$  a substantial reflectivity for all values of  $\theta_0$  is observed. Besides, for concentrations over  $10^{18} \text{ cm}^{-3}$ , an  $R_p > 0.9$  is reached for  $\theta_0 < 60^\circ$ , which is around 10% bigger than the silicon case.

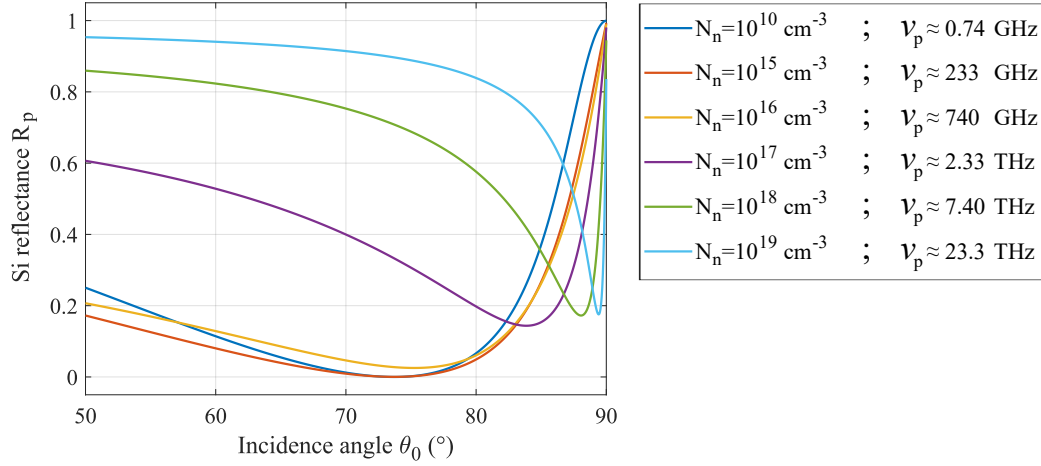


**Figure 4.8:** Computed reflectivity of 100 GHz radiation reflected of a 1 mm thick silicon wafer for different carrier concentrations and angles of incidence.

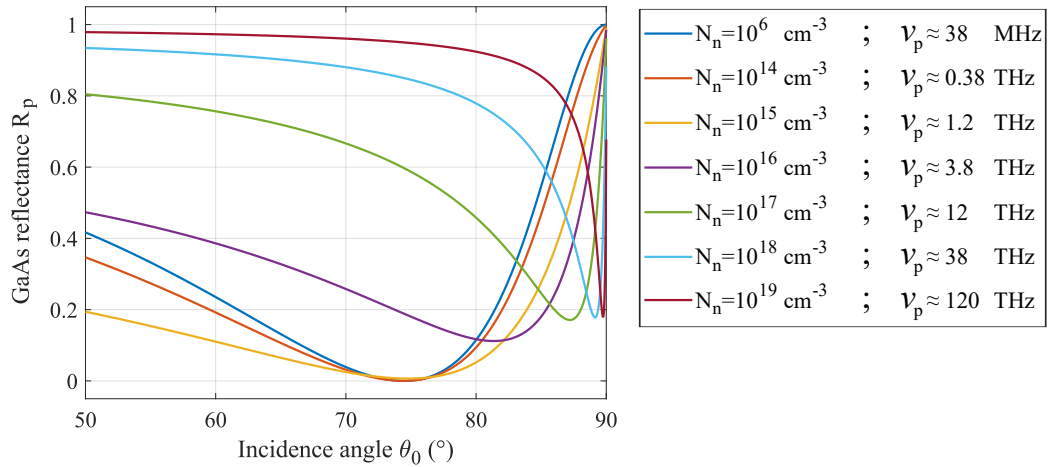


**Figure 4.9:** Computed reflectivity of 100 GHz radiation reflected of a 1 mm thick GaAs wafer for different carrier concentrations and angles of incidence.

It should be pointed out that Brewster's angle would be the ideal position to place the SW since a very small reflectance, close to zero, brings minimal losses to the cavity, which in the end contributes to optimizing the enhancement factor. However, this was not experimentally possible due to the size of the incident beam which was larger than the semiconductor surface under such an angle.

### 4.7.1 Power requirements of the excitation laser

According to Fig. 4.7, a carrier density  $N_n = 10^{19} \text{ cm}^{-3}$  ensures a reflectance  $R_p > 0.9$  for both semiconductors. At this concentration, the excess of carriers can be approximated to  $\Delta n = N_n - n_i \approx N_n$ . Considering a 532-nm, 7-ns excitation laser pulse with an associated photon energy  $E_{ph} = \hbar\omega = 3.74 \times 10^{-19} \text{ J}$ , by solving  $I_0$  in Eq. (4.5.6), it follows that for Si:

$$I_0 = \frac{N_n \cdot E_{ph}}{0.63 \cdot \eta \cdot \alpha_2 \cdot \tau} = \frac{10^{19} \text{ cm}^{-3} \cdot 3.734 \times 10^{-19} \text{ J}}{0.63 \cdot 1 \cdot 7.6 \times 10^3 \text{ cm}^{-1} \cdot 1 \times 10^{-6} \text{ s}} \approx 800 \frac{\text{W}}{\text{cm}^2}, \quad (4.7.1)$$

and for GaAs:

$$I_0 = \frac{N_n \cdot E_{ph}}{0.63 \cdot \eta \cdot \alpha_2 \cdot \tau} = \frac{10^{19} \text{ cm}^{-3} \cdot 3.734 \times 10^{-19} \text{ J}}{0.63 \cdot 1 \cdot 7.9 \times 10^4 \text{ cm}^{-1} \cdot 10 \times 10^{-9} \text{ s}} \approx 7.5 \frac{\text{kW}}{\text{cm}^2}. \quad (4.7.2)$$

Recalling from section 3.2, the profile of the 100 GHz radiation beam located at the center between the concave mirrors of the designed bow-tie cavity has the shape described by the simulation in Fig. 3.3d). As it is well known, the semiconductor switch will be placed around this position inside the resonator, hence, in order to reflect the entire beam from the cavity, the excitation laser must overlap the whole beam profile. Nevertheless, when the SW is placed at Brewster's angle  $\theta_B$  at the center between the concave mirrors, the 100 GHz beam profile on the semiconductor surface resembles the elliptical shape depicted in Fig. 4.10.

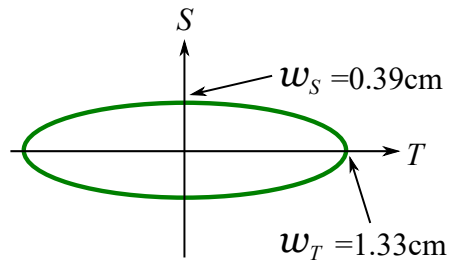


**Figure 4.10:** Simulated beam profile on the SW surface at  $\theta_B$  located at the center between the cavity concave mirrors.

Then, taking into account the major axis of the ellipse of Fig. 4.10, the circular area to cover by the excitation laser would be around  $A = \pi \cdot w_T^2 = 5.56 \text{ cm}^2$ . However, knowing that the actual angle of SW is  $\theta_0 = 68^\circ$  (instead of  $\theta_B$ ), a circular laser beam

with a radius of  $2.5\text{ cm}$  is considered to ensure a total superposition between the beams. This radius leads to a laser beam area of  $A \approx 20\text{ cm}^2$  which should be sufficient to overlap the whole reflective zone of interest of the SW. Therefore, assuming a uniform power distribution, the illumination intensity  $I_0$  computed for Si in Eq. (4.7.1) yields a laser pulse peak power of:

$$P = I_0 \cdot A = 800 \frac{W}{\text{cm}^2} \cdot 20\text{ cm}^2 = 16\text{ kW}. \quad (4.7.3)$$

In addition, for a laser pulse duration of  $t = 7\text{ ns}$ , the minimum effective energy per pulse necessary to accomplish over 90% of reflection is:

$$E = P \cdot t = 112\ \mu\text{J}. \quad (4.7.4)$$

Similarly, by using the result of Eq. (4.7.2), the power and energy requirements for an  $R_p > 0.9$  in the GaAs case are:

$$P = I_0 \cdot A = 7500 \frac{W}{\text{cm}^2} \cdot 20\text{ cm}^2 = 150\text{ kW}. \quad (4.7.5)$$

$$E = P \cdot t = 1\text{ mJ}. \quad (4.7.6)$$

As shown earlier in Fig. 4.7, GaAs provides a higher  $R_p$  than Si under the same  $N_n$ . However, the calculations performed throughout this section indicate that GaAs needs an excitation laser intensity (and consequently a laser pulse energy) approximately 9 times greater than that required by Si in order to generate the same amount of carrier concentration.



## 4.8 Experimental results

Fig. 4.11 depicts the optical arrangement with the SW acting as an optical switch. First, in the setup shown on the left, the power  $P$  of the 100 GHz p-polarized input radiation is measured. Then, in the setup shown on the right, the SW placed at  $\phi = 68^\circ$  is excited to its photoconductive state by a 532-nm, 7-ns laser pulse with a pulse energy  $E_L$  gradually increased from 0.2 to 50 mJ. This causes the wafer to become reflective to the incident 100 GHz radiation. The laser shines on the SW at around  $\sim 10^\circ$  regarding the normal incidence and has a circular shape with a radius of 2.5 cm. Besides, it is generated from a second harmonic generation (SHG) process by a type-I BBO crystal model 2NLC95, with a 1064-nm, 10-Hz,  $\sim 7$ -ns, 2-J fundamental pump laser pulse provided by a Continuum Q-switched/cavity dumped RGA, model Intrepid.

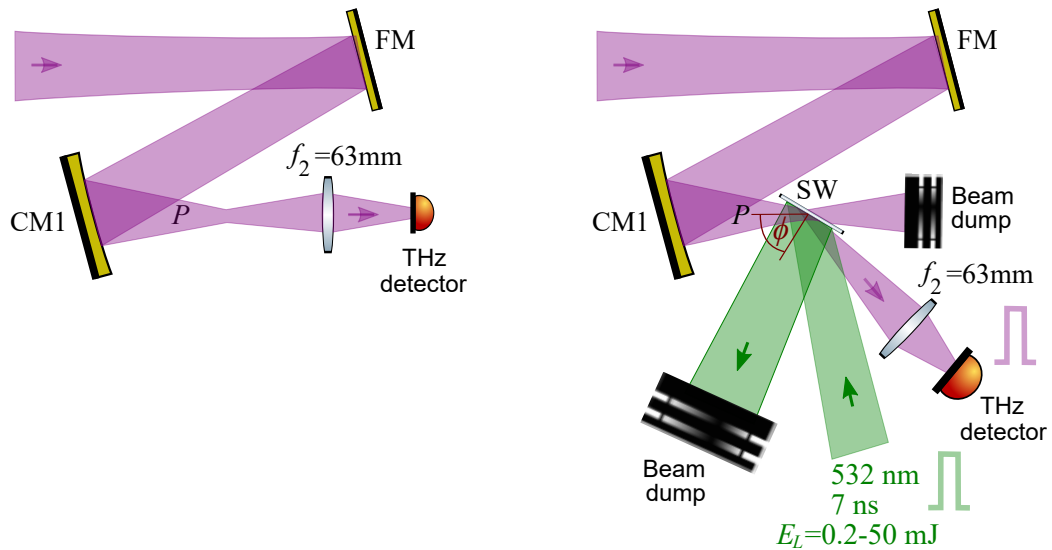


**Figure 4.11:** Experimental setup. Measurement of the input power  $P$  (left). Semiconductor wafer excited to the photoconductive state by a 532-nm, 7-ns laser pulse (right).

### 4.8.1 Results for intrinsic silicon semiconductor wafer

#### Reflectivity dependence on laser energy

Fig. 4.12 shows a sequence of pictures with the evolution of the 100 GHz radiation reflected by the SW as the excitation laser energy  $E_L$  increases. In the beginning, without the presence of the excitation laser, the semiconductor remains in its intrinsic state reflecting around  $\sim 6.0 \mu\text{W}$  of power, however, when the laser shines the wafer an

increment of the carrier density on the surface produces the higher reflectivity which is manifested through the pulse of the figures. It can be observed that the bigger  $E_L$ , the stronger the reflectivity, i.e, the larger the peak power of the reflected pulse. Afterward, when the laser is off, the carriers start to recombine and diffuse, and then the carrier density goes down in where a little amount is reflected and some portion is absorbed. This situation is especially seen in the decay time of the pulse in Figs. a) and d): once the semiconductor returns to the intrinsic state, the reflected power decreases below  $\sim 6.0 \mu\text{W}$ , which means that the light is being absorbed. Finally, it takes a few tens of microseconds until the carriers die and get back to intrinsic operation.

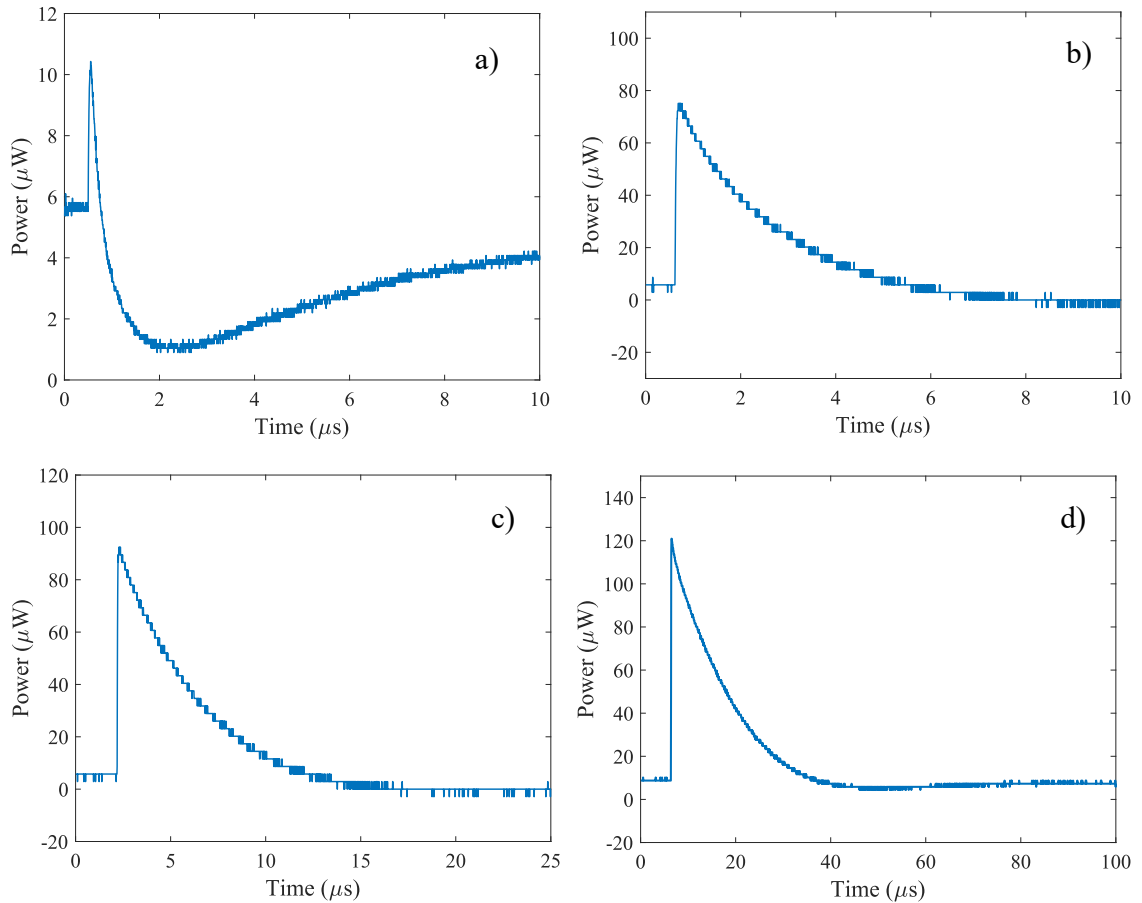


**Figure 4.12:** Evolution of the 100 GHz signal reflected by the Si wafer for different excitation laser energies. a)  $E_L = 0.23 \text{ mJ}$ . b)  $E_L = 2.9 \text{ mJ}$ . c)  $E_L = 8.9 \text{ mJ}$ . d)  $E_L = 50 \text{ mJ}$ .

For a measured input power of  $P = 180 \mu\text{W}$ , the reflective response of the silicon wafer along the entire energy range of the excitation laser is summarized in Fig. 4.13. According to the plot on the left, the curve does not reach saturation regardless of its

low increment in power after  $E_L \approx 30$  mJ. On the other hand, looking at the graph on the right, a maximum reflectance of  $R_p \approx 0.67$  is achieved, corresponding to a power of  $120 \mu\text{W}$ .

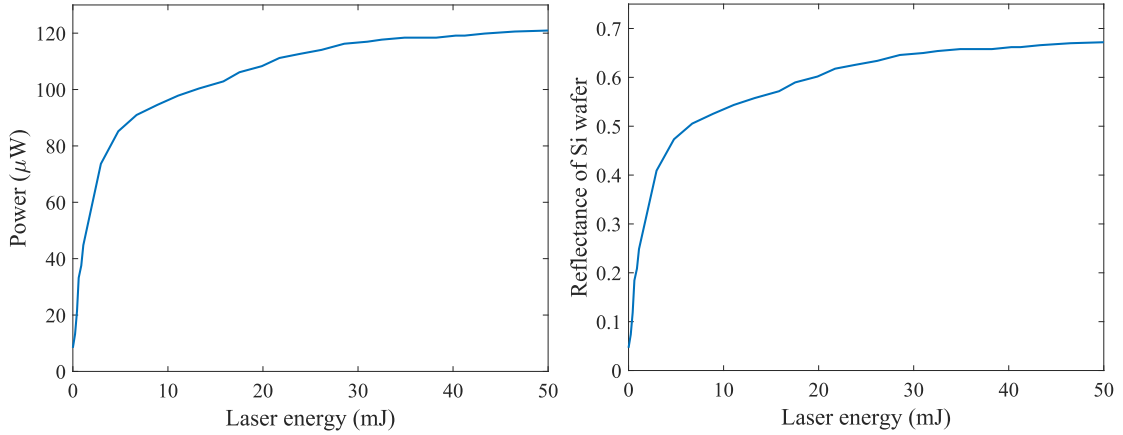


**Figure 4.13:** 100 GHz reflectance response by the Si wafer versus the excitation laser energy. Peak power of the reflected pulse (left). Equivalence of the peak power in reflected percentage (right).

### Rise and decay time of silicon reflectance response

The switching speed of the semiconductor between the transparent and reflective operation is a fundamental factor in the efficiency of the radiation extraction process from the cavity, as will be discussed in the next chapter. Specifically, it is crucial to know the rise time  $t_{rs}$  and decay time  $t_{ds}$  of the reflectance response to explain and understand what happens during such a process. To determine these parameters, Fig. 4.14 displays the foregoing Fig. 4.12d) under two different time scales. Focusing first on Fig. 4.14a), once the laser hits the wafer at instant  $x_1$ , this plot shows how the reflected signal grows over time. The points denoted as  $x_1$  and  $x_2$  represent the moment of minimum and maximum reflected light power, respectively. In other words, at  $x_1$  the SW operates mostly transparent to the incident 100 GHz radiation and at  $x_2$  achieves its maximum reflectance. Therefore, the rise time is around  $t_{rs} = x_2 - x_1 \approx 57$  ns.

On the other hand, Fig. 4.14b) illustrates the way how the reflected signal returns to its transparent state once the excitation laser is off. It is observed that the FWHM of the pulse is about  $9 \mu\text{s}$ . The point  $x_3$  corresponds to the moment of maximum reflected light power and  $x_4$  to the minimum one. As a result, the decay time of the pulse power (and in consequence of the reflectance) is about  $t_{ds} = x_4 - x_3 \approx 29 \mu\text{s}$ .

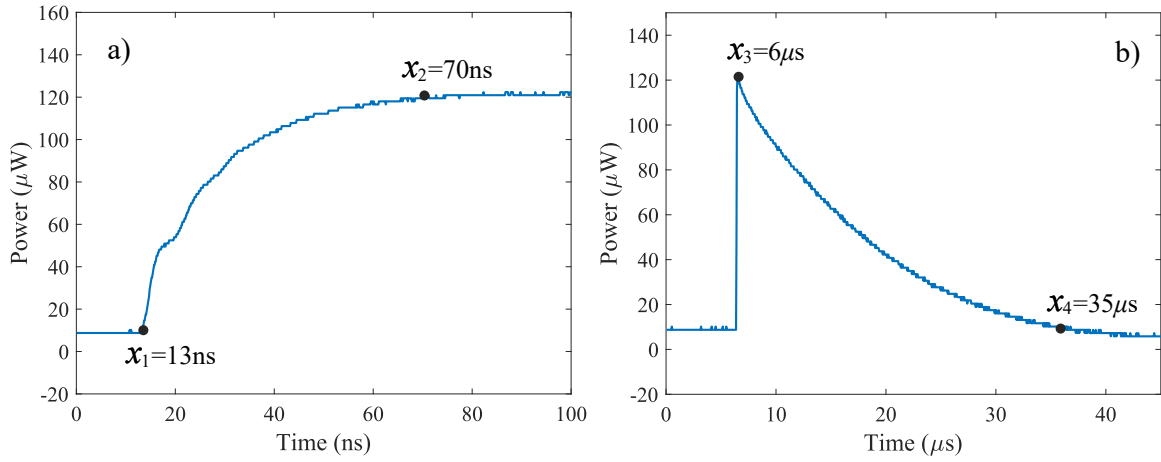


**Figure 4.14:** Reflected pulse by the Si wafer for a  $E_L=50\text{ mJ}$ . a) Shorter time scale. b) Longer time scale.

## 4.8.2 Results for intrinsic GaAs semiconductor wafer

### Reflectivity dependence on laser energy

By implementing the experimental setup of Fig. 4.11, Fig. 4.15 shows a sequence of pictures with the evolution of the 100 GHz signal reflected by the GaAs wafer as  $E_L$  increases. At the beginning, without the presence of the excitation laser, the semiconductor remains in its intrinsic state reflecting a power around  $\sim 16\ \mu\text{W}$  but when the laser acts on it, the reflectivity increases due to the increments of carriers in the surface. This manifested through the pulse shown in the figures. It can be seen that the bigger  $E_L$  the larger the peak power of the reflected pulse. Afterward, when the laser is off, the carriers rapidly start to recombine and diffuse until the concentration get back to intrinsic operation. However, unlike the case of silicon, the semiconductor does not undergo a perceptible induced absorption once it returns to its intrinsic state.

A summary of the reflective response of the GaAs wafer along the whole energy range of  $E_L$  is shown in the curves of Fig. 4.16. It is observed that, like the silicon case, this time the response does not reach saturation either. Nevertheless, according to the plot on the right and considering an input power of  $P = 180\ \mu\text{W}$ , a remarkable difference is that the maximum reflectance achieved is  $R_p \approx 0.59$  which is around  $\sim 0.08$  less than the one reached by silicon. This discrepancy enables to state that intrinsic GaAs requires more laser energy than intrinsic Si to reflect the same amount of power, demonstrating the conclusion obtained from the calculations in section 4.7.1. This also explains why the slope of the curve above  $E_L = 30\text{ mJ}$  is steeper in GaAs than Si.

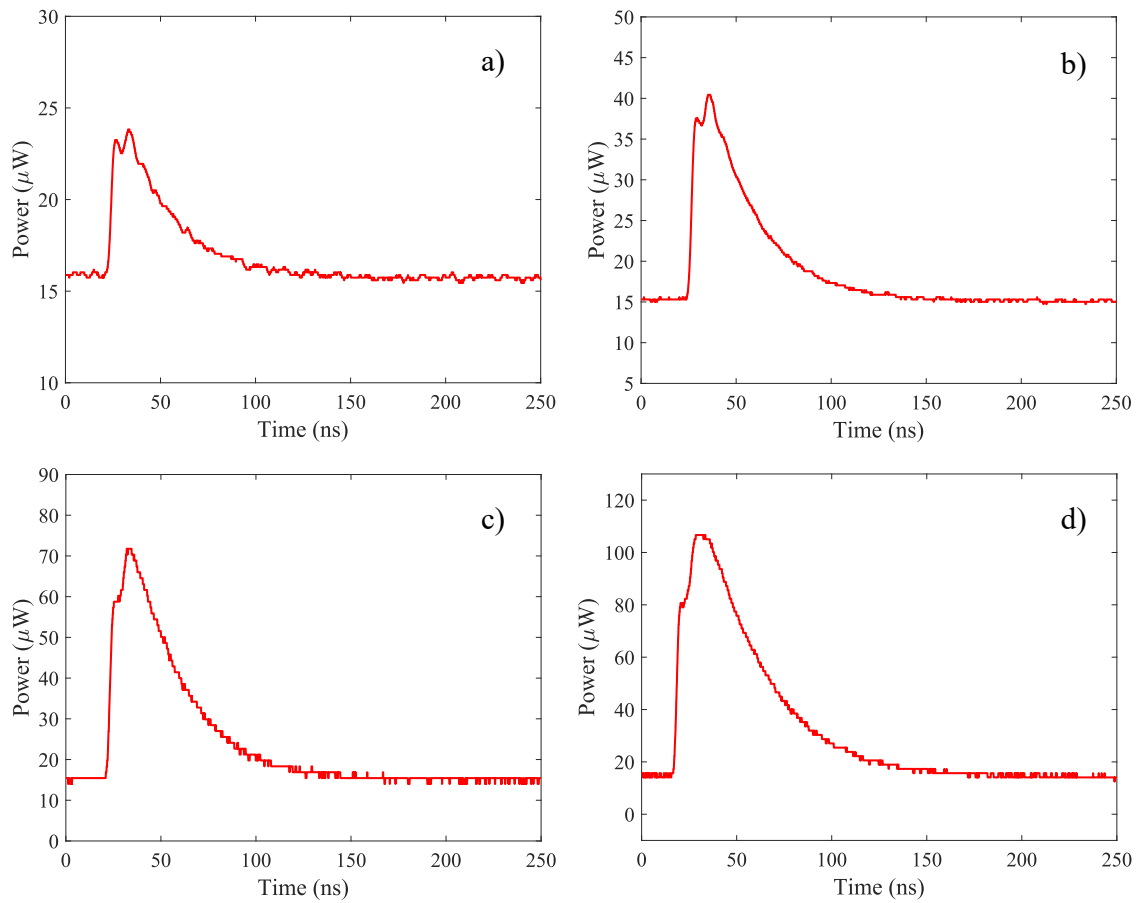


**Figure 4.15:** Evolution of the reflected pulse by the GaAs wafer for different excitation laser energies. a)  $E_L = 0.64 \text{ mJ}$ . b)  $E_L = 2.10 \text{ mJ}$ . c)  $E_L = 8.6 \text{ mJ}$ . d)  $E_L = 50.0 \text{ mJ}$ .

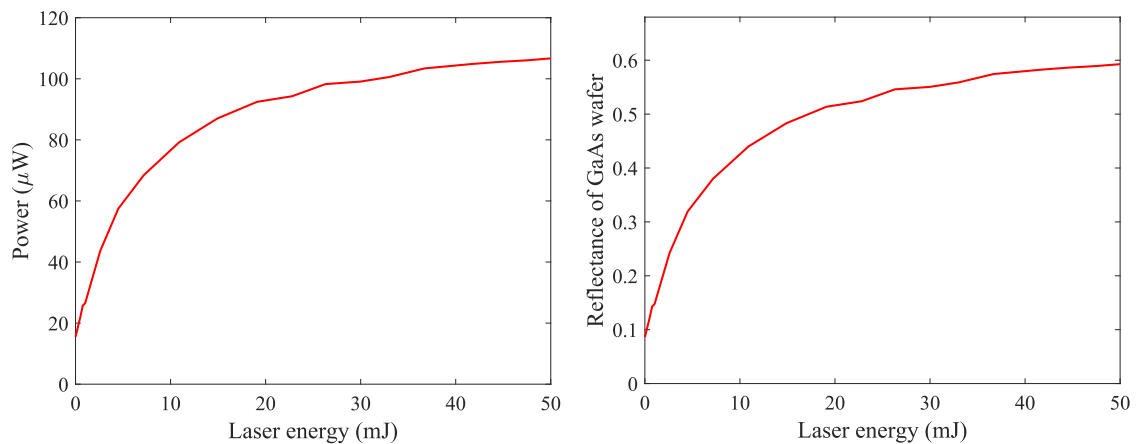


**Figure 4.16:** 100 GHz reflectance response by the GaAs wafer versus the excitation laser energy. Peak power of the reflected pulse (left). Equivalence of the peak power in reflected percentage (right).

### Rise and decay time of GaAs reflectance response

The preceding Fig. 4.15d) is visualized in Fig. 4.17 under two different time scales. Focusing first on Fig. 4.17a), the rise time is about  $t_{rs} = x_2 - x_1 \approx 12.5$  ns which is considerably less than the 57 ns of silicon. Moreover, a different pattern in the way how the curve ascends is observed. In particular, at around  $80 \mu\text{W}$  the reflectance level – and therefore the carrier concentration – remains constant for about 3 ns and then increases again until it reaches its maximum value.

On the other hand, according to Fig. 4.17b), the FWHM of the pulse is  $\sim 40$  ns which is around 225 times shorter than the  $9 \mu\text{s}$  of Si. Furthermore, it can be seen that once the excitation laser is off the pulse power decays – and in consequence the reflectance – in about  $t_{ds} = x_4 - x_3 \approx 111$  ns which is also much less than the  $29 \mu\text{s}$  of the silicon case. Overall, the shorter time values found in GaAs when compared with Si, obeys its direct band gap nature which leads to a shorter carrier lifetime (faster recombination process), as expected.

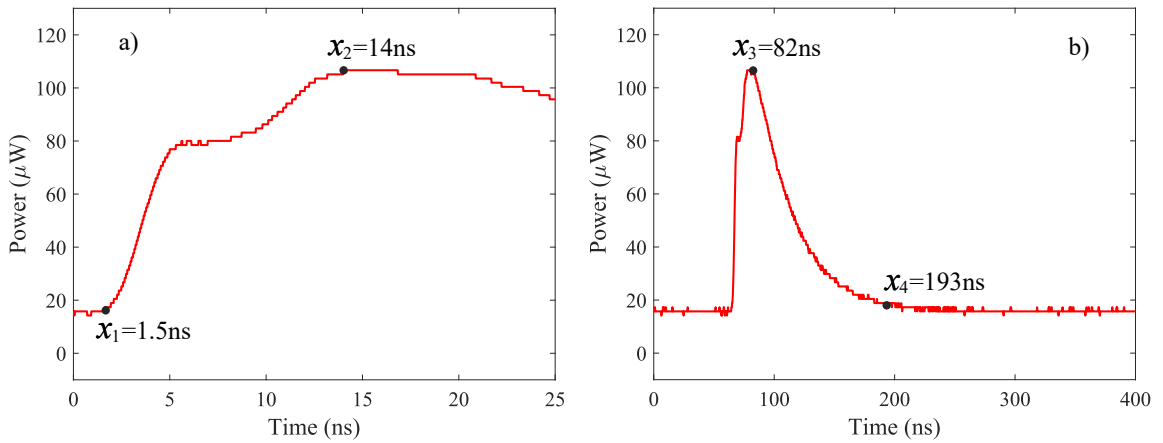


**Figure 4.17:** Reflected pulse by the GaAs wafer for a  $E_L=50$  mJ. a) Shorter time scale. b) Longer time scale.

### 4.8.3 Comments on the experimental results

The calculations in section 4.7.1 were based on assuming steady-state conditions with uniform laser illumination and a uniform carrier generation rate in the semiconductor (see section 4.5). Compared with those results, the maximum experimental reflectance achieved for both Si and GaAs was lower than estimated. The reasons might be due to the following factors, some of them interrelated, which could cause the uniformity

conditions not to be fulfilled.

- Irregularities in the uniformity of the laser beam intensity.
- The high reflectance observed at the semiconductor surface to the incident 532 nm excitation laser. This significantly reduces the effective illumination intensity on the semiconductor.
- Immobilized carriers trapped at lower energy states due to defects in the semiconductor [RBBA17]. This can lead to a lower optical efficiency of the carrier generation ( $\eta < 1$ ).
- Rapid carrier recombination because of impurities on the semiconductor surface. This generates a lower carrier concentration in the surface which exponentially increases across the thickness of the semiconductor. It should be pointed out that the impurity content of the semiconductors used in the experiments is unknown.
- The thickness and wedge angle of the wafer regarding the excitation laser [VDH<sup>+</sup>92].
- Diffusion of carriers throughout the wafer thickness. In the simulations, it was assumed a homogeneous distribution of carrier in the semiconductor which is not exactly the case because a huge concentration exists on the surface during the first micrometers and then diffusion occurs through a short distance (less than  $30 \mu\text{m}$ ).
- The shape and duration of the excitation laser pulse.

Regarding the last mentioned factor, the green graph in Fig. 4.18 corresponds to the excitation laser pulse. It can be seen that the energy of the pulse extends a little over 70 ns which alters considerably the results of Eqs. (4.7.4) and (4.7.6). This also explain why the rise time and decay time in both semiconductors are too long according to the literature. In particular, the red graph in Fig. 4.18 corresponds to the GaAs response of Fig. 4.17a) which is superposed to the excitation laser pulse. It is appreciated that during the big peak of the laser pulse the amplitude of the semiconductor response reaches  $\sim 0.17 \text{ V}$  and keeps there a few nanoseconds according to the carrier lifetime. Then, during the second little peak of the laser pulse, which happens at about  $t \approx 37 \text{ ns}$ , the amplitude of the semiconductor response increases to about  $\sim 0.24 \text{ V}$  due to an

increment of the carrier density. After that, the carriers start to recombine and the amplitude decreases. Additionally, the decay is also long due to the contribution of the carrier generated by the part of the laser pulse between  $37 < t < 70$  ns. In general, a similar scenario occurs in the case of silicon.

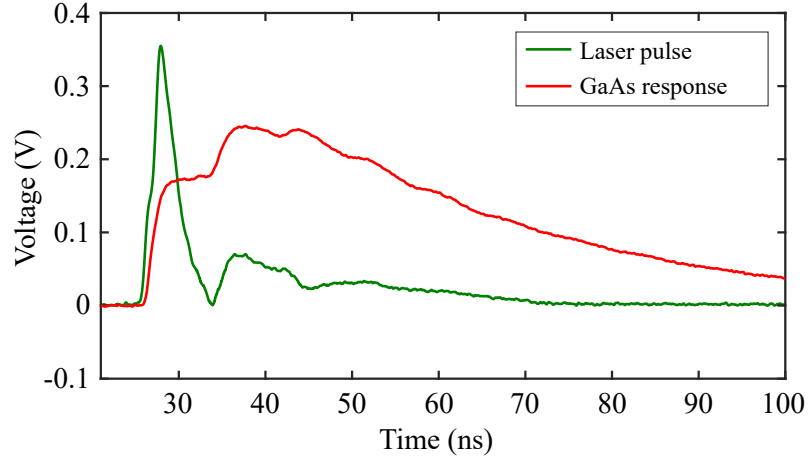


**Figure 4.18:** Excitation laser pulse (green) and GaAs response (red).

As a final remark, the standard 10-90% rise time and 90-10% decay time criteria for measuring  $t_{rs}$  and  $t_{ds}$  was not considered because it is essential to know as precisely as possible the moment of minimum and maximum reflectance of the SW in the compression procedure, as will be seen in the next chapter. However, taking into account the criteria, it is found for silicon that  $t_{rs} \sim 30$  ns and  $t_{ds} \sim 20$   $\mu$ s, and similarly for GaAs  $t_{rs} \sim 9$  ns and  $t_{ds} \sim 60$  ns.



---

# Chapter 5

## 100 GHz radiation compression

### 5.1 Introduction

The bow-tie enhancement cavity together with the semiconductor switch operation presented in the preceding chapters will enable to achieve the main objective of this thesis. This involves generating THz pulses by an experimental compression procedure from an original 100 GHz continuous-wave radiation to a higher power compressed pulse with the same frequency, and whose duration is around the nanosecond regime.

This chapter presents the experimental results of the THz compression system. Specifically, the accumulated power inside the resonant cavity will be extracted out in the form of a short pulse by implementing the laser-driven semiconductor switch principle on a silicon and gallium arsenide wafer, respectively. It will be seen that the characteristics of the extracted pulse depends on the energy of the excitation laser pulse, the cavity round trip time, the intensity of the cavity circulating light, and the switching response (rise time and fall time) and recombination time of the semiconductor.

### 5.2 Experimental setup

Fig. 5.1 shows the 100 GHz radiation compression setup. A Gaussian beam generated by the 100 GHz CW source is adapted through a mirror and lens arrangement to match the  $\text{TEM}_{00}$  mode of the bow-tie optical cavity. When the cavity is tuned at resonance, the intensity of cavity input light is enhanced a certain number of times expressed through the enhancement factor parameter  $\mathcal{E}$ . Subsequently, a SW placed at  $\phi = 68^\circ$  is optically excited by a laser pulse centered at 532 nm, with  $\sim 7$  ns FWHM of duration,

10 Hz of repetition rate, 50 mJ of maximum energy, and a beam diameter of 5 cm. This excitation induces a momentary reflectance from the semiconductor surface. As a result, a compressed 100 GHz radiation (short pulse) is extracted from the cavity.

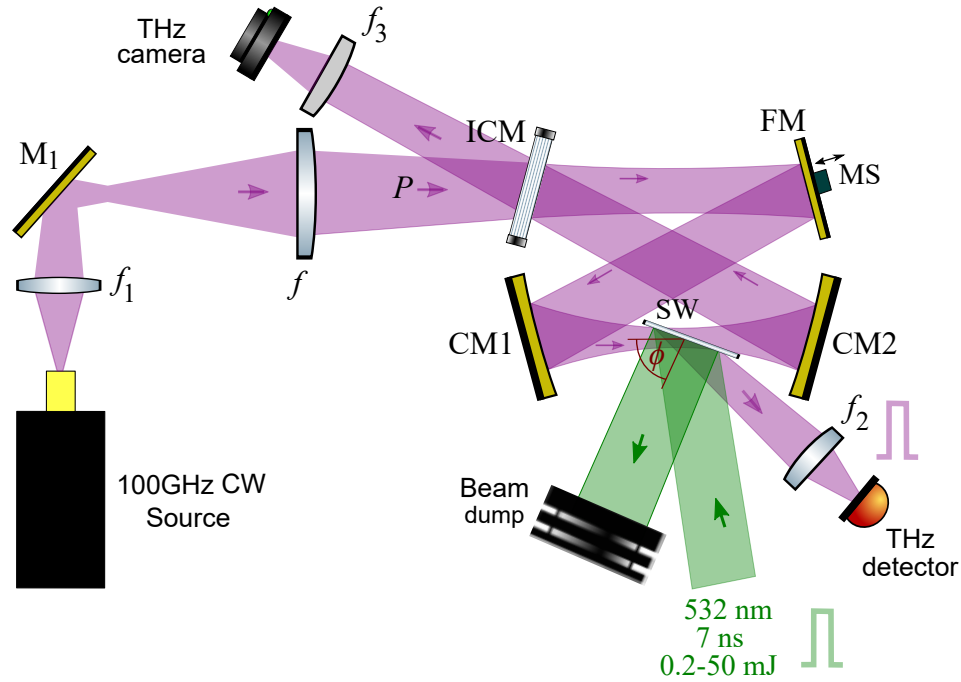


**Figure 5.1:** 100 GHz radiation compression setup.

### 5.3 Pulse compression by using Si SW

In order to obtain the following experimental results, the excitation laser was gradually increased from 0.2 to 50 mJ for a constant cavity input light power of  $145 \mu\text{W}$ , an enhancement factor of about  $\mathcal{E} \approx 17.5$ , and in consequence a cavity circulating power of  $\sim 2.5 \text{ mW}$ .

Fig. 5.2 illustrates four specific cases of the extracted pulse. In each of them, with the cavity at resonance, at time 0 s the power reflected by the silicon SW is about  $85 \mu\text{W}$ . This value is maintained until the excitation laser illuminates the wafer. At that instant, the carrier concentration in the semiconductor rapidly begins to grow which increases the percentage of reflection  $R_p$ . This is manifested through the generated pulse present in the extracted signal. According to the sequence of the graphs, as the laser energy increases, the amplitude of the pulse also rises, but the way it decays varies due to the number of carriers (level of reflectivity) photogenerated by the laser. For instance,

in Fig. 5.2a) the pulse decays roughly exponentially, while in the other cases of larger laser energies the decay becomes oscillatory, releasing part of the energy accumulated in the cavity in each period of oscillation. Regardless, most of the cavity light discharges in about  $\sim 100$  ns. Besides, once the semiconductor reaches its photoconductive state, i.e., while the light is being extracted from the resonator, the vast majority of the input 100 GHz radiation to the cavity is no longer coupled to it but is now mostly reflected by the ICM. This is caused by the increase of the cavity losses attributed to the high reflectance in the SW. Therefore, the accumulated light that circulates inside the resonator corresponds to a pulse of  $\sim 3$  ns duration, which is equivalent to the cavity round-trip time.

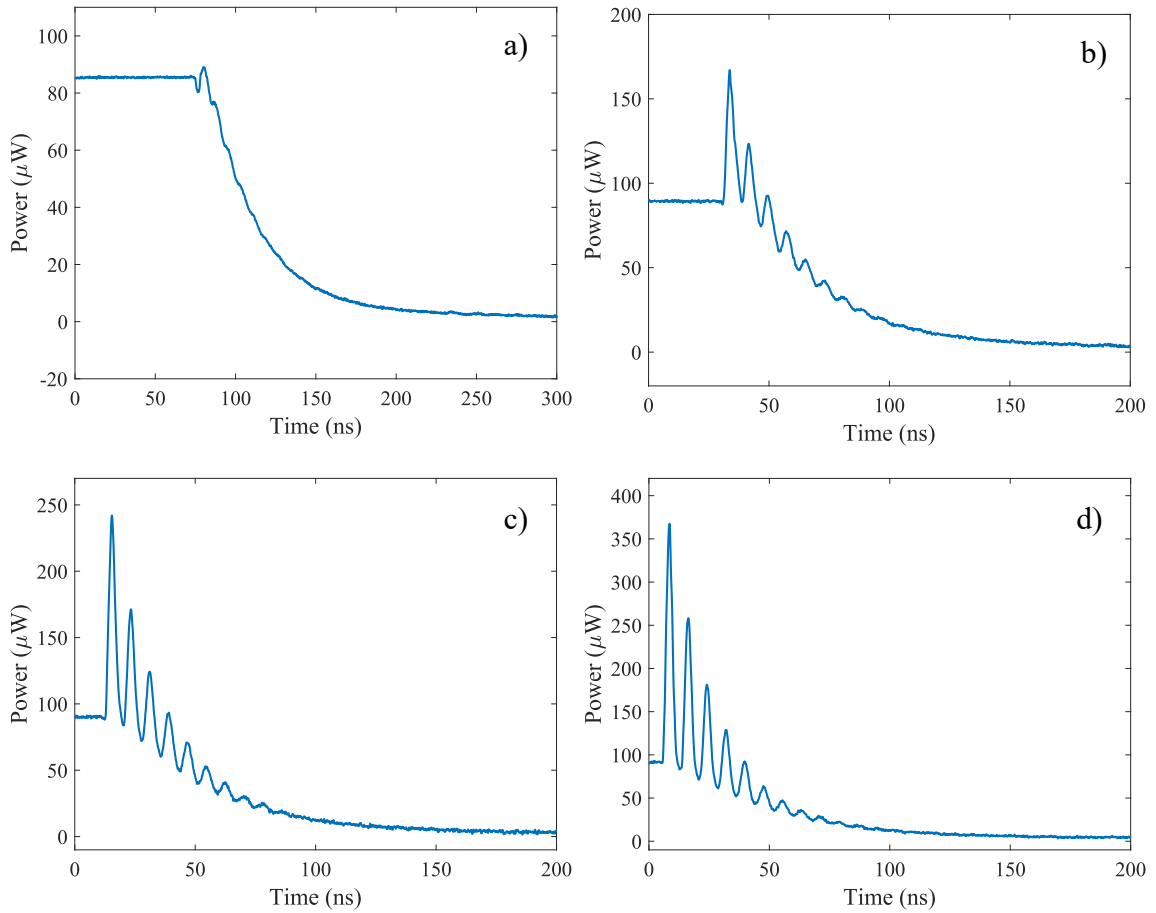


**Figure 5.2:** Extracted pulse from the cavity at resonance under an excitation laser energy of: a)  $E_L=0.25$  mJ, b)  $E_L=2.1$  mJ, c)  $E_L=8.4$  mJ and d)  $E_L=50$  mJ.

The plot in Fig. 5.3 illustrates the extracted pulse of Fig. 5.2d) with a time scale increased to the millisecond regime. Apparently, carriers induce some losses in the

semiconductor. Then, as the carriers progressively disappear through the recombination process, the transmission loss in the semiconductor is reduced and the cavity gradually recharges. This causes the cavity to take about  $500 \mu\text{s}$  to fully recharge.

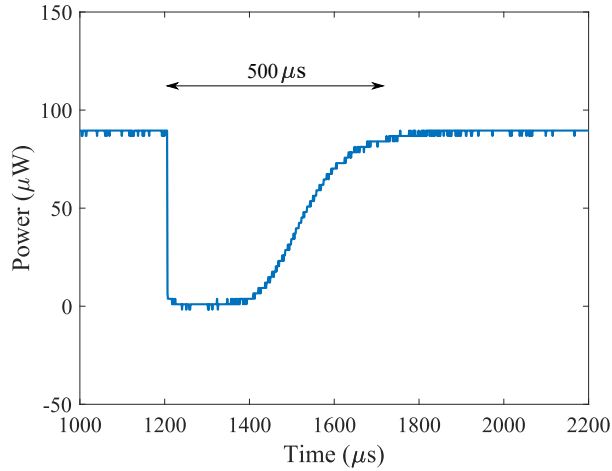


**Figure 5.3:** Longer time scale of the extracted pulse under an excitation laser energy of 50 mJ. The cavity recharge time is about  $500 \mu\text{s}$ .

### 5.3.1 Discussion of the extracted pulse

As shown in chapter 4, as  $E_L$  increases the carrier concentration in the semiconductor (and in consequence the reflectivity) also increases. This explains why in the graphs of Fig. 5.2 the higher the laser energy, the greater the amount of light extracted from the cavity. Under this concept, Fig. 5.2d) is the one with the best results. To explain in general terms the meaning of the oscillations and the shape of the extracted pulse, Fig. 5.2d) is shown again in Fig. 5.4a), but under a shorter time scale. According to Fig. 5.4a), four main sub-pulses (oscillations) account for most of the extracted energy, denoted as *I*, *II*, *III*, and *IV*, respectively. Each oscillation has a period of about  $6 \sim 7 \text{ ns}$ , which corresponds to approximately two cavity round-trip times. This implies that the majority of the extraction process is accomplished in about  $t_z \approx 28 \text{ ns}$  (sum of the four periods), or, in other words, most of the energy of the 3 ns circulating pulse is discharged in about 9 to 10 round trips in the cavity. Furthermore, it can be seen that the minimum and maximum points are labeled with the letters from *a* to *i*. At each of these points, the reflectivity of the semiconductor has a well-defined value which is dependent on the current level of the photoconductive state associated with the number of carriers. To estimate this value, Fig. 5.4b) depicts the foregoing Fig. 4.14a) with its equivalent letter labeled points wherein  $x_2$  would be the moment of maximum induced reflectivity in the semiconductor which is  $R_p \approx 0.67$  (see Fig. 4.13). Table 5.1

shows the corresponding percentage of reflection reached by the semiconductor at each of these points.

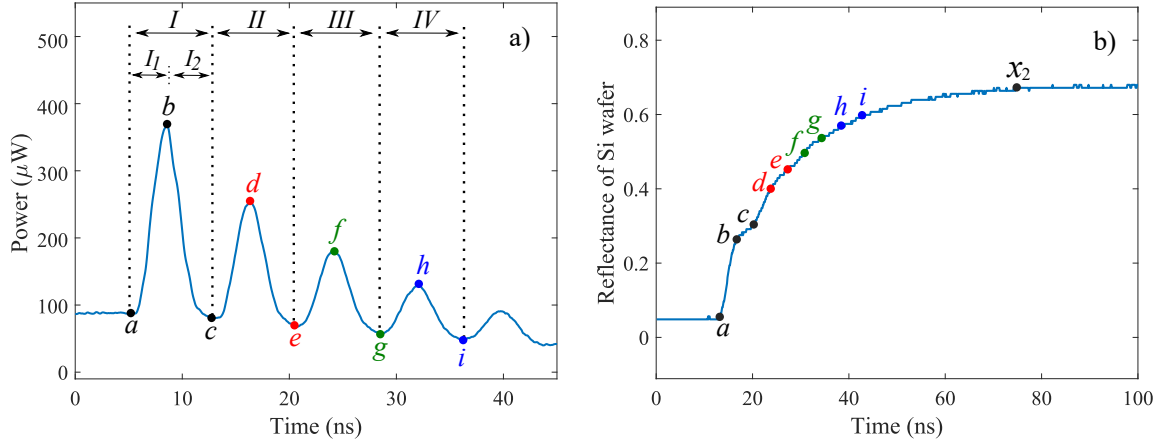


**Figure 5.4:** a) Extracted pulse under a  $E_L=50$  mJ. b) Rise time of the reflected signal by the Si wafer with the equivalent letter labeled points of figure a).

**Table 5.1:** Percentage of reflection reached by the Si wafer at each of the letter labeled points of Fig. 5.4b).

Curve location point	Percentage of reflection (%)
<i>a</i>	3.00
<i>b</i>	22.0
<i>c</i>	26.4
<i>d</i>	37.0
<i>e</i>	42.3
<i>f</i>	47.6
<i>g</i>	52.0
<i>h</i>	55.5
<i>i</i>	58.1

Focusing on period *I* of Fig. 5.4a), during the rising half-cycle  $I_1$  ( $0 < t_z < 3 \sim 4$  ns) the semiconductor gradually increases its reflectivity as the carrier concentration rises, resulting in a progressive increment of the extracted signal and a decrease around the same rate of the circulating pulse transmitted through the SW. According to Table 5.1, the semiconductor at point *b* has achieved around 22% of reflectivity. A schematic representation of the step  $I_1$  is visualized in Fig. 5.5.

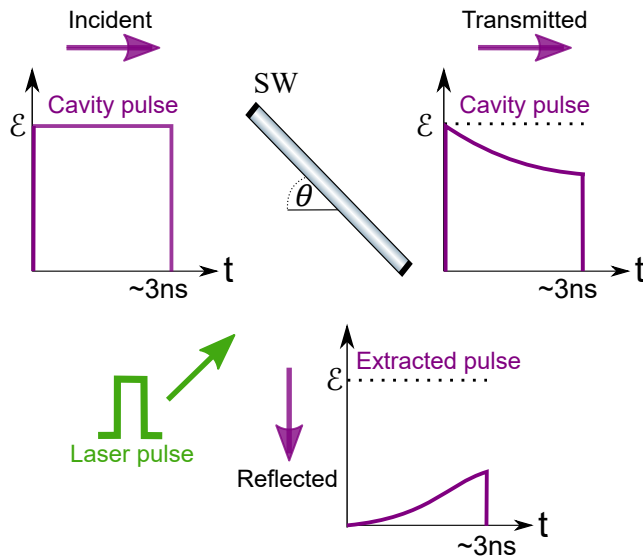


**Figure 5.5:** Schematic representation of the rising half-cycle  $I_1$  (not to scale) in the extraction process.

Next, in the falling half-cycle  $I_2$  ( $3 \sim 4 \text{ ns} < t_z < 7 \text{ ns}$ ) the circulating pulse takes its second round trip. At the onset of  $I_2$ , the front part of the circulating pulse – the one with the highest amplitude – starts being reflected and then followed by the rest of the pulse whose amplitude was gradually reduced during  $I_1$ . This explains why the amplitude of the extracted signal decreases throughout  $I_2$  despite the fact that the reflectivity is still increasing. Looking again at Table 5.1, about 26% of reflectivity is reached by the SW at point *c*. Fig. 5.6 illustrates a schematic diagram of the step  $I_2$ .

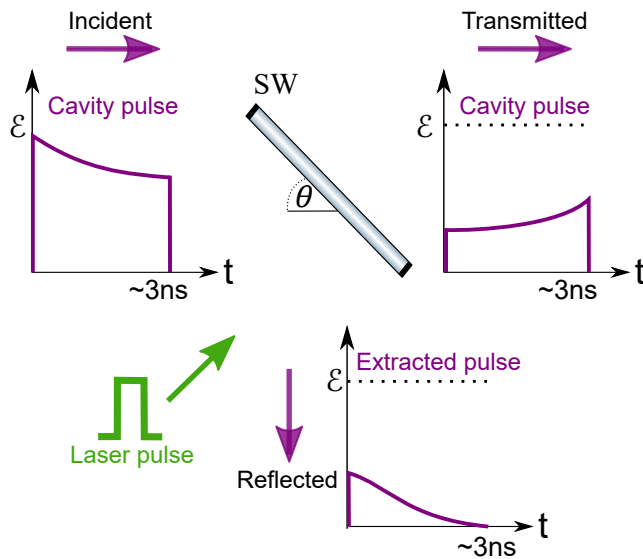


**Figure 5.6:** Schematic representation of the falling half-cycle  $I_2$  (not to scale) in the extraction process.

Finally, during  $II$  ( $7 \text{ ns} < t_z < 13 \sim 14 \text{ ns}$ ),  $III$  ( $14 \text{ ns} < t_z < 20 \sim 21 \text{ ns}$ ) and  $IV$

( $21 \text{ ns} < t_z < 28 \text{ ns}$ ), a procedure similar to *I* is performed with the remaining energy in the cavity after each process. It is important to mention that  $I+II+III+IV$  is carried out in  $t_z \sim 28 \text{ ns}$  which is about half of the time taken by the semiconductor to reach its maximum reflectivity ( $\sim 57 \text{ ns}$ ). Additionally, the losses attributed to the mirrors and the absorption in the SW contribute in parallel to the decay of the radiation stored in the cavity.

### 5.3.2 Efficiency of the compression process

Fig. 5.7 shows a summary of the results of the extraction process by using a Si wafer as an optical switch. On a), the plot displays the value of the highest peak power of the extracted pulse versus the amount of laser energy used for its generation. On b), knowing that the cavity circulating power is  $\sim 2.5 \text{ mW}$  before the extraction, the same plot displays the value equivalent in extracted percentage.

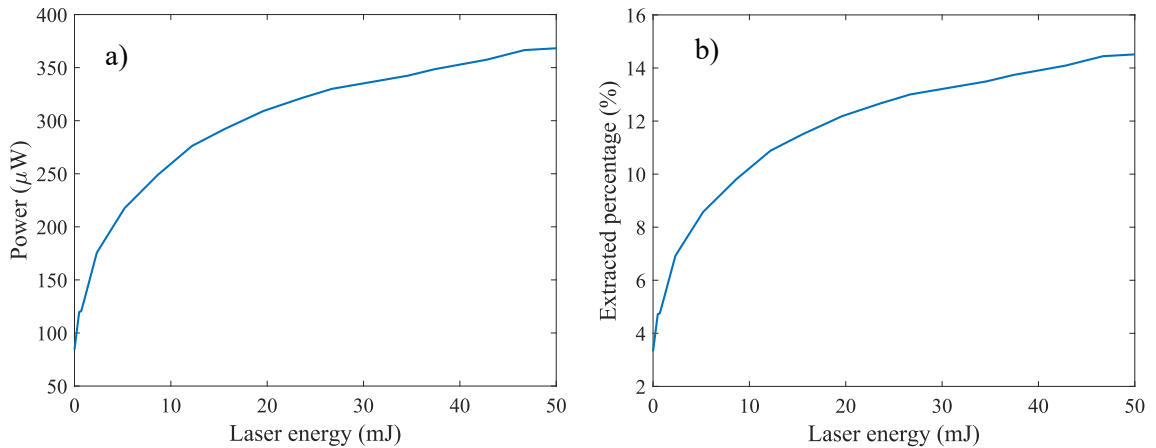


**Figure 5.7:** Summary with the extracted values from the cavity by using a Si SW as an optical switch: highest peak power of the reflected 100 GHz pulse (a) and its equivalence in percentage of extraction (b).

In general, the curves do not reach saturation. This means that the carrier concentration (and hence, the degree of reflectivity) in the semiconductor continues to grow even over  $E_L=50 \text{ mJ}$ . Furthermore, since the highest peak power happens during the first  $3 \sim 4 \text{ ns}$ , the rate of carrier generation is fast enough to reach throughout this span only about 22% of reflectance. Consequently, in the case of maximum energy of the excitation laser, the point  $b \approx 370 \mu\text{W}$  in Fig. 5.4a) is equivalent to approximately 14.8% of the cavity circulating power, corresponding to 2.5 times the cavity input power. However, by taking into account the sum of the peak power locations

$b+d+f+h \approx 940 \mu W$  (all of which are above the minimum reflection of  $\sim 85 \mu W$  that occurs without the presence of  $E_L$ ) the extraction percentage rises to about  $\sim 38\%$  of the total cavity circulating power, corresponding to  $\sim 6.5$  times the cavity input power. This relatively low level of efficiency is not surprising since the semiconductor practically reaches its maximum reflectance once the light in the cavity has already discharged.

The previous results conclude that the magnitude and shape of the extracted pulse are subject to four main factors: the energy and duration of the excitation laser pulse, the cavity round-trip time, the power of the cavity circulating light (i.e, the enhancement factor), and the carrier generation-recombination time associated the characteristics of the semiconductor. The following section will show how the efficiency varies considerably by changing the nature of the semiconductor.

## 5.4 Pulse compression by using GaAs SW

The results shown in this section were obtained after mounting the experimental setup of Fig. 5.1. Nevertheless, on this occasion, without the presence of the excitation laser and with the GaAs wafer placed at  $\phi = 68^\circ$ , the measured reflectivity is about  $R_p=0.08 \sim 0.09$ . This leads to a cavity enhancement factor of around 6.5 which multiplied by the cavity input power  $P = 145 \mu W$  provides an approximate circulating power of around  $942 \mu W$ .

Along with the last observations, the extracted pulses at four specific laser energy values are depicted in Fig. 5.8. Overall, the response follows a similar principle to that seen so far for the Si case: the peak power of the extracted pulse increments with the laser energy, and the decay changes from exponential to oscillatory as the energy increases, where each period of oscillation lasts about  $6 \sim 7$  ns which is approximately equivalent to twice the traveling time of the light in the cavity. This identical behavior is because the cavity dimensions remain the same, whereby the circulating internal pulse maintains its  $\sim 3$  ns duration, discharging on each round trip, regardless of the material of the semiconductor. However, a noticeable difference can be observed thanks to the faster recombination time of GaAs: on this occasion, the light in the cavity does not discharge completely and starts to recharge rapidly around  $60 \sim 70$  ns after the maximum peak power has occurred.



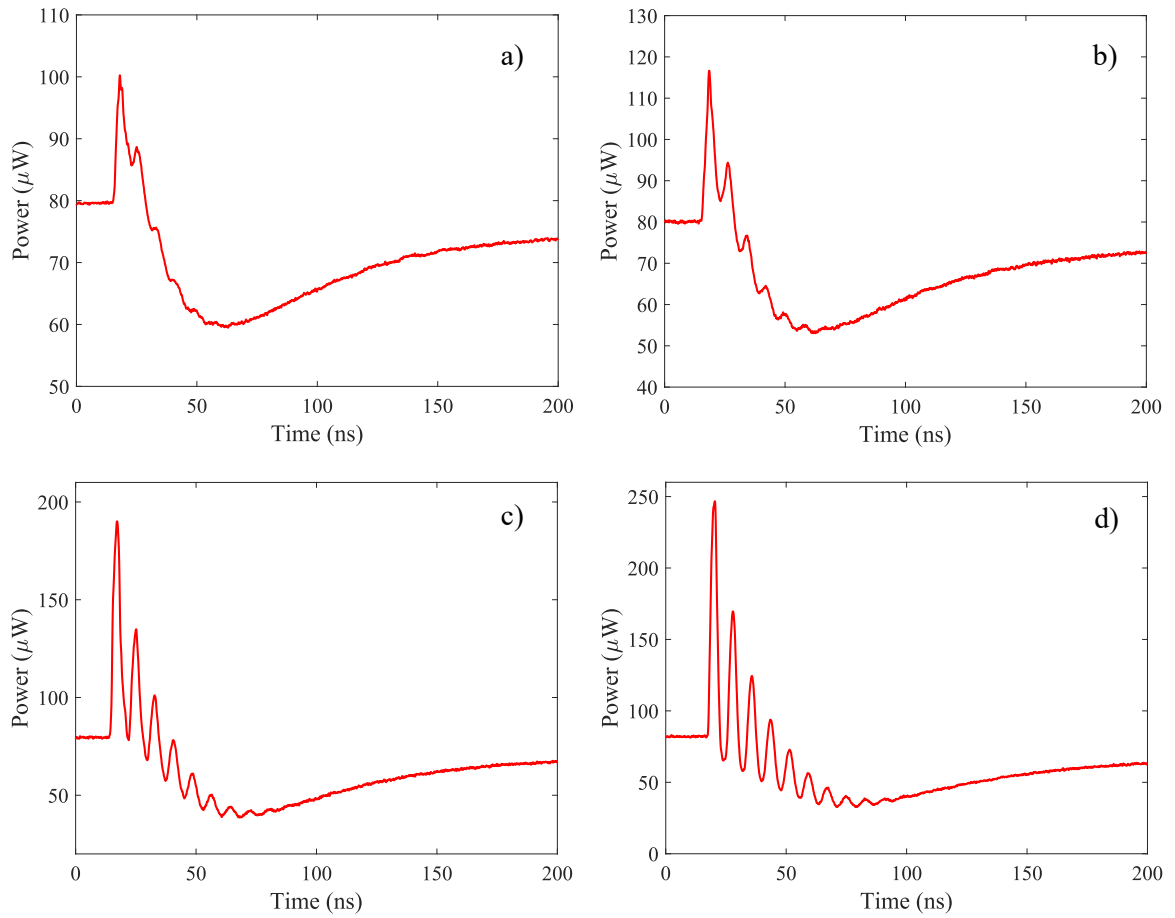


**Figure 5.8:** Extracted pulse from the cavity at resonance under an excitation laser energy of: a)  $E_L=0.52$  mJ; b)  $E_L=1.0$  mJ; c)  $E_L=7.2$  mJ and d)  $E_L=50$  mJ.

Fig. 5.9 shows the extracted pulse of Fig. 5.8d) with a time scale increased to the microsecond regime. As in the case of silicon, carriers in the semiconductor induce some losses. Then, as the carriers progressively disappear through the recombination process, the transmission loss in the semiconductor is reduced and the cavity gradually recharges. In particular, in Fig. 5.9a), once the signal reaches the point of minimum power, the cavity begins to charge rapidly for about 100 ns. Then, following the curve of Fig. 5.9b), the charging rate slows down considerably over a few tens of  $\mu\text{s}$ . Finally, the cavity takes about 170  $\mu\text{s}$  to fully recharge. Regardless, for both Si and GaAs SW cases, the magnitude of this parameter is not as relevant in the extraction routine itself since the laser pulse has a repetition rate of 10 Hz. This implies that the time between the laser pulses is around 100 ms, much longer than the cavity recharging time.

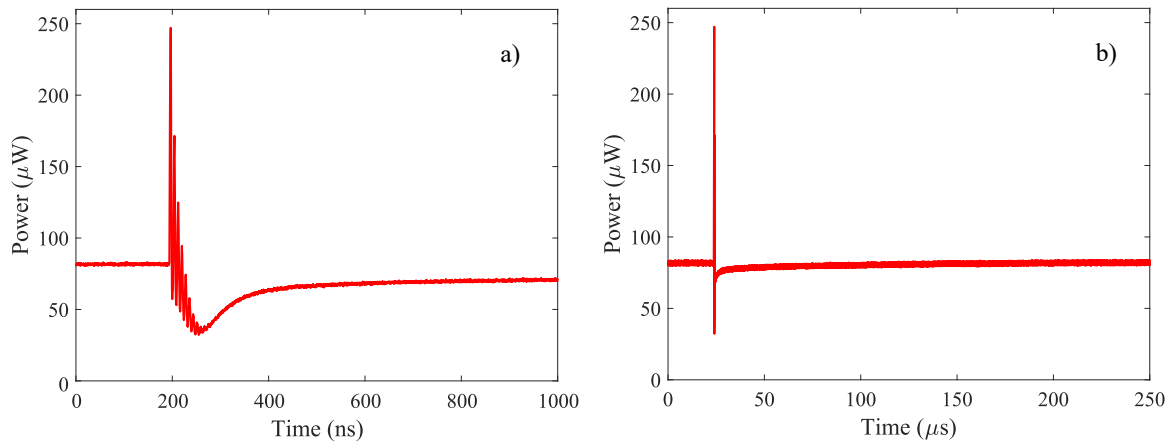


**Figure 5.9:** The extracted pulse of Fig. 5.8d) with longer time scales. The cavity recharging time is about  $170 \mu\text{s}$ .

### 5.4.1 Efficiency of the extracted pulse

In order to understand the evolution over time of the extracted pulse regarding the SW reflectivity, Fig. 5.10 shows on a) the foregoing Fig. 5.8d) and on b) the previous Fig. 4.17a), both with letter labeled points. Consequently, Table 5.2 provides the level of reflectance at each of the points. It is worth mentioning that since the way the circulating light is extracted from the cavity is the same for both Si and GaAs, the step-by-step discussion of the extracted pulse for the Si case described in section 5.3.1 is also applicable for the pulse obtained using the GaAs wafer, therefore it will not be explained again.

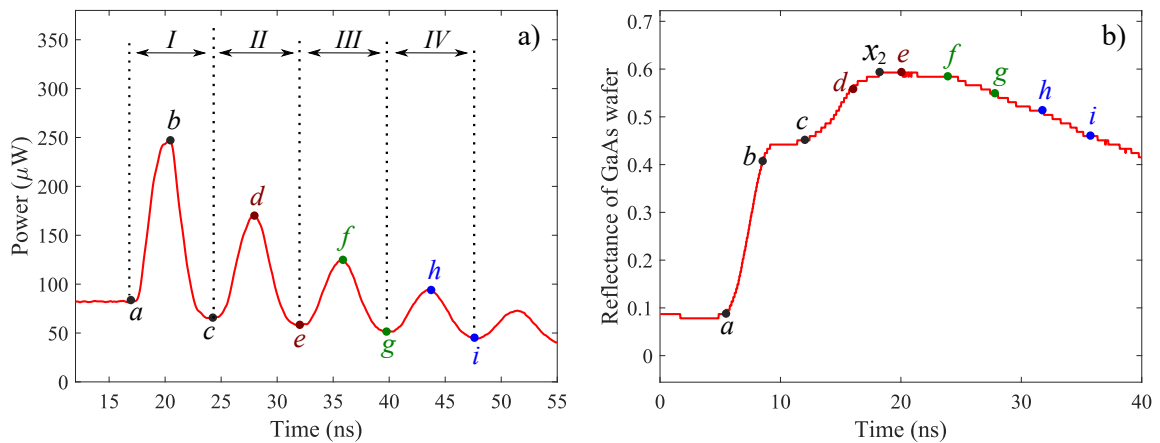


**Figure 5.10:** a) Extracted pulse under a  $E_L=50 \text{ mJ}$ . b) Rise time of the reflected signal by the GaAs wafer with the equivalent letter labeled points of figure a).

**Table 5.2:** Percentage of reflection reached by GaAs SW at each of the letter labeled points of Fig. 5.10b).

Curve location point	Percentage of reflection (%)
<i>a</i>	8.20
<i>b</i>	37.2
<i>c</i>	42.4
<i>d</i>	54.8
<i>e</i>	59.0
<i>f</i>	57.9
<i>g</i>	53.8
<i>h</i>	49.6
<i>i</i>	43.4

Focusing on Fig. 5.10a), the sum of periods  $I + II + III + IV$  is about  $t_z \approx 28$  ns. knowing that the cavity circulating power is about  $\sim 942 \mu W$ , therefore at point  $b$  ( $t_z=3 \sim 4$  ns) with around 37% of the reflectivity in the SW, a peak power of  $\sim 247 \mu W$  is achieved, corresponding to  $\sim 26\%$  of the maximum cavity circulating power. This is roughly equivalent to 1.7 times the cavity input power. Similarly, with  $R_p \approx 54\%$  at  $d$  ( $t_z \approx 11$  ns),  $R_p \approx 57\%$  at  $f$  ( $t_z \approx 18$  ns), and  $R_p \approx 49\%$  at  $h$  ( $t_z \approx 24$  ns), considering the addition of peak powers  $b+d+f+h$ , the extracted power rises to  $\sim 635 \mu W$ , which is equivalent to  $\sim 67\%$  of the maximum cavity circulating power and to  $\sim 4.4$  times the cavity input power.

Eventually, Fig. 5.11 presents a summary with the results of the extraction process by using GaAs as an optical switch. On a), the curve displays the value of the highest peak power of the extracted pulse versus the amount of laser energy used for its generation. On b), there is the same plot but with its equivalent in extracted percentage. As in the case of Si, the curves do not reach saturation either. However, on this occasion, the slope becomes less steep as the laser energy increases, implying that GaAs appears to achieve saturation at a lower excitation energy level than Si, which is consistent with its shorter carrier generation time.

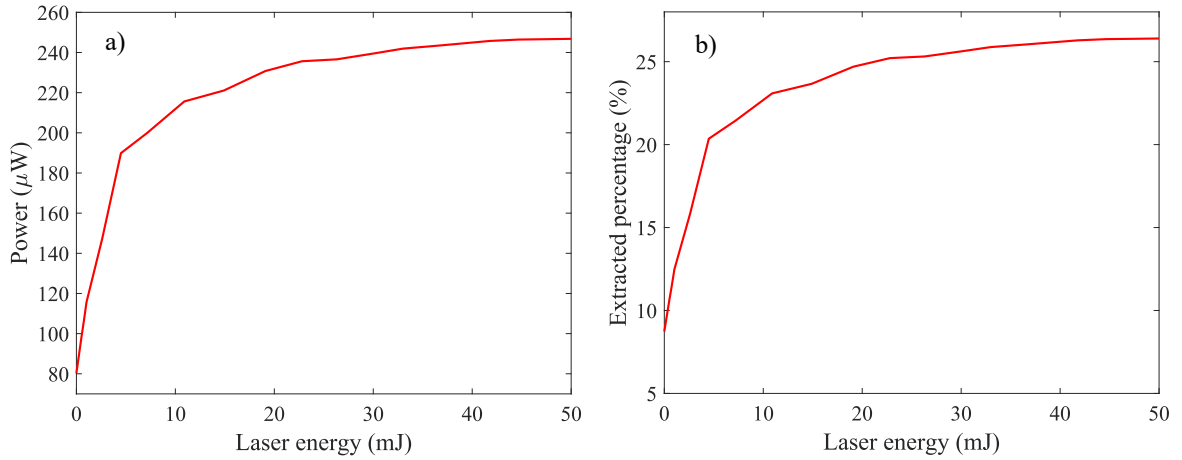


**Figure 5.11:** Summary of the extracted values from the cavity by using GaAs SW as an optical switch: highest peak power of the reflected 100 GHz pulse (a) and its equivalence in percentage of extraction (b).

## 5.5 Final remarks

It is not surprising that GaAs had a better performance than Si in the extraction process. Its faster switching response achieves the maximum reflectance after  $\sim 13$  ns of interacting with the laser. However, under the current design, the ideal scenario would be to achieve the maximum reflectance in around  $3 \sim 4$  ns, i.e., within the first round trip of the cavity circulating pulse. Thus, most of the extracted energy would be concentrated along the period  $I$ . In the same vein, it would be ideal to reach the maximum reflectance before the laser pulse begins to decay. This would allow the complete fulfillment of the steady-state conditions in the generation-recombination process. Unfortunately, as was shown throughout the development of this thesis, the unexpected longer response of both semiconductors due to probably the shape of the laser pulse (see Fig. 4.18) and the inherent characteristics acquired by the semiconductors during their fabrication made not possible such a situation.

The nature found in the extracted pulse delineates the methodology that should be applied to optimize future similar designs, in which the length of the cavity should ideally be set according to the response speed of the semiconductor. This also involves a decrease in the duration of the laser pulse, which should be less than  $1/10$ th of the cavity round-trip time. As a result, by having a thin short excitation laser pulse, the reflective response of both semiconductors would also be much sharper, and in consequence, the quality of the extracted pulse would also improve drastically.

---

## Chapter 6

# Conclusions and Outlook

Along with this thesis, a new THz pulse compression system was presented and developed. To accomplish it, two fundamental objectives were achieved:

1. A 900 mm-length bow-tie enhancement cavity resonant for an input Gaussian beam centered at 100 GHz of frequency (3 mm wavelength in the space domain) was designed and implemented (sections 3.2 and 3.4.2) by following the fundamentals of optical resonators. For this purpose, a Bragg reflector as the cavity input coupling mirror (ICM) composed of a multilayer structure designed with the transfer matrix technique was fabricated (section 3.3). The number of layers and type of material used, in the form of wafers, allowed the control of the intensity of the cavity input light. Furthermore, a single-lens strategy to match the mode of the input Gaussian beam to the TEM<sub>00</sub> cavity mode was performed (section 3.4.1) which enabled to couple most of the input light into the cavity with just a small amount reflected by the ICM. This was manifested through the circulating spectrum obtained by scanning the cavity length, where pronounced intensity peaks around the resonant frequencies and small intensity peaks around high-order modes could be observed (Fig. 3.15). As a result, the ICM formed by three 1 mm-thick silicon wafers separated from each other by 1 mm of air led to the best cavity performance, achieving an experimental enhancement factor of around  $\mathcal{E} \approx 18$  out of a possible maximum one of  $\mathcal{E} \approx 20$  (Table 3.3), this maximum enhancement considered a perfect mode matching and cavity alignment. Under such a scenario and according to the cavity parameters, the measured transmittance of the ICM was  $T_I = 0.0475$ , and all the round-trip cavity losses, without including the ICM, were  $L = 0.05$ . Thereby, due to  $T_I < L$ , the designed cavity was a little under coupled

(section 3.4.3).

2. The laser-driven semiconductor switch (LDSS) method was experimentally developed and proven (section 4.8). Specifically, intrinsic Si and GaAs semiconductors were excited by a 532-nm, 7-ns laser pulse. As a consequence, both semiconductors became reflective to 100 GHz radiation, with a degree of reflectivity proportional to the laser energy. Particularly, for a maximum laser pulse energy of  $E_L=50$  mJ (laser energy density of  $2.5$  mJ/cm<sup>2</sup>), the reflected pulse by Si reached around  $R_p \approx 0.67$  of peak reflectance (Fig. 4.13), whereas GaAs reached a maximum of about  $R_p \approx 0.59$  (Fig. 4.16). However, the GaAs reflective response was considerably faster than the Si one. In particular, the pulse reflected by GaAs was  $\sim 40$  ns (FWHM) of width and  $12 \sim 13$  ns of rising time (Fig. 4.17). Instead, the reflected one by Si had a width of  $9 \mu\text{s}$  (FWHM) and a rising time of  $\sim 57$  ns (Fig. 4.14).

The THz pulse compression system involved joining and implementing the two fundamental objectives at the same time, i.e., the enhanced light in the cavity was extracted by employing the LDSS method applied on a semiconductor wafer placed inside the cavity. Specifically, the extraction process was performed continuously on each round-trip of the 3-ns duration circulating pulse in the cavity, and the amount of light extracted on each round-trip was dependent mainly on the reflectivity level reached by the semiconductor at that instant and the current remaining power in the cavity. Thus, most of the cavity circulating power was extracted within 9 to 10 round trips of the circulating pulse producing, in the end, an extracted pulse with a duration of about  $\sim 28$  ns distributed over four sub-pulses (oscillations), each with a period of around  $6 \sim 7$  ns (two cavity round-trips) and different amplitudes (Figs. 5.4 and 5.10).

In particular, for a cavity input light power of  $145 \mu\text{W}$  and a 532-nm, 7-ns, 50-mJ excitation laser pulse, the compression system was performed under two specific scenarios. First, by using an intrinsic Si wafer, for  $\mathcal{E} \approx 17.5$  and considering the sum of the peak power of the four sub-pulses, a maximum power of  $940 \mu\text{W}$  was extracted, corresponding to  $\sim 38\%$  of the cavity circulating power and equivalent to 6.5 times the cavity input power (section 5.3). Second, by using an intrinsic GaAs wafer, for  $\mathcal{E} \approx 6.5$  and considering again the sum of the peak power of the four sub-pulses, a maximum power of  $635 \mu\text{W}$  was extracted, corresponding to  $\sim 67\%$  of the cavity circulating power and equivalent to 4.4 times the cavity input power (section 5.4). These results demonstrated that the magnitude, shape and duration of the extracted

pulse were dependent on four main factors: the energy and duration of the excitation laser pulse, the cavity round-trip time (cavity length), the cavity enhancement factor and the switching speed and number of carriers of the semiconductor.

All things considered, the efficiency of the THz pulse compression system can be improved in three ways:

- (i) By decreasing the cavity losses. This can be done by using mirrors with a higher reflectivity ( $R_c$ ) and/or by using a semiconductor wafer under equilibrium conditions with a higher transmittance ( $T_s$ ) when monitoring the cavity circulating light. For example, for a  $R_c = 0.997$  and a  $T_s = 0.99$  the theoretical enhancement factor would increase to over 50 (see Eq. (3.4.5)). This would raise the circulating power and consequently, the peak power of the extracted pulse oscillations.
- (ii) By using a semiconductor with a faster switching speed, ideally with a maximum reflectivity reached in less than 4 ns. This would enable the extraction of most of the cavity energy on the first round trip, hence the power of the extracted pulse would be especially concentrated within the first main oscillation.
- (iii) By shortening the duration of the excitation laser pulse. This would allow the semiconductor to reach a maximum reflectivity in a shorter period of time, ideally in less than 1/10th of a cavity round-trip.
- (iv) Finally, since neither of the used semiconductors reached saturation, an increase in the energy density of the excitation laser pulse might also contribute to an increment of the extracted power.

### Thesis outlook

The performance and knowledge of the variables involved in the THz pulse compression system presented in this thesis allow focusing the research on two main future applications:

1. By using the current cavity design:
  - Implementing the LDSS method by using Si and GaAs wafers fabricated by other manufactures. This would enable the selection of semiconductors with the fastest switching responses.

- Implementing the LDSS method by shortening the duration of the excitation laser pulse. By having a short excitation laser pulse, the reflective response of both semiconductors would also be a sharper pulse, and in consequence, the quality of the extracted pulse by the compression system would also improve drastically.
2. Developing the THz pulse compression system with a bow-tie enhancement cavity resonant with the radiation emitted by a gyrotron source for high-power THz applications. So far, the megawatt gyrotron incident power to the LDSS experiments is limited to  $\sim 600$  kW due to reflections from the experimental setup into the gyrotron and losses along the optical path [KJS<sup>+</sup>19, OPS<sup>+</sup>20]. Under such a scenario, some of the best results obtained by the LDSS technique of shortening the 3- $\mu$ s, 110-GHz gyrotron pulses are 9 ns by using Si wafer and 24 ns by using GaAs wafer, with a peak reflected power of 410 kW and 485 kW, corresponding to 78 % and 92 % of reflectance for a gyrotron incident power of 525 kW, respectively [KJS<sup>+</sup>19]. These results were obtained by using a 230-mJ, 532-nm, 6-ns laser pulse. Assuming similar conditions, the compression system would allow the dealing with the 600 kW limit power and exceed the reflected peak power to a certain number of times. The efficiency of this peak power would depend on the cavity enhancement factor and on an appropriate relation between the SW switching response and the cavity length. For example, considering a cavity input peak power of 525 kW with  $\mathcal{E}=20$ , an extracted pulse of 9-ns duration, and 70 % of reflectance by the semiconductor switch, the energy of the extracted pulse would be theoretically around  $E = 0.70 \cdot 525 \text{ kW} \cdot 20 \cdot 9 \text{ ns} \approx 66 \text{ mJ}$ . In addition, the extracted pulse duration could be compressed (again) by implementing a second LDSS arrangement (dual-wafer system) shortening the duration even below 3 ns [KJS<sup>+</sup>19, HS96].



---

# Appendix A

## 100 GHz IMPATT diode source

The cavity input radiation is generated by a THz source model IMPATT-100-H/F made by Terasense Group Inc. Table A.1 presents the most relevant properties of this source.

**Table A.1:** IMPATT-100-H/F general characteristics

Parameter	Value
Emission mode	Continuous wave (CW)
Frequency emission	100 GHz
Linewidth	$\sim 1$ MHz
Beam emission	Gaussian distribution (vertical polarization)
Horn output	WR-10
Measured output power	$\sim 20$ mW
Modulation	5 V square wave (1 Hz – 10 kHz)
Dimensions	174 x 77 x 71 mm (with horn)
Weight	0.5 kg
Power supply	24 VDC

The operation principle of the 100 GHz source is based on IMPATT diode technology which is the abbreviation for Impact Ionization Avalanche Transit Time Diode. The IMPATT diode is a solid-state high-power PN junction semiconductor device used as an oscillator and amplifier in the microwave frequency spectrum whose range depends on

the material used for its fabrication (principally Si, GaAs, Ge, and InP). To achieve such a functioning mode, the operation of the diode under the reverse bias condition – that means a reverse bias voltage over the avalanche breakdown voltage of the IMPATT –, the effect of the high impact ionization avalanche and the effect of the transit time of the carriers throughout the diode length induces a negative dynamic resistance behavior in the semiconductor which produces a total  $180^\circ$  delay phase difference between the applied AC+DC reverse bias voltage and the generated current density in the diode. Eventually, this created current is induced into an external resonant circuit from which the microwave signal is produced [WB71].

To characterize the actual radiation emission of the source, the beam profile was measured at four distinct  $z$  positions far from the source using a single-pixel detector of the THz camera model Tera-1024 fabricated also by Terasense Group Inc. The beam was scanned and recorded in the x-y axes and in increments of 1.5 mm, which coincides with the size of the camera pixel. The reconstructed beam at each location can be seen in Fig. A.1. It should be pointed out that due to the noise and distortion induced by the excessively high reflection level between the front panel of the camera and the source, it was not possible to scan the beam at distances shorter than  $z=85$  mm.

On the other hand, according to the manufacturer, the radiation comes from the round horn of the source in a cone shape with a transverse Gaussian profile and a divergence angle of  $\theta = 9^\circ$ , approximately. Furthermore, the beam waist, right at the front of the horn, is around  $w_0 = 6$  mm. Employing this information in Eqs. (2.2.10) and (2.2.11), a simulation of the beam radius emitted by the source as a function of the  $z$  propagation axis is shown in the blue curve of Fig. A.2.

In parallel, the red curve in Fig. A.2 represents the actual beam radius emitted by the source. This curve was calculated as the average value between  $w_x$  and  $w_y$ , which were taken from the experimental results of Fig. A.1.

To conclude, the similitude of the graphs in Fig. A.2 corroborates the information provided by the manufacturer, verifying the Gaussian nature of the light emitted by the source.

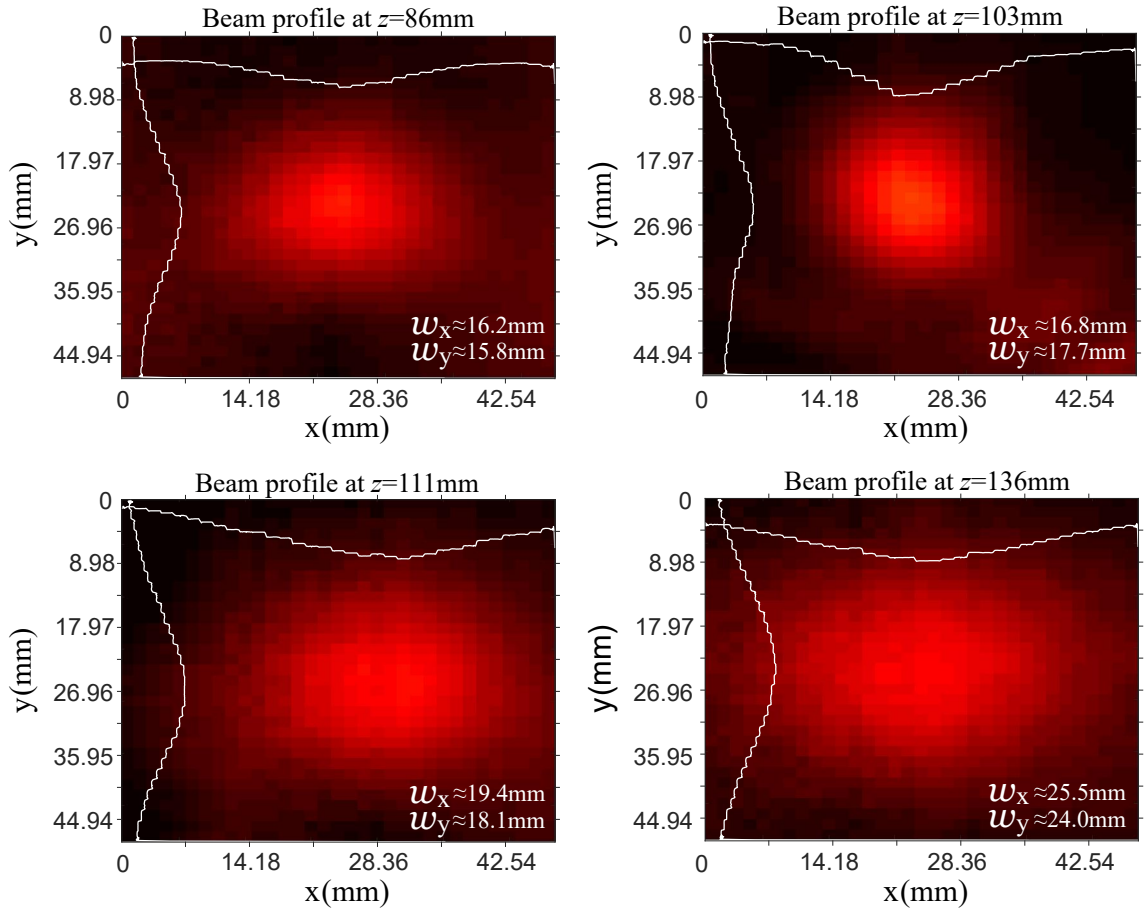


**Figure A.1:** Reconstruction of the emitted beam profile from the 100 GHz IMPATT diode source at different positions of  $z$ .

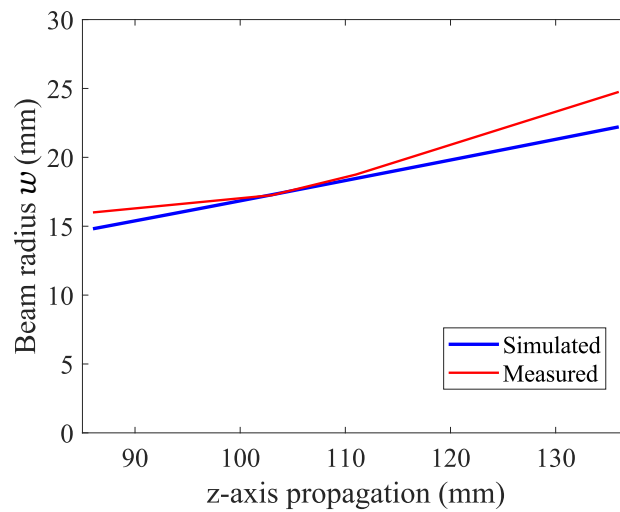


**Figure A.2:** Simulated (blue) and actual (red) beam propagation generated by the 100 GHz IMPATT diode source along the propagation axis  $z$ .



---

# Bibliography

- [AB77] R. M. A. Azzam and N. M. Bashara. *Ellipsometry and polarized light*. North-Holland Publishing Company, 1977.
- [ABB11] I. F. Almog, M. S. Bradley, and V. Bulović. *The Lorentz oscillator and its applications*. MIT Open Course, 2011.
- [AS04] Haim Abitan and Torben Skettrup. Laser resonators with several mirrors and lenses with the bow-tie laser resonator with compensation for astigmatism and thermal lens effects as an example. *Journal of Optics A: Pure and Applied Optics*, 7(1), 2004.
- [BAF<sup>+</sup>18] Johannes Bühler, Jonas Allerbeck, Gabriel Fitzky, Daniele Brida, and Alfred Leitenstorfer. Terahertz shockwaves generated by a precise subcycle cut of the electric field. *Optica*, 5(7), 2018.
- [Bee52] A. Beer. Bestimmung der absorption des rothen lichts in farbigen flüssigkeiten. *Annalen der Physik*, 162(78-88), 1852.
- [Bre18] Sven Breitskopf. *Energy Scaling by Stacking of Ultrashort Pulses in a Passive Enhancement Cavity*. Universität Jena, 2018.
- [BW03] Max Born and Emil Wolf. *Principles of Optics*. Cambridge University Press, 2003.
- [Car16] Henning Carstens. *Enhancement cavities for the generation of extreme ultraviolet and hard x-ray radiation*. Universität München, 2016.
- [CBB<sup>+</sup>13] E. Chiadroni, A. Bacci, M. Bellaveglia, M. Boscolo, M. Castellano, L. Cultrera, G. Di Pirro, M. Ferrario, L. Ficcadenti, D. Filippetto, G. Gatti, E. Pace, A. R. Rossi, C. Vaccarezza, L. Catani, A. Cianchi, B. Marchetti,

- A. Mostacci, L. Palumbo, C. Ronsivalle, A. Di Gaspare, M. Ortolani, A. Perucchi, P. Calvani, O. Limaj, D. Nicoletti, and S. Lupi. The sparac linear accelerator based terahertz source. *Applied Physics Letters*, 102(9):094101, 2013.
- [CCF<sup>+</sup>20] Enrica Chiadroni, Alessandro Cianchi, Massimo Ferrario, Andrea Mostacci, Riccardo Pompili, and Vladimir Shpakov. A versatile thz source from high-brightness electron beams: Generation and characterization. *Condensed Matter*, 5(2), 2020.
- [CCM<sup>+</sup>19] Luigi Consolino, Annamaria Campa, Davide Mazzotti, Miriam Serena Vitiello, Paolo De Natale, and Saverio Bartalini. Bow-tie cavity for terahertz radiation. *Photonics*, 6(1), 2019.
- [CHK<sup>+</sup>13] Henning Carstens, Simon Holzberger, Jan Kaster, Johannes Weitenberg, Volodymyr Pervak, Alexander Apolonski, Ernst Fill, Ferenc Krausz, and Ioachim Pupeza. Large-mode enhancement cavities. *Optics Express*, 21(9), 2013.
- [DCH<sup>+</sup>20] Umit Demirbas, Huseyin Cankaya, Yi Hua, Jelto Thesinga, Mikhail Pergament, and Franz X. Kärtner. 20-mj, sub-ps pulses at up to 70 w average power from a cryogenic yb:ylf regenerative amplifier. *Optics Express*, 28(2), 2020.
- [DCKS04] M. F. Doty, B. E. Cole, B. T. King, and M. S. Sherwin. Wavelength-specific laser-activated switches for improved contrast ratio in generation of short thz pulses. *Review of Scientific Instruments*, 75(9), 2004.
- [DFDB<sup>+</sup>16a] Massimo Dal Forno, Valery Dolgashev, Gordon Bowden, Christine Clarke, Mark Hogan, Doug McCormick, Alexander Novokhatski, Brendan O’Shea, Bruno Spataro, Stephen Weathersby, and Sami G. Tantawi. rf breakdown measurements in electron beam driven 200 ghz copper andcopper-silver accelerating structures. *American Physical Society*, 19(111301), 2016.
- [DFDB<sup>+</sup>16b] Massimo Dal Forno, Valery Dolgashev, Gordon Bowden, Christine Clarke, Mark Hogan, Doug McCormick, Alexander Novokhatski, Bruno Spataro, Stephen Weathersby, and Sami G. Tantawi. rf breakdown tests

- of mm-wave metallic accelerating structures. *American Physical Society*, 19(011301), 2016.
- [DLI14] Martina De Laurentis and Andrea Irace. Optical measurement techniques of recombination lifetime based on the free carriers absorption effect. *Journal of Solid State Physics*, 2014(ID 291469), 2014.
- [Dre01] M. S. Dresselhaus. *Solid State Physics Part II, Optical Properties of Solids*. MIT Lecture Notes, 2001.
- [ECC14] Mohamed Eldlio, Franklin Che, and Michael Cada. *Drude-Lorentz Model of Semiconductor Optical Plasmons*. Springer, 2014.
- [FLE71] G. E. Francois, F. M. Libreht, and J. J. Engelen. Mode matching with a single thin lens. *Applied Optics*, 10(5), 1971.
- [FOL<sup>+</sup>14] J. A. Fülöp, Z. Ollmann, Cs. Lombosi, C. Skrobol, S. Klingebiel, L. Pálfalvi, F. Krausz, S. Karsch, and J. Hebling. Efficient generation of thz pulses with 0.4 mj energy. *Opt. Express*, 22(17):20155–20163, Aug 2014.
- [Gru16] Marius Grundmann. *The Physics of Semiconductors*. Springer, 2016.
- [HAKK02] János Hebling, Gábor Almási, Ida Z. Kozma, and Jürgen Kuhl. Velocity matching by pulse front tilting for large-area thz-pulse generation. *Opt. Express*, 10(21):1161–1166, Oct 2002.
- [Ham07] Thomas John Hammond. *Creating Ultrahigh Intensities Using a Passive Enhancement Cavity*. The University Of British Columbia, 2007.
- [Ham17] Chihiro Hamaguchi. *Basic Semiconductor Physics*. Springer, 2017.
- [HBG<sup>+</sup>02] M. Hornstein, V. Bajaj, R. Griffin, K. Kreischer, I. Mastovsky, M. Shapiro, and R. Temkin. Design of a 460 ghz second harmonic gyrotron oscillator for use in dynamic nuclear polarization. *Twenty Seventh International Conference on Infrared and Millimeter Waves*, pages 193–194, 2002.
- [HF11] Matthias C Hoffmann and József András Fülöp. Intense ultrashort terahertz pulses: generation and applications. *Journal of Physics D: Applied Physics*, 44(8):083001, feb 2011.

- [HS96] Frank A. Hegmann and Mark S. Sherwin. Generation of picosecond far-infrared pulses using laser-activated semiconductor reflection switches. *Proceedings of SPIE*, 2842, 1996.
- [HW83] Chenming Hu and Richard M. White. *Sollar Cells*. McGraw-Hill Book Company, 1983.
- [IMK<sup>+</sup>13] T. Isogai, J. Miller, P. Kwee, L. Barsotti, and M. Evans. Loss in long-storage-time optical cavities. *Optics Express*, 21(24), 2013.
- [IPI<sup>+</sup>17] Hakan Inan, Muhammet Poyraz, Fatih Inci, Mark A. Lifson, Murat Baday, Brian T. Cunningham, and Utkan Demirci. Photonic crystals: emerging biosensors and their promise for point-of-care applications. *Chem. Soc. Rev.*, 46:366–388, 2017.
- [JAA<sup>+</sup>17] J. Jelonek, G. Aiello, S. Alberti, K. Avramidis, F. Braunmueller, A. Bruschi, J. Chelis, J. Franck, T. Franke, G. Gantenbein, S. Garavaglia, G. Granucci, G. Grossetti, S. Illy, Z.C. Ioannidis, J. Jin, P. Kalaria, G.P. Latsas, I.Gr. Pagonakis, T. Rzesnicki, S. Ruess, T. Scherer, M. Schmid, D. Strauss, C. Wu, I. Tigelis, M. Thumm, and M.Q. Tran. Design considerations for future demo gyrotrons: A review on related gyrotron activities within eurofusion. *Fusion Engineering and Design*, 123:241–246, 2017. Proceedings of the 29th Symposium on Fusion Technology (SOFT-29) Prague, Czech Republic, September 5-9, 2016.
- [JMA<sup>+</sup>19] S. Jolly, N. Matlis, F. Ahr, V. Leroux, T. Eichner, A. Calendron, H. Ishizuki, T. Taira, F. Kärtner, and A. Maier. Spectral phase control of interfering chirped pulses for high-energy narrowband terahertz generation. *Nature Communications*, 10(2591), 2019.
- [Kä20] Franz X. Kärtner. Terahertz accelerator based electron and x-ray sources. *Terahertz Science and Technology*, 13(1, , pp. 22-31), 2020.
- [KAC<sup>+</sup>16] Franz X. Kärtner, Frederike Ahr, A-L. Calendron, H. Çankaya, S. Carbajo, G. Chang, G. Cirmi, K. Dörner, U. Dorda, and A. Fallahi. Axisis: Exploring the frontiers in attosecond x-ray science, imaging and spectroscopy. *In: Nuclear Instruments and Methods in Physics Research*



- Section A: Accelerators, Spectrometers, Detectors and Associated Equipment*, 829(pp. 24–29), 2016.
- [KJS<sup>+</sup>19] S.V. Kutsaev, B. Jacobson, A.Yu. Smirnov, T. Campese, V.A. Dolgashev, V. Goncharik, M. Harrison, A. Murokh, E. Nanni, J. Picard, M. Ruelas, and S.C. Schaub. Nanosecond rf-power switch for gyrotron-driven millimeter-wave accelerators. *Phys. Rev. Applied*, 11:034052, Mar 2019.
- [KL66] H. Kogelnik and T. Li. Laser beams and resonators. *Applied Optics*, 5(10):1550–1567, 1966.
- [KM18] Franz X. Kärtner and Oliver D. Mücke. *Nonlinear Optics*. Department of Physics, University of Hamburg, 2018.
- [Lee09] Yun-Shik Lee. *Principles of Terahertz Science and Technology*. Springer Science+Business Media, LLC. Springer, 2009.
- [LJ16] Sha Li and R.R. Jones. High-energy electron emission from metallic nano-tips driven by intense single-cycle terahertz pulses. *Nature Communications*, 7(13405), 2016.
- [Mai07] Stefan Alexander Maier. *Plasmonics Fundamentals and Applications*. Springer, 2007.
- [MCH96] K. I. Martin, W. A. Clarkson, and D. C. Hanna. 3 w of single-frequency output at 532 nm by intracavity frequency doubling of a diode-bar-pumped nd:yag ring laser. *Optics Letters*, 21(12), 1996.
- [MS08] Umesh K. Mishra and Jasprit Singh. *Semiconductor Device Physics and Design*. Springer, 2008.
- [MSB<sup>+</sup>14] Bernhard Mayer, Christian Schmidt, Johannes Bühler, Denis V Seletskiy, Daniele Brida, Alexej Pashkin, and Alfred Leitenstorfer. Sub-cycle slicing of phase-locked and intense mid-infrared transients. *New Journal of Physics*, 16(063033), 2014.
- [Nag10] Warren Nagourney. *Quantum Electronics for Atomic Physics*. Oxford University Press, 2010.

- [ND11] Mira Naftaly and Richard Dudley. Terahertz reflectivities of metal-coated mirrors. *Applied Optics*, 50(19), 2011.
- [Nea11] Donald A. Neamen. *Semiconductor Physics and Devices*. McGraw-Hill Companies, 2011.
- [NHH<sup>+</sup>15] Emilio A. Nanni, Wenqian R. Huang, Kyung-Han Hong, Koustuban Ravi, Arya Fallahi, Gustavo Moriena, R.J. Dwayne Miller, and Franz X. Kärtner. Terahertz-driven linear electron acceleration. *Nature Commnications*, 6(8486), 2015.
- [NM05] M. Naftaly and R.E. Miles. Terahertz time-domain spectroscopy: A new tool for the study of glasses in the far infrared. *Journal of Non-Crystalline Solids*, 351(3341-3346), 2005.
- [NM07] Mira Naftaly and Robert E. Miles. *Terahertz beam interactions with amorphous materials*. Number 107-122 in Terahertz Frequency Detection and Identification of Materials and Objects. Springer, 2007.
- [Olg21] H. T. Olgun. *Efficient high energy laser-driven multicycle terahertz generation for accelerators*. PhD thesis, Universität Hamburg, 2021.
- [OPS<sup>+</sup>20] Mohamed A. K. Othman, Julian Picard, Samuel Schaub, Valery A. Dolgashev, Samantha M. Lewis, Jeffery Neilson, Andrew Haase, Sudheer Jawla, Bruno Spataro, Richard J. Temkin, Sami Tantawi, and Emilio A. Nanni. Experimental demonstration of externally driven millimeter-wave particle accelerator structure. *Applied Physics Letters*, 117(7):073502, 2020.
- [Pie96] Robert F. Pierret. *Semiconductor Device Fundamentals*. Addison-Wesley Publishing Company, 1996.
- [Pie03] Robert F. Pierret. *Advanced Semiconductor Fundamentals*. Prentice Hall, 2003.
- [PLL<sup>+</sup>19] Xiaofeng Peng, Xingyuan Lu, Xianlong Liu, Chenliang Zhao, Rong Lin, Lin Liu, and Yangjian Cai. Generation and propagation of a hermite-gaussian correlated schell-model lg0l beam. *Applied Sciences*, 9(610), 2019.

- [PS14] Manjiri Pande and P. Singh. Study of rf breakdown and multipacting in accelerator components. In *2014 International Symposium on Discharges and Electrical Insulation in Vacuum (ISDEIV)*, pages 105–108, 2014.
- [PSR<sup>+</sup>19] Julian F. Picard, Samuel C. Schaub, Guy Rosenzweig, Jacob C. Stephens, Michael A. Shapiro, and Richard J. Temkin. Laser-driven semiconductor switch for generating nanosecond pulses from a megawatt gyrotron. *Applied Physics Letters*, 114(16):164102, 2019.
- [PSTS17] Pietro Patimisco, Angelo Sampaolo, Frank K. Tittel, and Vincenzo Spagnolo. Mode matching of a laser-beam to a compact high finesse bow-tie optical cavity for quartz enhanced photoacoustic gas sensing. *Sensors and Actuators A: Physical*, 267(70-75), 2017.
- [QXZ<sup>+</sup>14] Wen Qiao, Zhang Xiaojun, Liang Zongsen, Wang Yonggang, Sun Liqun, and Niu Hanben. Simple method of optical ring cavity design and its applications. *Optics Express*, 22(12), 2014.
- [RBBA17] Stephen Reynolds, Monica Brinza, Mohammed L. Benkhedir, and Guy J. Adriaenssens. *Photoconductivity in Materials Research*, pages 153–154. Springer International Publishing, Cham, 2017.
- [RCGM10] David S. Rabeling, Jong H. Chow, Malcolm B. Gray, and David E. McClelland. Experimental demonstration of impedance match locking and control for coupled resonators. *Optics Express*, 18(9), 2010.
- [RUS<sup>+</sup>12] Arpit Rawankar, Junji Urakawa, Hirotaka Shimizu, Yan You, Nobuhiro Terunuma, Alexander Aryshev, and Yosuke Honda. Design studies on compact four mirror laser resonator with mode-locked pulsed laser for 5 $\mu$ m laser wire. *Elsevier, Nuclear Instruments and Methods in Physics Research A*, 700(145-152), 2012.
- [SKS12] U. Singh, Nitin Kumar, and A. Sinha. Gyrotron and its electron beam source: A review. *Journal of Fusion Energy*, 31:489–505, 2012.
- [SKT<sup>+</sup>07] Keishi Sakamoto, Atsushi Kasugai, Koji Takahashi, Ryutaro Minami, Noriyuki Kobayashi, and Ken Kajiwara. Achievement of robust high-efficiency 1 mw oscillation in the hard-self-excitation region by a 170 ghz continuous-wave gyrotron. *Nature physics*, 3:411–414, 2007.

- [SM90] Richard Scheps and Joseph Myers. A single frequency nd:yag ring laser pumped by laser diodes. *IEEE Journal of Quantum Electronics*, 26(3), 1990.
- [ST07] Bahaa E.A. Saleh and Malvin Carl Teich. *Fundamentals of photonics*. Wiley series in pure and applied optics. Wiley Series, 2007.
- [STvdL00] K. Sokolowski-Tinten and D. von der Linde. Generation of dense electron-hole plasmas in silicon. *Physical Review B*, 61(4), 2000.
- [VDH<sup>+</sup>92] T. Vogel, G. Dodel, E. Holzhauser, H. Salzmann, and A. Theurer. High-speed switching of far-infrared radiation by photoionization in a semiconductor. *Applied Optics*, 31(3), 1992.
- [WB71] R. K. Willardson and Albert C. Beer. *Semiconductors and semimetals*, volume 7. Academic Press, Inc., 1971.
- [Wei01] Martin H. Weik. *photoconductive effect*, pages 1266–1266. Springer US, Boston, MA, 2001.
- [WH20] E. Wilson and B. J. Holzer. *Accelerators, Colliders and Their Application*, pages 1–14. Springer International Publishing, Cham, 2020.
- [WHFA94] A. S. Weling, B. B. Hu, N. M. Froberg, and D. H. Auston. Generation of tunable narrow-band thz radiation from large aperture photoconducting antennas. *Applied Physics Letters*, 64(2):137–139, 1994.
- [WJ19] Colin Webb and Julian Jones. *Handbook of Laser Technology and Applications*. Number Volume 1: Principles. Routledge, 2019.
- [Woo72] Frederick Wooten. *Optical Properties of Solids*. Academic Press, Inc, 1972.
- [WTHK20] Lu Wang, György Tóth, János Hebling, and Franz Kärtner. Tilted-pulse-front schemes for terahertz generation, 2020.
- [YC10] Peter Y. Yu and Manuel Cardona. *Fundamentals of Semiconductors*. Springer, 2010.
- [YF09] Hugh D. Young and Roger A. Freedman. *Física Universitaria, con Física Moderna Volumen 2*. Addison-Wesley, 2009.

- [YIO<sup>+</sup>96] S. T. Yang, Y. Imai, M. Oka, N. Eguchi, and S. Kubota. Frequency-stabilized, 10-w continuous-wave, laser-diode end-pumped, injection-locked nd:yag laser. *Optics Letters*, 21(20), 1996.
- [You14] Yan You. *Pulsed Laser Injected Enhancement Cavity for Laser-electron Interaction*. 2014PA112099, tel-01011960. Université Paris Sud - Paris XI; Qing hua da xue (Beijing, Chine), 2014.
- [YS05] Teresa Yonte Sanchidrián. *Fundamentos geométricos de la óptica de multicapas*. PhD thesis, Universidad Complutense de Madrid, 2005.
- [YY07] Amnon Yariv and Pochi Yeh. *Photonics: Optical Electronics in Modern Communications*. The Oxford series in electrical and computer engineering. Oxford University Press, 2007.
- [ZBC<sup>+</sup>01] Fred J. Zutavern, Albert G. Baca, Weng W. Chow, Michael J. Hafich, Harold P. Hjalmarson, Guillermo M. Loubriel, Alan Mar, Martin W. O'Malley, L. D. Roose, and G. Allen Vawter. Electron-hole plasmas in semiconductors. *Pulsed Power Plasma Science*, 1(289–293), 2001.